

# **Numerical Simulations of Fracture Problems using Smoothed Floating Node Method**

A Thesis to be Submitted  
In Partial Fulfillment of the Requirements  
for the Degree of

**Doctor of Philosophy**

by

**Umed Singh  
(2018MEZ0003)**



**DEPARTMENT OF MECHANICAL ENGINEERING  
INDIAN INSTITUTE OF TECHNOLOGY ROPAR**

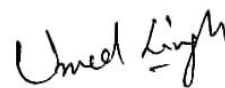
February, 2024

Copyright © “2023” by Indian Institute of Technology Ropar

DEDICATED  
TO  
FAMILY & FRIENDS

## DECLARATION

I declare that this work entitled “Numerical Simulations of Fracture Problems using Smoothed Floating Node Method” has not previously been accepted in substance for any degree and is not being simultaneously submitted in candidature for any other degree. This thesis is being submitted in partial fulfilment of the requirements for the degree of PhD in Mechanical Engineering. This thesis is the result of my own independent investigation, except where otherwise stated. I have acknowledged all the other sources by stating the references explicitly. I declare that any idea/data/fact/source stated in my thesis has not been fabricated/falsified/misrepresented. All the principles of academic honesty and integrity have been followed. I understand that any violation of the above will be cause for disciplinary action by the Institute and can also evoke penal action from the sources which have thus not been properly cited or from whom proper permission has not been taken when needed. I hereby give consent for my thesis, if accepted, to be available online in the Institute’s Open Access repository and for inter-library loan, and for the title and abstract to be made available to outside organizations.



---

Umed Singh  
2018MEZ0003

Date: 05-02-2024

## ACKNOWLEDGEMENTS

First and foremost, I would like to express my deepest gratitude to my thesis advisor, Dr. Sachin Kumar, Associate Professor, Department of Mechanical Engineering, IIT Ropar, for his invaluable mentorship, unwavering support, and insightful guidance throughout the research process. His expertise and feedback significantly shaped the direction and quality of this thesis.

I would like to thank my doctoral committee members, Dr. Ekta Singla (Committee Chairperson, Associate Professor, Department of Mechanical Engineering, IIT Ropar), Dr. Navin Kumar (Professor, Department of Mechanical Engineering, IIT Ropar), Dr. Srikant Sekhar Padhee (Assistant Professor, Department of Mechanical Engineering, IIT Ropar) and Dr. Naveen James (Assistant Professor, Department of Civil Engineering, IIT Ropar), for their valuable feedback, constructive criticism, and expertise in reviewing and refining this work. Their insights greatly improved the rigor of this research.

I am grateful to the Indian Institute of Technology Ropar for providing the necessary resources, facilities, and an intellectually stimulating environment that fostered my academic growth and research endeavours.

I am thankful to my colleagues Mr. Alok Negi, Mr. Aakash Soni, Mr. Anshul Pandey, Mr. Rajiv Kumar Pal, Mr. Tripurari and fellow students Mr. Ram Naresh Yadav, Mr. Piyush Uniyal, Mr. Piyush Lakhani, Mr. Krashan Kumar Dwivedi, Mr. Neeraj Deswal, Mr. Somenath Gorai, Mr. Sanjay Singh, Mr. Rakesh Kumar, Mr. Mukesh Kumar, Mr. Rajesh Bhura who provided valuable discussions, encouragement, and emotional support throughout this academic pursuit. Their friendship made this journey more enjoyable and memorable. I express my deepest appreciation to my family for their encouragement, and support throughout this academic journey. Their support has been my constant source of motivation, and I am forever grateful.

Finally, I express my deepest appreciation to the Ministry of Education, Government of India, for the financial assistance, which made this research possible.

Thank you to all who have been an integral part in shaping this thesis and my academic experience. Your contributions are deeply appreciated.

## **CERTIFICATE**

It is certified that the work contained in the thesis titled “Numerical Simulations of Fracture Problems using Smoothed Floating Node Method” by “Umed Singh” has been carried out under my supervision and that this work has not been submitted elsewhere for the award of any degree.



**Signature of the Supervisor**

**Dr. Sachin Kumar**

**Department of Mechanical Engineering**

**IIT Ropar**

## LAY SUMMARY

Some clear examples of fracture problems that engineers might face: like gears, bearings, springs, and fasteners can break or crack. Also, parts in cars, like axles, connecting rods, and crankshafts, can experience a lot of stress during working. Other important examples are dams, power plants, pressure vessels, and offshore structures. Every material has imperfections or irregularities, like micro-defects or cracks. These imperfections can make stress in a material to accommodate at one spot. Defects during manufacturing, like bad welding or casting, can also make things more likely to break. Factors in the environment, such as rust, high heat, or radiation, can also make things break easier. Figuring out fracture problems can be really tough. It depends on the shape of the thing, how it's being used, and what it's made of. Sometimes, a part can break slowly over time, or it can break suddenly and cause big problems. When things break, it can have adverse effects on both individuals and finances.

To this end, fracture mechanics helps engineers design things to stay strong and predict how long they will last before they start to crack. There are ways to test materials to see how strong they are under different conditions. However, once a test is done on a material, it can't be used again, so it's a bit wasteful. There are also computer techniques that can help us see where cracks might start and how they might grow. One technique called the "smoothed floating node method" is used in this thesis to study how engineering materials behave when they start to break.

## **ABSTRACT**

Numerical Simulations of Fracture Problems using Smoothed Floating Node Method

Umed Singh

Ensuring the safety and dependability of a wide array of engineering applications is of utmost importance, particularly in fields like aerospace, civil infrastructure, and mechanical components. It is imperative to accurately comprehend and forecast the onset and spread of cracks within engineering structures to prevent potentially disastrous failures with severe consequences. As materials are utilized in practical scenarios, their strength may diminish based on variables such as loading conditions, material composition, and environmental factors. The presence of flaws such as cracks, voids, holes, inclusions, discontinuities and manufacturing defects introduces complexity, thus requiring the utilization of fracture mechanics to tackle these complexities. Also changes in temperature within a material can lead to the development of thermal stresses, which may result in cracks and failure of the structure. Beyond cracking, temperature variations also result in alterations in the material's microstructure, and these changes significantly affect its mechanical properties and behaviour. Researchers have developed computational techniques, including both analytical and numerical methods, to tackle these challenges. In the field of computational analysis, two main approaches are highlighted in existing literature: Smeared Crack Approach and Discrete Crack Approach. Smeared or continuous methods, demonstrated by continuum damage mechanics, forecast material degradation by tracking the accumulation of damage in the material. On the other hand, discrete crack approaches consider cracks as interfaces, proving especially valuable for dealing with complex crack patterns.

Linear elastic fracture mechanics simplifies the fracture behaviour analysis for materials that behave linearly elastic, but in practical applications, challenges frequently arise due to the presence of nonlinearities in the problems, such as in quasi-brittle materials (concrete, rock, bone, ice, and various composites) with nonlinear fracture process zone ahead of the crack tip. Many advanced numerical methods are reported in the literature to solve fracture mechanics problems involving arbitrary crack propagation without the use of remeshing to tackle the strong discontinuity. This thesis aims to develop a formulation based on discrete crack approach using floating node



method in combination with strain smoothening technique to solve the fracture mechanics problems having strong discontinuity. The crack inside the specimen finds its true position with the help of floating nodes rather than tackling the crack by virtual nodes positioned on the standard nodes by using the special enrichment functions.

The initial focus of this thesis is to develop a Smoothed Floating Node Method (SFNM) that accurately traces the crack real position by utilizing floating nodes based on the crack propagation direction criterion. A strain smoothing technique is employed, replacing area integral with a line integral to handle the integration scheme. Here, to mitigate challenges related to element distortion and convexity, a cell-based smoothing approach is adopted which eliminates the need of Jacobian matrix in the numerical calculations. The method's precision and convergence are thoroughly analysed, and error norms are calculated based on both energy and stress Intensity factors. Another contribution of this thesis is the incorporation of the nonlinear behaviour of the fracture process zone into the smoothed floating node method. The zero thickness cohesive element used in this work, acts as a medium to transfer the cohesive forces through the partially damaged materials in cohesive zone. The potential based intrinsic cohesive zone modelling formulation is aligned to the proposed SFNM method for the analysis of fracture behaviour of the quasi brittle materials. First, the numerical framework is validated through the patch test of a two-dimensional specimen subjected to both mode I and mode II loading conditions. Following this verification, the framework is further applied to address two-dimensional standard fracture problems considering the cohesive strengths of the material, both in the normal and tangential directions. The assessment of the SFNM coupled with CZM is conducted for scenarios involving straight and curved crack growth.

Next, the formulation of the Smoothed Floating Node Method is extended to address fracture problems occurring within a thermally loaded environment, while considering the influence of mechanical boundary constraints. The analysis involves examining cracked specimens subjected to both isothermal and adiabatic crack thermal loading conditions. The fracture failure of the specimen is attributed to the thermal stresses induced in this setting. The cohesive zone model is employed to account for the combined thermo-mechanical effects. The nonlinear fracture process zone is examined both under thermal loading and mechanical loading separately, as well as in their combined state. Various homogeneous and bi-material problems are effectively solved using the proposed methodology, and the obtained results are compared with the

existing literature results. Finally, comprehensive findings are presented for cases involving a combination of thermal and mechanical loads, specifically focusing on quasi-brittle materials.

**Keywords:**

Fracture mechanics, smoothed floating node method, strain smoothing, cohesive zone modelling, fracture process zone, line integration, element cell, quasi-brittle materials, stress intensity factor.

## LIST OF PUBLICATIONS

### *Journal papers*

- Negi A, Singh U, Kumar S. Structural size effect in concrete using a micromorphic stress-based localizing gradient damage model. Eng Fract Mech 2021;243.
- Singh U, Kumar S, Chen B. Smoothed floating node method for modelling 2D arbitrary crack propagation problems. Theor Appl Fract Mech 2022;117.
- Singh U, Kumar S. Smoothed floating node method for modelling cohesive fracture in quasi-brittle materials. Mech Adv Mater Struct 2022.
- Singh U, Kumar S, Pathak H, Bui TQ, Gupta RK. Modelling of 2D thermo-elastic brittle fracture using smoothed floating node method. Mech Adv Mater Struct 2024.
- Thermo-mechanical modelling of 2D crack growth mechanics problems for quasi-brittle materials using SFNM, (To be submitted).

### *Conference papers*

- Singh, U. and Kumar, S. (2019). Failure analysis of quasi-brittle materials using cohesive zone model assisted XFEM. 64th Congress of the Indian Society of Theoretical and Applied Mechanics (ISTAM), December 9-12, 2019, IIT Bhubaneswar, India.
- Singh, U. and Kumar, S. (2022). Failure analysis of quasi-brittle materials using CZM based floating node method. 67th Congress of the Indian Society of Theoretical and Applied Mechanics (ISTAM), December 14-16, 2022, IIT, Mandi, India.

# TABLE OF CONTENTS

<b>DECLARATION.....</b>	<b>IV</b>
<b>ACKNOWLEDGEMENTS.....</b>	<b>V</b>
<b>CERTIFICATE .....</b>	<b>VI</b>
<b>LAY SUMMARY .....</b>	<b>VII</b>
<b>ABSTRACT .....</b>	<b>VIII</b>
<b>LIST OF PUBLICATIONS.....</b>	<b>XI</b>
<b>TABLE OF CONTENTS.....</b>	<b>XII</b>
<b>Chapter 1 Introduction.....</b>	<b>1</b>
1.1 Background and Motivation.....	3
1.2 Fracture Behaviour of Materials .....	4
1.2.1 Modes of fracture .....	5
1.2.2 Types of fracture .....	6
1.3 Research Approach and Methodology .....	7
1.3.1 Cohesive Zone Modelling .....	8
1.4 Objectives.....	9
1.5 Thesis Outline .....	9
<b>Chapter 2 Literature Review .....</b>	<b>13</b>
2.1 Continuous Approach.....	13
2.1.1 Gradient Damage Models.....	14
2.1.2 Peridynamics .....	15
2.1.3 Phase Field Method.....	16
2.2 Discontinuous Approaches.....	17
2.2.1 Phantom Node Method.....	19
2.2.2 Extended Finite Element Method.....	20
2.2.3 Element-Free Galerkin Method with geometric discontinuity.....	21

2.2.4 Crack Particle Method .....	22
2.2.5 Floating Node Method.....	22
2.2.6 Strain Smoothing Approach .....	23
2.2.7 Boundary Element Method .....	24
<b>Chapter 3 Development of SFNM to Model 2D Arbitrary Crack .....</b>	<b>25</b>
3.1 Introduction .....	25
3.2 Numerical Formulation .....	28
3.2.1 Governing equations for elasto-statics .....	28
3.2.2 Basic formulation of FNM .....	30
3.2.3 Strain smoothing technique .....	33
3.2.4 Shape function construction and numerical integration scheme .....	36
3.2.5 SFNM outline .....	40
3.3 SIF Computation .....	40
3.4 Crack Propagation Criterion.....	42
3.5 Numerical Examples .....	42
3.5.1 Static crack examples .....	43
3.5.2 Crack propagation examples .....	47
3.6 Conclusions .....	53
<b>Chapter 4 SFNM Implementation with CZM for Quasi-brittle Materials.....</b>	<b>55</b>
4.1 Introduction .....	55
4.2 Numerical Formulation .....	57
4.2.1 Governing equations for elasto-statics .....	57
4.2.2 Basic formulation of FNM .....	59
4.2.3 Strain smoothing technique .....	60
4.3 Cohesive Zone Interface Model .....	62
4.3.1 Kinematics of the interfacial surface .....	64
4.3.2 Implementation of a cohesive element in SFNM.....	66
4.4 Crack Growth and Direction Criterion .....	67
4.5 Numerical Examples .....	68
4.5.1 Patch test validation of SFNM .....	69
4.5.2 Three-point bending test.....	73
4.5.3 Mixed mode fracture in eccentrically notched beam .....	75
4.5.4 Mixed mode failure of an L-shaped panel.....	77

4.6 Conclusions .....	79
<b>Chapter 5 Thermo-elastic Brittle Fracture using SFNM with CZM .....</b>	<b>81</b>
5.1 Introduction .....	81
5.2 Smoothed Floating Node Method .....	82
5.3 Governing Equations.....	87
5.3.1 Weak formulation for thermo-elastic loading .....	88
5.4 Thermal Cohesive Zone .....	90
5.5 SIF Computation and Crack Propagation Criterion .....	92
5.6 Numerical Results .....	94
5.6.1 Isothermal centre crack .....	94
5.6.2 Adiabatic centre crack.....	97
5.6.3 Adiabatic edge crack propagation .....	99
5.6.4 Bi-material adiabatic interfacial crack propagation .....	101
5.7 Conclusions .....	104
<b>Chapter 6 Thermo-mechanical Quasi-brittle Fracture .....</b>	<b>105</b>
6.1 Introduction .....	105
6.2 Numerical Formulation .....	107
6.2.1 Weak formulation of equilibrium equations .....	108
6.3 Cohesive Crack Modelling.....	110
6.4 Adiabatic edge crack propagation .....	111
6.5 Numerical Simulations.....	111
6.5.1 Cruciform Specimen .....	111
6.6 Conclusions .....	117
<b>Chapter 7 Conclusions and Future Scope.....</b>	<b>119</b>
7.1 Conclusions .....	119
7.2 Future Scope.....	121
7.3 Method Limitation.....	122

## LIST OF FIGURES

Figure 1.1: Comparison between the displacement and strain profiles for (a) continuous and (b) discontinuous approaches.....	2
Figure 1.2: Modes of fracture .....	5
Figure 1.3: Different fracture types: (a) brittle, (b) ductile and (c) quasi-brittle [1].....	6
Figure 3.1: A cracked domain with boundary conditions.....	29
Figure 3.2: A schematic representation of strong discontinuity modelling in an element using floating node method.....	31
Figure 3.3: Crack tip modelling in floating node .....	32
Figure 3.4: Schematic of subcells formation for integration in SFNM: <b>(a)</b> crack growth in domain <b>(b)</b> intact element subcells <b>(c)</b> 2 sub-elements with inclined crack path and further subdivision into triangular subcells and <b>(d)</b> 2 quadrilateral sub-elements with inclined crack path and further subdivision into quadrilateral subcells.....	34
Figure 3.5: Quadratic element division into smoothing subcells and integration scheme: <b>(a)</b> 1-subcell <b>(b)</b> 2-subcells <b>(c)</b> 3-subcells and <b>(d)</b> 4-subcells. ....	35
Figure 3.6: Triangular element division into smoothing subcells and integration scheme, (a) 1-subcell (b) 4-subcells.....	37
Figure 3.7: Detailed procedure in SFNM for modelling crack initiation to final failure.....	39
Figure 3.8 A rectangular plate with an edge crack under mode-I loading.....	44
Figure 3.9 The convergence in strain energy for the rectangular plate with edge crack under mode-I loading. ....	44
Figure 3.10 Comparison of convergence rate between FNM and SFNM in the SIF .....	45
Figure 3.11 Static edge crack plate stress contours under mode-I loading: <b>(a)</b> $\sigma_{xx}$ <b>(b)</b> $\sigma_{xy}$ <b>(c)</b> $\sigma_{yy}$ . ....	45
Figure 3.12 : A rectangular plate with an edge crack under shear (mode-II) loading, dimensions are in mm. ....	46
Figure 3.13: The convergence in strain energy for the rectangular plate with edge crack under mode-II loading.....	46
Figure 3.14: Comparison of convergence rate of SIF vs mesh size ( $h$ ) between FNM and SFNM; <b>(a)</b> convergence in SIF $K_I$ <b>(b)</b> convergence in SIF $K_{II}$ .....	47
Figure 3.15: SIF variation with crack length under mode-I loading for edge crack plate. ....	48
Figure 3.16: Normal stress contour of edge crack plate under normal load; (a) $a/W=0.2$ , (b) $a/W=0.3$ and (c) $a/W=0.45$ .....	48
Figure 3.17: SIF variation with crack length under mode-II loading for edge crack plate.....	49
Figure 3.18: Stress contour plots of edge crack plate under shear load at $aW = 0.5$ : <b>(a)</b> $\sigma_{xx}$ <b>(b)</b> $\sigma_{xy}$ <b>(c)</b> $\sigma_{yy}$ .....	49
Figure 3.19: Crack growth trajectory comparison of an edge crack plate under mode-II loading.....	50
Figure 3.20: (a) Bi-material plate with an interfacial edge crack under mode-I loading; (b) Crack growth trajectory comparison of a bi-material interface edge crack. ....	51

Figure 3.21: SIF vs crack length plot for bi-materials edge crack plate under mode-I. ....	51
Figure 3.22: Deformed configuration with element subdomains for bi-material edge crack plate under mode-I loading.....	52
Figure 3.23: Stress and Strain contour plot at failure condition; <b>(a)</b> strain contour plot in y-direction <b>(b)</b> stress contour plot in y-direction. ....	52
Figure 4.1: A cracked domain with boundary conditions .....	58
Figure 4.2: (a) Schematic representation of strong discontinuity modelling in an element using FNM, (b) Schematic representation of crack tip modelling in FNM.....	59
Figure 4.3: Quadratic element division into smoothing cells and integration scheme: <b>(a)</b> Q4, 1-cell <b>(b)</b> Q4, 2-cells <b>(c)</b> Q4, 3-cells <b>(d)</b> Q4, 4-cells and <b>(e)</b> T3, 1-cell.....	61
Figure 4.4: Schematic representation of fracture process zone; <b>(a)</b> crack with traction free, FPZ and intact elastic domain, <b>(b)</b> stress transfer inside the nonlinear FPZ. .	63
Figure 4.5: Representation of the cohesive element inside FPZ as per the crack propagation direction. Dotted line defines the linear cohesive element to calculate displacement separation. Two hexagonal points on the linear cohesive element denotes integration points. ....	66
Figure 4.6: Illustration of crack growth criterion. A 90° sector considered for the computation of nonlocal stresses at crack tip using weighted average method .....	67
Figure 4.7: Geometry and boundary conditions of mode I specimen with cohesive element inserted horizontally at the centre.....	69
Figure 4.8: Comparison of stress vs displacement curve of proposed method and literature [49] results under mode I test .....	70
Figure 4.9: Displacement (separation) and normal stress distribution in sub-elements during mode I specimen test .....	71
Figure 4.10: Geometry and boundary conditions of mode II specimen with cohesive element along the diagonal .....	72
Figure 4.11: Comparison of stress vs displacement curve of proposed method and literature [49] results under mode II test .....	72
Figure 4.12: Geometry and boundary conditions of three-point beam specimen with an edge crack under mode I loading. ....	73
Figure 4.13: Comparison of Force vs displacement curve of proposed method and literature [55] results of three-point bending test under mode I loading.....	74
Figure 4.14: Stress contour of three-point bending test specimen. ....	74
Figure 4.15: Geometry and boundary conditions of three-point beam specimen with eccentric crack under mixed mode loading .....	75
Figure 4.16: Comparison of Force vs CMOD curve of three-point bending test of proposed method with literature [56] results for eccentric crack under mixed mode loading .....	75
Figure 4.17: Stress contour of eccentrically loaded three-point bending specimen.....	76
Figure 4.18: L-shape panel geometry with boundary conditions (all dimensions are in mm). ....	77
Figure 4.19: Comparison of force vs displacement curve of proposed method and literature [23] results of L-shaped panel under mixed mode loading. ....	78



Figure 4.20: (a) L-shaped panel deformed shape (magnification factor 25), (b) Comparison of the crack path with experimental [23].	78
Figure 4.21: Stress Contour plot of L-shaped panel	79
Figure 5.1: Schematic representation of strong discontinuity of an element dividing into sub-elements.	83
Figure 5.2: Representation of different types of elements in domain under strong discontinuity.	84
Figure 5.3: Quadrilateral and Triangular elements division into smoothing cells and integration scheme: (a) Q4, 4-cells and (b) T3, 1-cell.	84
Figure 5.4: Flow chart of SFNM to model crack propagation under thermo-elastic loading conditions.	86
Figure 5.5: Two dimensional cracked domain with loading and boundary conditions.	88
Figure 5.6: Cohesive zone crack interfaces separation with floating nodes along tangential and normal directions.	91
Figure 5.7: Normal separation law for heat transfer across a thermal cohesive crack.	92
Figure 5.8: Geometry of homogeneous square plate with a centre crack under isothermal load.	95
Figure 5.9: Temperature contour for a symmetrical half plate subjected to isothermal loads considering half of centre crack as an edge crack for $a/W = 0.4$ .	95
Figure 5.10: Stress contour plots for a symmetrical half plate subjected to isothermal loads considering half of centre crack as an edge crack. (a) $\sigma_{yy}$ ; (b) $\sigma_{xx}$ ; (c) $\sigma_{xy}$ .	96
Figure 5.11: SIF Convergence analysis of the Isothermal centre crack in a square plate with varying of number of nodes.	96
Figure 5.12: Normalized SIF comparison of the Isothermal centre crack in a square plate with Literature1 [166] and Literature2 [50].	97
Figure 5.13: Geometry of homogeneous square plate with a centre crack under adiabatic thermal load.	97
Figure 5.14: Temperature contour plot for a symmetrical half plate subjected to adiabatic thermal load considering half of centre crack as an edge crack for $a/W = 0.4$ .	98
Figure 5.15: Stress contour plots for a symmetrical half plate subjected to adiabatic thermal loads considering half of centre crack as an edge crack. (a) $\sigma_{yy}$ ; (b) $\sigma_{xx}$ ; (c) $\sigma_{xy}$ .	98
Figure 5.16: Normalized SIF comparison of the Adiabatic centre crack in a square plate with Literature1 [22] and Literature2 [50].	99
Figure 5.17: Square homogeneous plate with an edge crack under adiabatic thermal load.	99
Figure 5.18: Temperature contour plot for homogeneous square plate with an edge crack under adiabatic thermal load.	100
Figure 5.19: Stress contour plots for homogeneous square plate with an edge crack under adiabatic thermal load : (a) $\sigma_{yy}$ ; (b) $\sigma_{xx}$ ; (c) $\tau_{xy}$ .	100
Figure 5.20: SIF vs crack length variation for edge crack of homogeneous square plate under adiabatic thermal load.	101

Figure 5.21: Bi-material plate with an edge crack under adiabatic thermal load.....	102
Figure 5.22: Temperature contour plot for bi-material plate with an edge crack under adiabatic thermal load.....	102
Figure 5.23: Stress contour plot for bi-material plate with an edge crack under adiabatic thermal load: (a) $\sigma_{yy}$ ; (b) $\sigma_{xx}$ ; (c) $\tau_{xy}$ . ....	103
Figure 5.24: SIF variation with respect to crack length of an adiabatic edge crack of a bi-material plate. ....	103
Figure 6.1: (a)Two dimensional cracked domain with loading and boundary conditions, (b) domain division as per discontinuity interface. ....	107
Figure 6.2: Cruciform Plate geometry with boundary conditions.....	112
Figure 6.3: Cruciform plate crack path under pure mechanical loading conditions (Literature [170]). ....	113
Figure 6.4: Cruciform plate displacement contour (displacement in m) under pure mechanical loading conditions. ....	113
Figure 6.5: Cruciform plate stress (N/m <sup>2</sup> ) contour in y-direction under pure mechanical case. ....	114
Figure 6.6: Structural Response of the cruciform plate.....	114
Figure 6.7: Deformed Shape under mechanical loading conditions. ....	115
Figure 6.8: Crack path comparison under pure thermal loading conditions (Literature [170]). ....	115
Figure 6.9: Temperature distribution profile under pure thermal loading conditions. ....	116
Figure 6.10: Crack path comparison under thermo-mechanical loading conditions (Literature [170]). ....	116
Figure 6.11: Stress Contour profile under thermo-mechanical loading conditions.....	117

## LIST OF TABLES

Table 3.1: Shape function value at different sites within SC4Q4 element ( <b>Figure 6(d)</b> ) .....	37
Table 3.2: Shape function values at different sites within SC1T3 element (Figure 3.7(b)) .....	38
Table 3.3: Properties of the constituents of bi-materials rectangular plate. ....	50
Table 4.1: Shape functions values at different sites (refer <b>Figure 4.3</b> ) within T3 element .....	62
Table 4.2: Shape functions values at different sites (refer <b>Figure 4.3</b> ) within Q4 element.....	62
Table 4.3: Material properties and fracture parameters for mode I test .....	70
Table 4.4: Material properties and parameters for the three-point bending test.....	73
Table 4.5: Material properties and parameters for three-point bending eccentrically notched beam test.....	76
Table 4.6: Material properties and parameters for L-shaped panel.....	77
Table 6.1: Material properties and parameters for cruciform plate.....	112
Table 6.2: Different cases of thermo-mechanical loading conditions. ....	112

## NOTATIONS AND ABBREVIATIONS

### Nomenclature

$a$	initial crack length
$q$	heat flux
$Q$	heat source
$k$	thermal conductivity
$\mathbf{b}$	body force vector per unit volume
$\mathbf{B}$	shape functions gradients matrix
$\tilde{\mathbf{B}}_I$	smoothed gradient matrix of node I
$\mathbf{d}$	nodal displacements vector
$\mathbf{D}$	material elasticity tensor
$E$	Young's modulus
$\mathbf{f}$	externally applied force vector
$f_t$	tensile strength
$\mathbf{K}$	global stiffness matrix
$\mathbf{L}$	local displacement-separation relation matrix
$\hat{\mathbf{n}}$	unit outward normal
$\mathbf{N}$	shape function matrix
$\mathbf{R}$	rotational matrix
$t$	out plane thickness
$\bar{\mathbf{t}}$	applied traction vector
$\mathbf{t}_c$	cohesive traction vector
$\bar{\mathbf{u}}$	local nodal displacements
$\alpha$	shape parameter normal
$\alpha_T$	thermal expansion coefficient
$\beta$	shape parameter tangential
$\nu$	Poisson's ratio
$\Delta$	displacement jump across the crack surface
$\nabla$	gradient operator
$\boldsymbol{\sigma}$	Cauchy stress tensor
$\Psi$	potential function
$\langle . \rangle$	Macauley bracket
$\bar{\Delta}$	local displacement jump
$\mathbf{Y}$	transformation matrix
$\bar{\sigma}$	nonlocal weighted average stress
$\theta_c$	direction of crack growth
$\lambda_n$	normal initial slope indicator
$\lambda_t$	tangential initial slope indicator
$\phi$	smoothing function
$\phi_n$	fracture energy normal

$\phi_t$	fracture energy tangential
$\tau_{max}$	shear strength
Q4	4-noded quadrilateral element
T3	3-noded triangular element

### **Acronyms**

LEFM	linear elastic fracture mechanics
CZM	cohesive zone model
CMOD	crack mouth opening displacement
FPZ	fracture process zone
FEM	finite element method
FNM	floating node method
SFEM	smoothed finite element method
SFNM	smoothed floating node method
SIF	stress intensity factor
TSL	traction separation law
XFEM	extended finite element method
dof	degree of freedom
XIGA	extended isogeometric analysis

Page left blank intentionally

# Chapter 1

## Introduction

---

In order to comprehensively assess the safety and reliability of components and structures, it is of utmost importance to have a fundamental understanding of material failure behaviour. This understanding aids in to identify and address potential weak points in the design or manufacturing process. Additionally, Engineers can simulate various conditions and assess how materials respond without the need for physical prototypes, enabling more efficient design iterations and optimization. As structures and components undergo practical usage, its material strength may decrease depending on factors such as the type of loading, the materials involved, and the prevailing environmental conditions. The presence of cracks, voids, holes, inclusions, discontinuities, and manufacturing defects in the material introduces complexities that render the application of conventional solid mechanics' failure theories ineffective in analysing material and structural failure mechanisms. Some of the instances of such complexities include the building cracks, pressure vessel ruptures, aircraft rotor failures, bridge collapses, turbine blade malfunctions, and machine component breakages etc. Therefore, advanced evaluation criteria are required to account for these intricate parameters in the assessment process.

Addressing these multifaceted challenges involves the use of both experimental and computational methods. Numerous experimental methodologies require both destructive and non-destructive procedures to scrutinize the failure characteristics of materials and structures. In case of destructive testing, the reusability of an individual specimen post-testing remains prohibited even if it successfully passes the test. Examples include tensile testing, 3-point bend tests etc. In contrast, non-destructive testing (NDT) is a valuable approach employed to assess the properties of a material, without causing any damage to the specimen. Various NDT methods, such as visual inspection, radiography, and ultrasonic testing etc. are utilized for this purpose. NDT ensures that the tested part remains fit for service even after undergoing the evaluation. It's worth noting that the introduction of human error and suboptimal calibration of the testing apparatus holds the potential to yield erroneous prediction. Also, Enhancing the

reliability of outcomes mandates a larger number of test samples. Therefore, to ensure robust repeatability and precise accuracy during testing, an assessment of various factors is required before executing tests.

Conversely, within the domain of computational techniques, there exists a range of analytical and advanced numerical methods that can effectively address complex crack geometries and material behaviours. Analytical solutions are available for the standard simple geometry problems and frequently fall short when facing complex challenges arising from intricate structural geometries and boundary conditions. Recently, various innovative methodologies for modelling fracture problems have surfaced. These approaches can be broadly divided into two types, distinguished by their representation of fracture namely, continuous and discontinuous approaches. The continuous approach utilizes the theoretical framework of continuum damage mechanics (CDM), while the discontinuous approach is based on fracture mechanics theory. A comparison between continuous and discontinuous technique is presented in **Figure 1.1**. CDM is suitable for micro-crack nucleation and coalescence, while discrete approaches yield more accurate results for finite cracks. The CDM approach perceives crack development as a gradual process of damage accumulation. It treats cracks as diffuse zones, and illustrates how materials degrade under stresses. This approach simplifies the complex nature of cracks and provides insights into material failure using continuum damage mechanics.

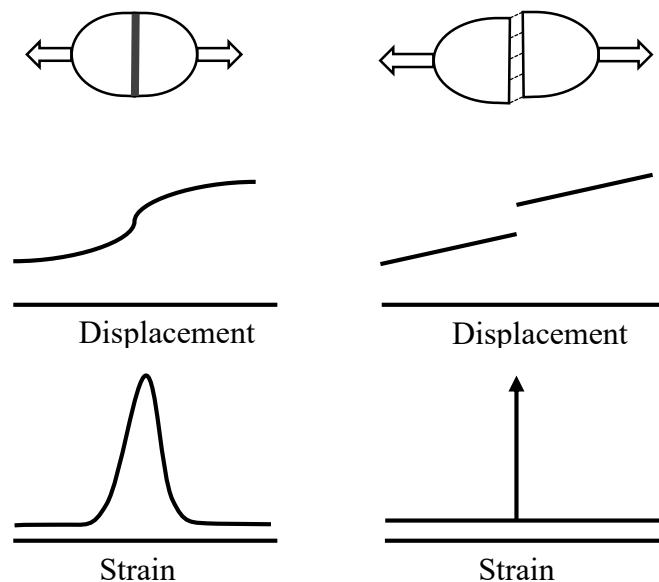


Figure 1.1: Comparison between the displacement and strain profiles for (a) continuous and (b) discontinuous approaches.



Within engineering, fracture mechanics based on the discrete approach of crack assessment, holds a fundamental position, playing a critical role in guaranteeing the reliability and safety of various applications such as aerospace, civil infrastructure, and mechanical systems. The main assumption at the core of fracture mechanics lies that every engineering material inherently contains defects or manufacturing imperfections that can be represented as cracks. Therefore, accurate understanding and prediction of crack initiation and propagation within engineering structures are crucial for preventing catastrophic failures.

## 1.1 Background and Motivation

The Finite Element Method (FEM) can be the best suited numerical tool to carry out numerical simulations of fracture mechanics problems. In FEM, a mapped element takes part as a paired set between physical and natural coordinate systems to maintain the exact equivalence. Thus, exceeding the acceptable limit for element distortion is prohibited, as it leads to singularity issues in the inversion of the stiffness matrix. Moreover, in simulations of crack propagation behaviour using FEM, conformal meshing is required to capture the crack discontinuity [1], and singular elements are also required to model the crack tip singularity. In addition to this, remeshing during crack growth introduces errors while shifting the field variables data from the previous mesh to the new one. Therefore, it becomes cumbersome to model crack propagation and evolving discontinuity using the FEM approach alone. A more robust framework is desirable for the prediction of progressive failure. Various challenges arise when attempting to solve crack problems using computational methods. These challenges involve various issues, such as the need for remeshing and enrichment functions to precisely depict static behaviour and the propagation of cracks [2,3]. In discrete approaches, the incorporation of isoparametric mapping necessitates checking the convexity condition of elements. However, the requirement of conformal mesh and remeshing during crack growth can be eliminated using advanced numerical methods such as eXtended Finite Element Methods (XFEM), Meshless Methods, Boundary Element Method, Scaled Boundary Element Finite Element Method (SBFEM). For instance, in case of XFEM, to effectively model blending, split, and tip elements, an enhanced integration scheme becomes essential. Additionally, complications arise from the aspect ratio of sub-elements divided by the crack path, which hinders the accurate computation of field variables.

Another significant concern relates to the failure characteristics of materials. In a more extensive context, failures can take in diverse forms, involving brittleness, quasi-brittleness, and ductility. For brittle materials, the fracture process zone is considerably smaller compared to the overall structure size, which is a key factor contributing to immediate fracture upon surpassing a critical load threshold. Addressing the challenge of failure, there exists the phenomenon of quasi-brittle failure, which poses significant modelling difficulties due to microstructural variations within quasi-brittle structures. This type of failure is observable across a diverse range of materials, including polycrystalline ceramics, cementitious materials like concrete, various rock types, wood, bones, and a variety of composites. These materials hold immense significance in the fields of engineering and materials science due to their extensive use, especially within engineering applications.

To overcome the limitations associated with numerical methods such as FEM, XFEM etc., and to capture the nonlinear fracture process zone, a new approach called the Smoothed Floating Node Method (SFNM) is developed by combining the Floating Node Method (FNM) [4,5] with strain smoothing technique [6]. This thesis introduces a formulation and implementation of the SFNM to both brittle and quasi-brittle materials. The integration of cohesive zone modelling into the SFNM methodology is also comprehensively demonstrated across various loading scenarios for quasi-brittle materials. This study covers both mechanical and thermal loading, along with their combined impacts, to investigate material fracture utilizing a discrete approach. Further elaboration on this can be found in the Objectives and Thesis Outline sections.

## 1.2 Fracture Behaviour of Materials

The introduction of all-welded designs, such as the Liberty ships and T-2 tankers during World War II, proved to be a major factor behind accidents and structural failures. Among the 2,500 Liberty ships constructed during the war, 145 of them suffered catastrophic breakages, and nearly 700 experienced significant issues. These failures were particularly unexpected because they frequently happened to be in low-stress situations, including when a ship was stationary in a dock. This puzzling problem prompted extensive investigations, which determined that the fractures were brittle in nature, primarily attributed to flaws and areas where stress concentrated. Therefore, it becomes imperative, from a fracture mechanics perspective, to gain a comprehensive understanding of how materials respond to crack propagation and environment

conditions. This understanding is essential in the context of designing structures and components resilient enough to withstand the inherent flaws present in real-world materials. The fracture behaviour of a material depends on the loading and the type of the material. These are discussed in the following subsections.

### 1.2.1 Modes of fracture

In the area around a crack tip, all stress systems are linked to a specific way that the crack surface moves locally. In accordance with fracture mechanics principles, the fracture process is typically classified into three distinct modes of fracture.

*Mode I Fracture (Opening Mode):* In this type of fracture, the surfaces of a crack tend to separate, creating a stretching force on the crack surfaces (**Figure 1.2(a)**). This is the most common fracture mode and used in fracture toughness testing. Linear elastic fracture mechanics, which relies on calculations involving the stress intensity factor ( $K$ ), explains the connection between applied stress, crack size, and material properties. This relationship helps in determining the critical stress level required for a crack to start spreading in a brittle material.

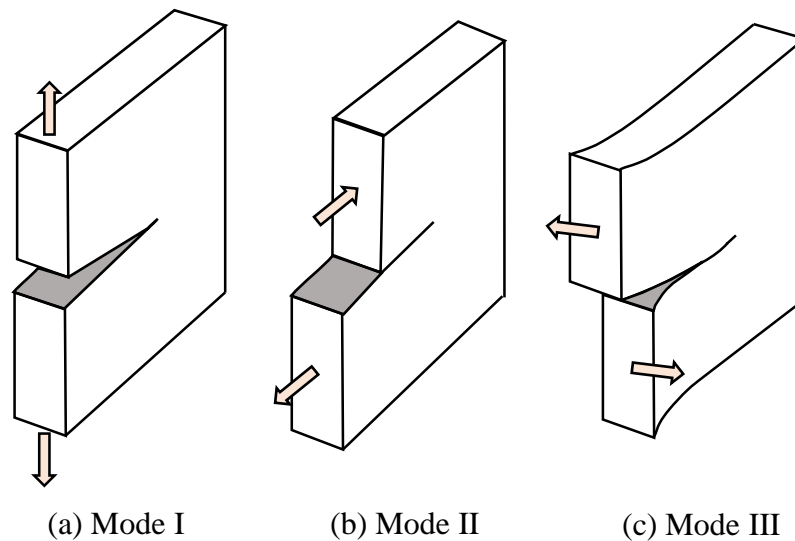


Figure 1.2: Modes of fracture

*Mode II Fracture (Sliding Mode):* Mode II fracture involves the sliding movement of crack surfaces, causing them to shift alongside each other in a shear-like manner (**Figure 1.2(b)**). The shear stress is applied normally to the leading edge of the crack but in the plane of the crack. The primary theory governing Mode II fracture is Elastic-Plastic

Fracture Mechanics (EPFM). EPFM considers the plastic deformation that occurs near the crack's tip and takes into account how the plastic zone affects the crack's growth.

*Mode III Fracture (Tearing Mode):* In Mode III fracture, the surfaces of the crack move parallel to the plane of the crack, resulting in a tearing motion (**Figure 1.2(c)**). Applied shear stress is parallel to the leading edge of the crack. Mode III fracture is less frequent and has received less comprehensive study compared to Mode I and Mode II.

It's important to note that the fracture can involve a combination of these modes, depending on factors like material properties, stress conditions, temperature, loading rate, and the presence of defects. Engineers and materials scientists analyse these different modes to understand the causes of failure and develop strategies to prevent them, especially in critical applications such as aerospace, structural engineering, and manufacturing.

### 1.2.2 Types of fracture

The topic mentioned earlier explores fracture modes, which describes how materials react to different types of loads. Another aspect of fracture revolves around the specific types of fracture, which are influenced by the behaviour of the material [7]. The fracture

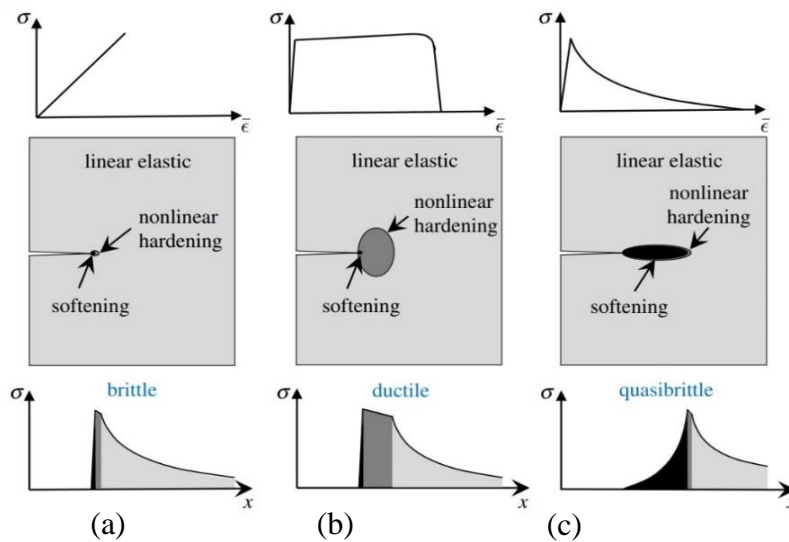


Figure 1.3: Different fracture types: (a) brittle, (b) ductile and (c) quasi-brittle [1].

process reaches its conclusion when crack propagation ceases or, when the body completely fractures into two or more separate parts. The fracture process is categorized into three distinct types (see **Figure 1.3**).

*Brittle Fracture:* Brittle fracture occurs when a material breaks suddenly and without much deformation. This type of fracture usually happens in brittle materials without significant warning and can result in catastrophic failure. Brittle materials tend to have limited ability to absorb energy before breaking. Examples of brittle materials include ceramics and certain types of glass.

*Ductile Fracture:* Ductile fracture involves significant deformation before the material ultimately breaks. Ductile materials can absorb more energy before failing compared to brittle materials. This characteristic is due to the ability of ductile materials to undergo plastic deformation, which allows them to change shape without immediate failure. Common examples of ductile materials include most metals, which can bend and stretch before breaking.

*Quasi-Brittle Fracture:* Quasi-brittle fracture is a behaviour of materials that falls between brittle and ductile fracture. Materials exhibiting quasi-brittle behaviour can undergo some deformation before breaking, but they also exhibit brittle-like characteristics, such as sudden failure without extensive plastic deformation. Concrete and certain types of composite materials are often considered quasi-brittle.

### **1.3 Research Approach and Methodology**

Numerous advanced numerical techniques are documented in the literature to solve the fracture mechanics problems. For instance, the damage models, founded on continuum damage mechanics, utilize the damage variable to represent the fracture state. The damage variable varies from zero (undamaged) to one (completely damaged). Another, smeared approach based method known as Phase Field Method also utilizes a continuous scalar field (the phase field) to depict the fracture state. This field smoothly transits between phases (intact and cracked material) across a characteristic length. Further, in discrete method, the Phantom Node Method, enhances standard meshfree methods by incorporating additional nodes (phantom nodes) to effectively manage discontinuities such as cracks. XFEM, another notable approach, employs enrichment functions to alter standard element shape functions near crack tips, allowing precise modelling of stress singularities. Each numerical method possesses its own set of strengths and weaknesses. The forthcoming chapter titled Literature Review thoroughly explores the pros and cons of various methods rooted in continuum mechanics and fracture mechanics. This research study introduces a novel approach based on a Floating

Node and Smoothing technique, aimed at overcoming the limitations associated with the existing numerical methods.

The Floating Node Method (FNM) is a numerical approach that works on the principles of the discrete crack approach. It introduces additional "floating" nodes that represent discontinuity within elements. The method assigns the position to floating nodes at the intersection of crack and element edges and the additional nodes get activated only for the elements having discontinuity. The FNM can model brittle, quasi-brittle and ductile fracture by incorporating appropriate interface evolution laws. Therefore, the primary objective of this thesis is to formulate an innovative discrete approach by integrating the concepts of the floating node method and the strain smoothing technique. This study introduces a new method known as SFNM for analysing material fracture. SFNM combines the advantages of the floating node method, which positions the floating nodes at the actual crack/discontinuity locations, while the strain smoothing approach eliminates the issues associated with the inverse of Jacobian by converting the area integral into line integral. Thus, the issues associated with element distortion and integration are eliminated in SFNM. The detailed literature on FNM and SFNM is provided in Chapter-2.

#### **1.3.1 Cohesive Zone Modelling**

Addressing the nonlinearity inherent in the fracture process zone ahead of the crack tip necessitates the utilization of cohesive zone models. Cohesive zone models, also known as traction-separation laws or cohesive laws, are used in computational simulations to describe the behaviour of cracks, interfaces, and delamination in materials. These laws are particularly useful in situations where the behaviour of a material at the crack or interface plays a critical role in determining the overall response of the structure. The crack initiation and propagation is based on the cohesive strength, critical crack opening of the interfaces and the fracture energy therefore the fracture problem can be solved with or without the initial crack assumption. The nonlinear nature of the fracture process zone (FPZ) is tackled by the traction separation laws. This model was introduced in the early sixties for metals by Dugdale [8] and Barenblatt [9] for the perfectly brittle materials. The implementation of CZM clubbed with FEM was first presented by Hillerborg [10]. Further, a number of traction separation laws were proposed for the concrete based on the fracture energy. Initially, it was used for brittle materials [11,12] and further extended to the ductile materials [13–15]. The implementation of the

cohesive zone was along the elements and further embedded inside the elements [16]. Using the finite elements based on partition of unity the cohesive crack was implemented to understand the behaviour of the different materials [17–21].

## 1.4 Objectives

This thesis investigates the fracture behaviour of brittle and quasi-brittle materials computationally using the smoothed floating node method. The primary goal is to establish the numerical framework for the smoothed floating node method and application of it to fundamental fracture mechanics problems under mechanical and thermo-mechanical loading conditions. The main objectives of the thesis are summarized as follows:

- To develop the smoothed floating node numerical framework for the failure analysis of 2-D linear elastic bodies.
- To extend the proposed smoothed floating node method for failure analysis of quasi-brittle materials under mechanical loading conditions.
- To predict the fracture behaviour of brittle materials under thermo-elastic loading conditions using the proposed method.
- To develop a numerical framework for the fracture modelling of quasi-brittle materials under thermo-mechanical loading conditions.

## 1.5 Thesis Outline

The complete thesis is summarised in seven chapters. A brief of each chapter is discussed in this section.

### Chapter 1. Introduction

The introduction chapter of this thesis serves as a gateway to the exploration of a highly specialized and critical area of study i.e. fracture mechanics framework for crack modelling using a discrete approach. This chapter is designed to establish the essential groundwork for the subsequent examination of this intricate subject matter. It comprehensively covers all the necessary details for the analysis to follow. It accomplishes this by addressing key components, including the background, motivation, and scope of the research. Furthermore, it outlines the strategic approach that will be adopted to investigate the crack modelling within the context of fracture mechanics using discrete approaches.

### **Chapter 2. Literature Review**

This chapter provides a comprehensive overview of the methods employed to understand and predict crack behaviour in materials. This survey considers mainly two fundamental strategies: the smeared and the discrete approach. The literature review highlights the diverse landscape of crack modelling through an examination of historical development, theoretical frameworks, validation techniques, applications and emerging trends, which offers insights into the balance between understanding theories and computer simulations in the fields of the mechanics of fractures. This chapter emphasizes various computational methods documented in the literature.

### **Chapter 3. Development of SFNM to Model 2D Arbitrary Crack**

This chapter offers an in-depth exploration of the SFNM's foundational structure and practical application. It conducts a rigorous examination of the convergence study involving stress intensity factors and strain energy within diverse material contexts. Furthermore, it positions the SFNM as a favourable option in contrast to other advanced methods, emphasizing its distinct merits in the context of fracture mechanics analysis.

### **Chapter 4. SFNM Implementation with CZM for Quasi-brittle Materials**

This chapter sheds light on the nonlinear fracture process zone that occurs ahead of the crack tip in materials with quasi-brittle characteristics. It provides a comprehensive understanding of the integration of the cohesive zone model with SFNM, offering detailed insights into this combination. First the validation of the framework is verified with the patch test using single element in different mode conditions. The chapter addresses problem-solving for various modes including Mode I, Mode II, and mixed-mode loading conditions.

### **Chapter 5. Thermo-elastic Brittle Fracture using SFNM with CZM**

This chapter focuses on assessing the effectiveness of the SFNM framework when subjected to thermo-elastic loading conditions. It extensively examines how cracks behave, particularly in isothermal and adiabatic thermal scenarios, spanning both homogeneous and nonhomogeneous materials.

### **Chapter 6. Thermo-mechanical Quasi-brittle Fracture**

In this chapter, a combination of thermal and mechanical loading conditions is employed for crack analysis within the discrete approach. Furthermore, the incorporation of the cohesive zone model (CZM) is demonstrated, particularly in the context of quasi-brittle materials. The fracture process zone employs both thermal and mechanical cohesive zone formulations. The chapter entails a comparative assessment of crack propagation



paths across distinct scenarios such as mechanical, thermal, and combined mechanical and thermal loadings.

## **Chapter 7. Conclusions and Future Scope**

This chapter presents a summary of the major conclusions drawn from the presented work. It also highlights the distinctive advantages of the SFNM compared to other advanced finite element-based methods. The possible extensions of the proposed work are also presented in the future scope section of the chapter.

Finally, the references taken from papers, books, websites, etc., have been provided at the end of the dissertation.

Page left blank intentionally

## Chapter 2

### Literature Review

---

This chapter provides a detailed overview of some of the recent developments in the field of fracture mechanics, with particular emphasis on failure models based on continuous, and discontinuous FE frameworks. First, a brief discussion regarding the development of continuous approaches is presented to highlight their advantages and disadvantages. Thereafter, a brief introduction to discrete/discontinuous failure approaches is presented, emphasizing the floating node method. Finally, the last part of this chapter reviews the smoothing procedure and its advantages in numerical analysis of fracture problems.

#### 2.1 Continuous Approach

Continuum damage mechanics is centred on the comprehension and simulation of progressive material degradation caused by internal microstructural damage. It provides a structured framework for analysing the development of damage within a material while considering its mechanical responses. This approach avoids the necessity to model the physical damage in a realistic way. The main advantage of it is that it can include gradual changes in damage within a complex simulation of the failure of a component or structure. Damage is assumed to be a function of local stress or strain, and of time or number of cycles, so it is possible to incorporate the effects of both fatigue and creep, as well as gradual damage accumulation under increasing monotonic loads in quasi-brittle materials. At its core is the introduction of a damage variable which quantifies the extent of material damage on a scale from 0 (undamaged) to 1 (complete failure), capturing the transition from intact to fully damaged states.

The evolution of this damage variable over time, driven by loading and deformation, is governed by an evolution law derived from experimental observations or microstructural considerations. This evolution is incorporated into the material's constitutive equations, enabling the reduction in stiffness and strength due to damage. As the damage variable increases, the material's load-carrying capacity diminishes. Failure criteria are established to define conditions under which failure occurs, often relying on the damage variable surpassing a critical threshold or specific mechanical

properties dropping to defined levels. CDM's predictive capability extends to localizing damage within a material, identifying areas where damage accumulates, leading to crack initiation and propagation. It also seeks to establish the relationship between microstructure, damage evolution, and macroscopic mechanical behaviour by considering factors like voids, inclusions, and micro-cracks. Finally, real-world material behaviour under various loading conditions is validated to ensure accuracy and reliability. Finite Element Analysis (FEA) combined with damage mechanics models enables us to create simulations that closely mimic real-world scenarios. Nevertheless, these models come with certain drawbacks. They often oversimplify damage by representing it as a single value. Yet, in actual situations, different types of damage, like delamination or micro-cracking, can have intricate behaviour and effects. Their responsiveness to factors in the numerical model, such as mesh density, adds another layer of complexity. Typically, these models are applied locally, where the extent of damage in each element is solely influenced by its stress and strain history. Due to their limitations in handling cracking processes, damage mechanics models are generally not used to predict such phenomena.

The preceding explanation offers a comprehensive overview of CDM, and researchers have expanded upon this concept in diverse ways, leading to the development of various techniques aimed at understanding damage mechanics. The subsequent section highlights a subset of these techniques collected from the existing literature.

### 2.1.1 Gradient Damage Models

In the gradient damage model, the material's response is characterized by both the displacement field and the damage field [22–25]. The damage field represents the extent of material degradation at different points within the material. This model is particularly useful for capturing phenomena such as crack initiation, propagation, and branching, which occur in materials under extreme loading conditions. The interaction domain dealing with micro-cracks and fracture process zone introduces a length scale parameter into the formulation, which serves as a localization limiter during strain softening [26]. Gradient damage models introduce a length scale parameter to capture the interaction between intact material and damage, allowing for smoother damage evolution and crack initiation. A length scale parameter relation with damage, in order to satisfy the thermodynamics requirement was suggested in ref. [27]. The gradient damage model

introduces additional governing equations to describe the evolution of the damage field, typically involving partial differential equations. These equations take into account factors such as the stress and strain fields, as well as the gradient of the damage field itself [28]. The model's parameters are determined based on experimental data and physical considerations related to the material being studied. This model finds application in various fields, including solid mechanics, fracture mechanics, and structural engineering, where accurately predicting the failure behaviour of materials is crucial.

Calibrating model parameters can be challenging and relies heavily on experimental data, especially for complex materials. Accurate results may require fine meshes and appropriate mesh configurations to capture localized damage effectively. The model might exhibit numerical instabilities, particularly when abrupt changes in the damage field need to be captured. Incorporating the model into multiscale simulations introduces challenges in data transfer between different scales. Gradient damage models can represent micro-cracks and discontinuities by varying the damage parameter within the material. The length scale parameter in gradient damage models can be used to handle the presence of inclusions and voids, influencing the damage evolution in their vicinity.

### **2.1.2 Peridynamics**

Peridynamics presents a computational modelling paradigm that distinguishes itself from conventional continuum mechanics. It centres on the interactions among material points over finite distances, departing from reliance on local derivatives and differential equations [29,30]. This unique perspective allows peridynamics to effectively handle problems involving crack initiation, propagation, and complex material behaviours that are challenging for classical methods. Peridynamics theory can be broadly divided into two types: bond-based, and state-based peridynamics [31]. Peridynamics was introduced as an extension of continuum mechanics to address challenges associated with cracks and discontinuities. Unlike the local nature of partial differential equations, peridynamics employs integral equations to describe the interactions between material points, which can span considerable distances. This nonlocal behaviour inherently captures long-range interactions, making it an attractive choice for modelling crack propagation and complex material responses. Since its inception, it has been employed in diverse domains. For instance, it finds utility in studying composite materials [32,33]

to predict damage and stress distribution, visco-plasticity [34], thermo-visco-plasticity [35] as well as in the analysis of concrete structures [36]. Notably, peridynamics doesn't require a structured mesh, opting to represent materials via assemblies of material points. This simplifies mesh generation, particularly for intricate geometries. Nonetheless, the computational demand of peridynamics calculations, stemming from nonlocal interactions, restrict its application to specific problems.

### 2.1.3 Phase Field Method

The Phase Field Method (PFM) has emerged as an alternative approach to model fracture problems. PFM, the discontinuity represented by a crack is depicted as damage spread across a regularized region. Various models have been developed within this framework, including physics-based models employing the Ginsberg-Landau phase evolution [37,38], and mechanics-based models grounded in the variational theory of fracture [39]. The latter has proven instrumental in overcoming the limitations of Griffith's approach, particularly in addressing crack nucleation, curvilinear crack path, branching, and other aspects.

The variational approach within PFM involves minimizing the total potential energy concerning the displacement field and a scalar phase variable that governs crack topology evolution [40–44]. To ensure distinct behavior in tensile and compressive fields, literature introduces an additive decomposition of elastic energy density based on volumetric and deviatoric contributions [45,46]. An important contribution to phase-field modeling is Miehe's thermodynamically compatible model, which incorporates principles of continuum mechanics and thermodynamics along with an anisotropic split in strain energy density [47,48]. This model introduces crack irreversibility through the inclusion of a local history field variable. Additionally, Wu et al. have presented a similar anisotropic model featuring a positive-negative decomposition of the effective stress tensor [49]. Phase-field models have found applications in a wide array of fracture scenarios including dynamic problems [50,51], and cohesive fracture problems [52]. Most recently, the hybrid approach, integrating phase field and machine learning, excels in accurately predicting precise structural residual useful life. This is achieved through a phase field and deep-learning based methodology using convolutional neural network (CNN) [53]. A framework for non-deterministic damage prediction in 2D and 3D fracture problems is created, employing a recently developed machine learning technique, specifically the extended support vector regression (X-SVR) [54].

Additionally, adaptive mesh refinement techniques have been devised to enhance both the computational accuracy and efficiency of the phase-field method (PFM) concurrently aiming to refine the elements associated with crack propagation [55–58].

The effectiveness of phase field modelling lies in its ability to simulate a wide range of complex processes, such as solidification, melting, coarsening, and grain growth, across multiple length and time scales [59–61]. It enables the study of intricate microstructural evolution and pattern formation in materials without requiring explicit tracking of interfaces. However, its accuracy is subjected to the careful calibration of parameters and mesh resolution, and large-scale simulations can still be computationally demanding. Despite these challenges, phase field modelling stands as a valuable tool for researchers and engineers to gain insights into the behaviour of materials undergoing phase transitions and evolving interfaces.

## 2.2 Discontinuous Approaches

The other state-of-the-art approach to model the failure is a discrete/discontinuous approach, which gives an explicit representation of failure through discontinuous displacement fields. In this approach, a crack is usually defined as a discrete topological discontinuity represented over a surface, which is introduced separately in the domain. To address failure within a discrete/discontinuous framework, various contributions can be found in the literature based on the fundamentals of linear elastic fracture mechanics and elastic plastic fracture mechanics. The fracture mechanics approaches are briefly discussed in the following paragraphs.

### 1. *Linear Elastic Fracture Mechanics*

Linear Elastic Fracture Mechanics (LEFM) is a fundamental framework used to analyse and understand the behaviour of cracks and fractures in solid materials. It provides a systematic approach for studying the mechanics of brittle materials under the influence of external loads, with a focus on linear elasticity. LEFM is particularly useful for predicting the conditions under which cracks in materials will propagate or remain stable.

The foundation of LEFM lies in the principles of linear elasticity, which assumes that materials deform linearly under small loads and the stress and strain are directly proportional within this elastic range. In the context of fracture mechanics, LEFM introduces concepts like stress intensity factor ( $K$ ), which quantifies the stress field at the crack tip, and fracture toughness ( $K_{Ic}$ ), which characterizes a material's resistance to

crack propagation. The critical value of  $K$  for a material represents the point beyond which crack growth becomes unstable. It is a material-specific parameter that indicates the stress intensity factor required to initiate or propagate a crack. It is important to note that LEFM has limitations, particularly its applicability to brittle materials and small-scale yielding problems. It is less suitable for ductile materials that experience significant plastic deformation. Despite these limitations, LEFM remains a valuable tool in understanding and predicting crack behaviour in a wide range of engineering and materials science applications.

### 2. *Elastic-Plastic Fracture Mechanics*

Most engineering materials show nonlinear elastic or inelastic behaviour under the operating conditions. The elasto-plastic behaviour of the material makes the fracture analysis complex as this implies the existence of two zones; namely, the plastic zone near the crack tip and the elastic zone surrounding the plastic zone. Thus, linear elastic fracture mechanics may not hold good for such materials. The elasto-plastic fracture mechanics is intended to analyse these materials in the presence of large plastic zones. Elasto-plastic crack problems are characterized by other fracture parameters such as crack tip opening displacement and  $J$ -integral.

#### a) *Crack Tip Opening Displacement*

The measurement of fracture toughness by assessing the opening at the crack tip is referred to as Critical Tip Opening Displacement (CTOD). In materials that undergo significant plastic deformation, it is common for the surfaces of cracks to separate prior to fracturing, which is a consequence of the plastic deformation process. The material near the crack tip undergoes plastic deformation in the plastic zone, the square root singularity of stress field does not exist. As the stresses near the crack tip reach a critical value, the crack faces move apart from each other. The CTOD is a measure of the separation of crack faces and quantifies the severity of plastic deformation.

#### b) *J-Contour Integral*

Rice (1968) [62] established a path-independent contour integral to calculate the crack-tip energy release rate, idealizing elastic-plastic deformation as nonlinear elastic. Furthermore, Rice and Rosengren (1968) [63] derived a solution for crack-tip stress and displacement components for materials described by the Ramberg-Osgood relation, representing nonlinear behaviour. The concept of  $J$ -integral received enormous success in modelling the fracture behaviour of ductile materials exhibiting significant plastic



behaviour. In this approach, a generalized energy release rate for nonlinear elastic materials is evaluated.  $J$ -integral is evaluated along an arbitrary line around the crack tip and can be expressed in the form of energy release rate. This fracture parameter is competent enough to analyse both linear elastic and nonlinear elasto-plastic cracked problems.

The preceding explanation provides a comprehensive overview of fracture mechanics approaches, and researchers have extended these concepts in diverse ways, leading to the development of various techniques aimed at understanding fracture mechanics. The subsequent section discusses the applications of fracture mechanics concepts in different numerical techniques for solving fracture problems.

### 2.2.1 Phantom Node Method

Phantom Node Method (PNM) is a mesh-based approach that introduces additional "phantom" nodes to represent cracks and interfaces, enabling the modelling of evolving discontinuities. PNM can represent evolving micro-cracks and discontinuities by assigning additional nodes to describe their shapes and paths. The method updates these nodes as cracks grow. Within this approach, it becomes possible to position a crack tip within an element, enabling nearly independent propagation of cracks regardless of the finite element mesh [64]. To simulate cohesive cracks in quasi-brittle materials, extra displacement degrees of freedom at existing nodes are introduced, enabling the propagation of discontinuities within the elements. This is achieved through the utilization of two distinct sets of standard basis functions. One set is zero on one side of the discontinuity and retains typical values on the opposite side, while the opposite behaviour applies to the other set [65]. PNM, equivalent to standard XFEM, employs the partition of unity concept. It uses a rearrangement of finite element basis and nodal degrees of freedom to represent discontinuities with superimposed elements and phantom nodes. To handle cracks, phantom nodes and superimposed elements are added to the original mesh, while shear bands are addressed by introducing phantom degrees of freedom. This method simplifies the treatment of element-by-element crack and shear band propagation in explicit simulations [66]. Reference [67,68] provides information on the development of PNM and its impressive achievements in modelling the quasi-static failure of composite materials. The qualitative and quantitative investigation of matrix cracking-induced delamination in composite laminates is conducted within a finite element framework, utilizing the phantom node method [69]. In Reference [70],

the investigation of predicting fatigue crack initiation is carried out through the utilization of the extended finite element method employing phantom nodes. Recently, a framework for modelling large deformation contact-impact problems is presented using the phantom-node extended finite element method. This framework incorporates large sliding through a master-slave approach and accounts for large deformations and strains using an updated Lagrangian scheme [71].

However, in this method numerical stability concerns may arise, particularly when simulating dynamic or highly nonlinear scenarios. Furthermore, the incorporation of phantom nodes and the associated increase in degrees of freedom can substantially elevate computational demands, rendering it less suitable for extensive simulations [66]. Consequently, although effective in specific contexts, the phantom node method may not be the ideal selection for all finite element problems.

### 2.2.2 Extended Finite Element Method

The extended Finite Element Method (XFEM), developed by Belytschko and Black [72], is a numerical technique employed to effectively simulate problems characterized by complex discontinuities, such as cracks and interfaces, within finite element analysis. The XFEM approach is particularly advantageous as it obviates the need of conformal remeshing and the fine meshing along the discontinuity, thereby significantly reducing computational costs [73]. Further, the enrichment functions were suggested by Dolbow for a discontinuity to solve 2D elastic problem. Level set method was clubbed with XFEM for the tracking of the discontinuity inside the domain [74–76]. The mechanism of the XFEM approach involves enriching the standard finite element approximation space with additional functions, known as enrichment functions or branch functions [77–80]. These enrichment functions are designed to capture the behaviour of the solution near the discontinuity, enabling accurate representation of stress and displacement fields.

The key parameters in XFEM approach include the choice of enrichment functions, integration schemes for evaluating integrals involving these functions, and the shape of the elements used in the simulation. Enrichment functions are selected based on the type of discontinuity present, and these functions introduce additional degrees of freedom (dofs) associated with the discontinuity. The interface computational analysis is executed using these additional virtual nodes dofs. Further the blending elements enhancing methods were developed to optimise the accuracy and the

convergence rate [81]. XFEM finds application in inhomogeneous materials and composites [82–85], quasi-brittle materials [86], biomaterials [87,88] etc. A detailed overview of the method and its applications can be found in literature [89,90].

However, the accurate treatment of singularities, particularly singularities at the crack tip, remains a challenge in FEM. Special techniques, such as crack tip enrichment functions, are used to address these singularities and improve the accuracy of stress intensity factor calculations in XFEM. However, it introduces in general an error in the representation of the geometry of discontinuities, when mapping the discontinuities from the physical to the natural space [89][64].

### 2.2.3 Element-Free Galerkin Method with geometric discontinuity

The Element-Free Galerkin Method (EFGM) is a numerical technique employed for solving partial differential equations (PDEs) within a computational framework that operates without a predefined mesh [91,92]. Different discontinuity tracking schemes such as visibility criterion, XFEM etc. are employed along with EFGM to solve fracture mechanics problems. Unlike traditional finite element methods, EFGM employs a meshless approach, which eliminates the need for complex mesh generation and refinement processes [93]. In EFGM, the domain is discretized using scattered nodes, often based on a cloud-like distribution, allowing for flexible and adaptive resolution. Only nodal data is required to compute the field variables. Integration in EFGM is typically achieved using techniques such as radial basis functions or moving least squares, enabling efficient handling of spatial derivatives and integrals [94]. The selection of influence areas around nodes plays a crucial role, influencing solution accuracy and stability. Addressing 3D fracture problems with EFGM, involves utilizing a visibility criterion to detect the presence of boundary or geometric discontinuities, while the penalty method is applied to enforce the boundary conditions [95,96]. Simulations of quasi-static fatigue crack growth in both homogeneous and bi-material interfacial cracks are conducted utilizing the Element-Free Galerkin Method (EFGM) under both mechanical and thermo-elastic loading conditions [97,98]. The references [99–101] contain examples of additional fracture problems that have been modeled using both the meshfree method and the extended finite element method.

The meshless approach finds application in various fields, including fluid dynamics, solid mechanics, and heat transfer, offering a promising alternative to conventional numerical methods [95,98,102]. A limitation of the EFGM arises when employing a

single integration point within a domain, as this choice could potentially result in instability due to the presence of higher-order shape functions. Moreover, the computation of shape functions is time consuming, hence makes it computationally inefficient.

### 2.2.4 Crack Particle Method

The Crack Particle Method (CPM) is a mesh-free approach that represents a crack as a set of cracked particles. Cracked segments model discrete cracks, employing a discontinuous enrichment that can be aligned arbitrarily at each node within the body. To account for displacement discontinuity, additional unknowns are introduced in the variational formulation [103]. An additional enhancement in this method involves the detection of cracking, where particles are divided into two, positioned on opposite sides of the crack. To accurately depict the jump in the displacement field, the shape functions of particles adjacent to cohesive crack segments are intersected across the crack boundary, similar to the visibility method. CPM is developed further to incorporate the Configurational Forces(CF) approach instead of using maximum circumferential stress criterion for crack propagation [104]. The method has been expanded to address cracks with significant curvatures through the incorporation of bilinear segments in the two-dimensional framework [105]. The CPM is employed in various fields, including dynamic fracture, ductile fracture, and the simulation of multiple cracks.

### 2.2.5 Floating Node Method

The floating node method represents a refined advancement over the XFEM and phantom node method with respect to simulating structural discontinuities. Unlike the XFEM and PNM, where supplementary nodes align with the standard nodes' coordinates within the cracked element, the FNM takes a different approach. In the case of the FNM, each element incorporates standard nodes alongside dormant floating nodes, which do not possess specific coordinate positions within the element. During instances involving an un-cracked structure, these additional nodes remain inactive, causing the element to behave comparably to a typical finite element. However, when a discontinuity arises within a specific element, the corresponding floating nodes become active and dynamically assume positions based on the crack's orientation. This adaptation allows the FNM to effectively model the development of structural failures in composite materials [4,106,107], brittle fracture [5,108] showcasing its relevance in progressive failure analysis. A novel numerical framework utilizing the floating node

method is introduced for investigating delamination migration problems. This approach involves the insertion of discrete cohesive cracks into a single element to provide multiple potential crack paths [109]. Thereafter, an implementation of a floating node method with strong discontinuities in laminated composites under large deformations is also introduced where enriched solid and cohesive elements are employed to handle matrix cracking and delamination through a mixed-mode cohesive model [110]. Recently, a numerical approach for analysing multiple fatigue-induced delamination cracks is developed, which includes a cohesive zone model along with an Adaptive Refinement Scheme (ARS) and an Adaptive Floating Node Method (A-FNM). This integrated approach effectively refines the model during the analysis process [111].

### 2.2.6 Strain Smoothing Approach

Chen et al. [112] originally introduced the concept of strain smoothing within meshfree methods, which was subsequently extended into the framework of FEM [113–116]. The technique of strain smoothing offers the potential for enhancing accuracy and convergence rates in comparison to the conventional finite element approach. This advantage becomes particularly pronounced in scenarios involving singularities or distorted meshes, and all of this is achieved at a reduced computational expense. This innovative technique circumvents the necessity of computing and inverting the Jacobian matrix for each element or sub-element, thereby contributing to its computational efficiency. The strategy for applying strain smoothing presents various options, including node-based smoothing [117], cell-based smoothing [118,119], face-based smoothing [120], and edge-based smoothing [121]. These options allow for flexible adaptation to different problem scenarios. This approach has been successfully employed to address problems featuring singular stress fields of arbitrary order [122]. Moreover, the technique is seamlessly integrated with the phase field method to analyse brittle fracture through dedicated subroutines [123]. Two distinct Smoothed Finite Element Methods (SFEMs), referred to as NS-FEM and CS-FEM, are developed to address topology optimization challenges involving both compressible and incompressible materials [124]. The extension of a cell-based smoothed three-node Mindlin plate element (CS-FEM-MIN3) is implemented for the geometrically nonlinear analysis of laminated composite plates [119]. Furthermore, the application of this concept extends to the enhancement of performance in standard three-noded constant strain triangular elements [125].

Based on the literature, the continuum damage mechanics approach is recognized for its effectiveness at the micro-level but it encounters limitations at the macro-level, prompting the utilization of discrete crack approaches. The preceding sections explore numerous advanced discrete methods. Despite significant progress in advanced discrete approaches, there remains a challenging research gap in developing advanced numerical models capable of addressing diverse brittle, quasi-brittle fracture scenarios and complex thermo-mechanical loading conditions. Therefore, additional research contributions in this direction are still required.

### **2.2.7 Boundary Element Method**

The Boundary Element Method, also referred to as the Boundary Integral Equation Method, is a numerical approach that focuses on the domain's boundary instead of partitioning the entire domain into elements. This method is applicable to linear partial differential equations (PDEs), wherein the solution within a specific region's interior is entirely determined by values at the boundary. In contrast to finite element methods, which transform PDEs into linear algebra problems by dividing the domain into elements, boundary element methods operate on elements situated on the domain's boundary. BEM proves particularly advantageous in scenarios involving infinite domains or situations where the solution is only required along the boundary. By reducing the dimensionality of the problem, BEM enhances computational efficiency for specific types of applications. Application of BEM for fracture mechanics problems in orthotropic bodies [126] and anisotropic composite laminates [127] is presented for stress intensity factor calculation. BEM formulation for 2-D problems is presented in the field of magneto-electroelastic to analyse crack problems [128,129].

Another technique rooted in the BEM is the Scaled Boundary Finite Element Method (SBFEM) that combines the features of both the boundary element method (BEM) and the finite element method (FEM). The Scaled Boundary Finite Element Method is particularly useful for solving problems related to elastic wave propagation, structural dynamics, and acoustics. In SBFEM, the domain of interest is divided into two regions: an inner region, where the problem is solved using traditional finite elements, and an outer region or boundary, where the problem is addressed using the boundary element method. The finite element mesh is confined to the interior of the domain, while the boundary elements are employed along the domain's boundary.

## Chapter 3

### Development of SFNM to Model 2D Arbitrary Crack

---

In this chapter, Floating Node Method (FNM), is coupled with cell-wise strain Smoothed Finite Element Method (SFEM) for modelling 2D linear elastic fracture mechanics problems. The proposed method is termed as Smoothed Floating Node Method (SFNM), where FNM is used to represent the kinematics of crack and the crack front inside the domain without the requirement of remeshing and discontinuous enrichment functions during crack growth. For smoothing, a constant smoothing function is considered over the smoothing domains through which classical domain integration changes to line integration along each boundary of the smoothing cell, thus derivative of shape functions are not required in the computation of the field gradients. The values of stress intensity factor are obtained from the SFNM solution using domain based interaction integral approach. Few standard fracture mechanics problems are considered to check the accuracy and effectiveness of the proposed method.

#### 3.1 Introduction

Defects such as cracks and voids are inevitable in the engineering materials and are mainly responsible for the fracture and failure of materials during the service. Therefore, it is important to study the amalgamation of the inherent micro cracks and voids, crack initiation and propagation of cracks in the structural components to predict the life span. The FEM can be the best suited numerical tool to carry out such simulations of fracture mechanics problems. In FEM, mapped element takes part as a paired set between physical and natural coordinate system to maintain the exact equivalence. Thus, element distortion is not permitted as it causes singularity in the inversion of stiffness matrix. Moreover, in simulations of crack propagation behaviour using FEM, conformal meshing is required to capture the crack discontinuity [72]. This mesh update in the crack tip vicinity corresponding to crack growth makes the simulation complex and time consuming. In addition to this, remeshing during crack growth introduces error while transferring the field variables data from the previous mesh to the new one. Therefore, it becomes cumbersome to model crack propagation and evolving discontinuity using



FEM approach alone. A more robust framework is desirable for the prediction of progressive failure. To this end, efforts have been made by researchers to establish different advanced numerical methods, such as the meshfree method, extended finite element method, phantom node method, boundary element method, isogeometric analysis, floating node method, continuum damage models, Phase Field Method etc. The detailed review of these numerical approaches is provided in Chapter-2.

Recently, floating node method is proposed based on the development of PNM, which has similar computational architecture to PNM, but the locations of additional nodes do not need to be fixed. These additional nodes are called floating nodes that move to the crack-edge intersections to form the crack by partitioning the original element into sub-elements. The complex crack networks can be modelled in an element by forming sub-elements that are conformal to the cracks. So far, FNM has been extended for numerous fracture problems, ranging from single crack to multiple crack problems on isotropic [130] and composite materials [4,131]. The FNM alleviates the limitations such as remeshing during crack propagation, enrichment functions requirement, error during mapping the discontinuity from physical to natural space etc. Despite its success in fracture problems, there exists some limitations during integration where during mapping a basic requirement is that the element has to be convex and severe distortion is not acceptable so that a one-to-one coordinates correspondence between physical and natural space associated with element can be guaranteed. More precisely, no interior angle should be greater than  $180^\circ$  for a 2D four node element and the positivity of the Jacobian determinant should be ensured in numerical implementation [132], which increases the computational cost. Moreover, the modelling of arbitrary crack in FNM is cumbersome as in FNM a crack divides the intact element into sub-elements. Sometimes these sub-elements may have poor aspect ratio depending on the crack direction, which deteriorates the convergence rate during the simulations. To alleviate this issue, Kumar et al. [14] considered one additional floating node in each standard element to maintain the aspect ratio of the sub-elements within the acceptable limit. To overcome these issues of integration, Liu et al. [6] proposed a smoothed finite element method by combining the FEM with strain smoothing technique of meshfree methods. In this approach, smoothing operations are performed over the elements, which eliminates the requirement of Jacobian determinant during numerical integration. The strain smoothing concept is further extended with FEM [133] and XFEM [134,135]



for solving fracture problems. Though, by combining the smoothing procedures with FEM and XFEM, the requirement of mapping and positive Jacobian determinant during numerical integration is eliminated, the methods still suffer with the limitations associated with their basic framework, discussed in respective sections.

To overcome the limitations associated with FEM, XFEM, XIGA, PNM, FNM, a new approach called as Smoothed Floating Node Method (SFNM) is proposed by combining the FNM with strain smoothing technique. In SFNM, FNM is used to represent the kinematics of crack, and the system stiffness matrix is calculated by using the strain smoothing technique over the domain of the smoothing cell associated with the element. The values of stress intensity factor (SIF) are obtained from the SFNM solution using domain based interaction integral approach. The major features of the proposed method are as follows:

- No requirement of remeshing and enrichment functions to model the static and crack propagation behaviour.
- Less sensitive to the element distortion due to the absence of isoparametric mapping.
- Unlike XFEM, no mixed terms of stiffness occur, that results in better conditioning.
- Simplify integration by transforming domain integration on Gauss points into line integration along the edges.
- Shape function derivatives are not required for the field variable gradient matrix.
- Element convexity restriction is less sensitive to the computational procedure, and maintaining the aspect ratio of the sub-divided elements in SFNM becomes redundant.

To implement the proposed method, certain assumptions are considered, as outlined below.

- Discretization of the domain into elements is a common practice in simulations, with the assumption of a uniform structural mesh.
- Simulations assume small deformations, where the strains remain within the elastic range.
- The material is considered to be homogeneous and isotropic, indicating uniform properties in all directions.

- 
- Fracture mechanics simulations assume either plane stress or plane strain conditions, simplifying the problem by reducing it from three dimensions to two.
  - Problem-solving focuses on a specified initial crack, neglecting interactions between multiple cracks in the simulations.
  - Material properties are assumed to remain constant throughout the simulation.
  - The proposed method assumes the capture of the crack tip on any one edge of the element.

To demonstrate the effectiveness of the proposed approach, three benchmark fracture mechanics problems are solved, and the results obtained by SFNM are compared with the available literature/theoretical results. In the first problem, an edge cracked plate under mode-I loading is considered and the relative error in SIF and strain energy are obtained. The second problem deals with an edge cracked plate under mode-II loading condition. The error in SIF and strain energy are obtained and compared. In the third problem, a bi-material specimen having interfacial edge crack subjected to mode-I loading is solved.

The chapter is organized as follows: Section 3.2 describes the governing equations and mathematical formulation of SFNM and smoothing technique. Section 3.3 and Section 3.4 contain the SIF computation and crack growth criterion respectively. The numerical problems are presented in Section 3.5 to demonstrate the effectiveness of the SFNM framework. Finally, the conclusions obtained through numerical simulations are provided in Section 3.6.

## 3.2 Numerical Formulation

In this section, the governing equations for the static analysis of an elastic medium containing a traction free crack are briefly discussed. A brief review of FNM and SFEM is also presented for completeness. Further, the shape function generation, numerical integration procedure in SFNM and its implementation procedure is discussed.

### 3.2.1 Governing equations for elasto-statics

Consider a linear elastic body with a discontinuity as shown in **Figure 3.1**. The domain  $\Omega$  is divided into three parts  $\Gamma_u$  where the displacement boundary conditions are applied,  $\Gamma_t$  where the traction boundary conditions are applied and  $\Gamma_{cr}$  which is the traction free surface representing the discontinuity.

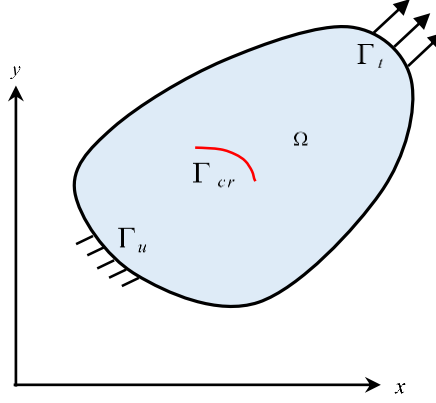


Figure 3.1: A cracked domain with boundary conditions

The strong form of the static equilibrium equation along with the boundary conditions are given as,

$$\nabla \cdot \boldsymbol{\sigma} + \mathbf{b} = \mathbf{0} \text{ in } \Omega \quad (3.1)$$

$$\boldsymbol{\sigma} \cdot \hat{\mathbf{n}} = \bar{\mathbf{t}} \text{ on } \Gamma_t \quad (3.2a)$$

$$\boldsymbol{\sigma} \cdot \hat{\mathbf{n}} = \mathbf{0} \text{ on } \Gamma_{cr} \quad (3.2b)$$

$$\mathbf{u} = \bar{\mathbf{u}} \text{ on } \Gamma_u \quad (3.2c)$$

where  $\nabla$  is the gradient operator,  $\boldsymbol{\sigma}$  is the Cauchy stress tensor,  $\mathbf{b}$  is the body force vector per unit volume,  $\hat{\mathbf{n}}$  is the unit outward normal and  $\bar{\mathbf{t}}$  is the applied traction vector. For small strains and displacements, the strain-displacement relation can be written as,

$$\boldsymbol{\varepsilon} = \boldsymbol{\varepsilon}(\mathbf{u}) = \nabla^s \mathbf{u} \quad (3.3)$$

where  $\nabla^s$  is the symmetric part of the gradient operator. The constitutive relation for linear elastic material is given by Hooke's law,

$$\boldsymbol{\sigma} = \mathbf{D} \boldsymbol{\varepsilon} \quad (3.4)$$

where  $\mathbf{D}$  is the material elasticity tensor.

By substituting the constitutive relation and the strain-displacement relation, the weak form of the equilibrium equation can be expressed as,

$$\int_{\Omega} \boldsymbol{\sigma}(\mathbf{u}) : \boldsymbol{\varepsilon}(\mathbf{v}) d\Omega = \int_{\Omega} \mathbf{b} \cdot \mathbf{v} d\Omega + \int_{\Gamma_t} \bar{\mathbf{t}} \cdot \mathbf{v} d\Gamma \quad (3.5)$$

where  $\mathbf{u}$  and  $\mathbf{v}$  are the displacement trial and the test functions, respectively. Upon discretization of  $\mathbf{u}$  and  $\mathbf{v}$ , the above weak form can be transformed into the following discrete set of equations,

$$\mathbf{K}\mathbf{d} = \mathbf{f} \quad (3.6)$$

where  $\mathbf{K}$  is the global stiffness matrix,  $\mathbf{d}$  is the nodal displacements vector and  $\mathbf{f}$  is the external applied force vector.

### 3.2.2 Basic formulation of FNM

In FNM, each real node is characterized by its nodal coordinates and its associated dofs, and each element in the domain also contains a suitable number of floating dofs. Thus, discretized mesh contains of either intact element, or elements that encompasses a crack/discontinuity. The floating nodes in the intact element are dormant and the element thus identical to the standard finite element. Once a crack appears inside the intact element, the floating nodes get activated to model the crack in the element. The nodal position vectors of the floating nodes are defined by the crack position coordinates (points with coordinates  $\mathbf{x}_r$  and  $\mathbf{x}_s$ ), refer **Figure 3.2**. Hence, the cracked element is split into two sub-elements  $\Omega_A$  and  $\Omega_B$ , depending on the direction of the crack [106]. The vectors of nodal coordinates of sub-elements are defined as,

$$\mathbf{x}_{\Omega_A}^T = [\mathbf{x}_r^T, \mathbf{x}_s^T, \mathbf{x}_3^T, \mathbf{x}_4^T] \quad \text{and} \quad \mathbf{x}_{\Omega_B}^T = [\mathbf{x}_1^T, \mathbf{x}_2^T, \mathbf{x}_s^T, \mathbf{x}_r^T] \quad (3.7)$$

Now, each sub-element ( $\Omega_A$  and  $\Omega_B$ ) has a separate Jacobian given as,

$$\mathbf{J}_A = \frac{d\mathbf{x}}{d\xi} = \frac{d\mathbf{N}}{d\xi} \mathbf{x}_{\Omega_A} \quad \text{and} \quad \mathbf{J}_B = \frac{d\mathbf{x}}{d\xi} = \frac{d\mathbf{N}}{d\xi} \mathbf{x}_{\Omega_B} \quad (3.8)$$

The displacement  $\mathbf{u}_A$  and  $\mathbf{u}_B$  in the sub-elements are interpolated separately from the respective degrees of freedom  $\mathbf{d}_A$  and  $\mathbf{d}_B$  of the sub-element  $\Omega_A$  and  $\Omega_B$  respectively,

$$\mathbf{u}_A = \mathbf{N}\mathbf{d}_A \quad \text{and} \quad \mathbf{u}_B = \mathbf{N}\mathbf{d}_B \quad (3.9)$$

where  $\mathbf{d}_A^T = [\mathbf{d}_7^T, \mathbf{d}_8^T, \mathbf{d}_3^T, \mathbf{d}_4^T]$  and  $\mathbf{d}_B^T = [\mathbf{d}_1^T, \mathbf{d}_2^T, \mathbf{d}_5^T, \mathbf{d}_6^T]$

The stiffness matrices and force vectors of the sub-elements are thus defined as,

$$\mathbf{K}_A = \int_{\Omega_A} \mathbf{B}_A^T \mathbf{D} \mathbf{B}_A d\Omega \quad \text{and} \quad \mathbf{K}_B = \int_{\Omega_B} \mathbf{B}_B^T \mathbf{D} \mathbf{B}_B d\Omega \quad (3.10)$$

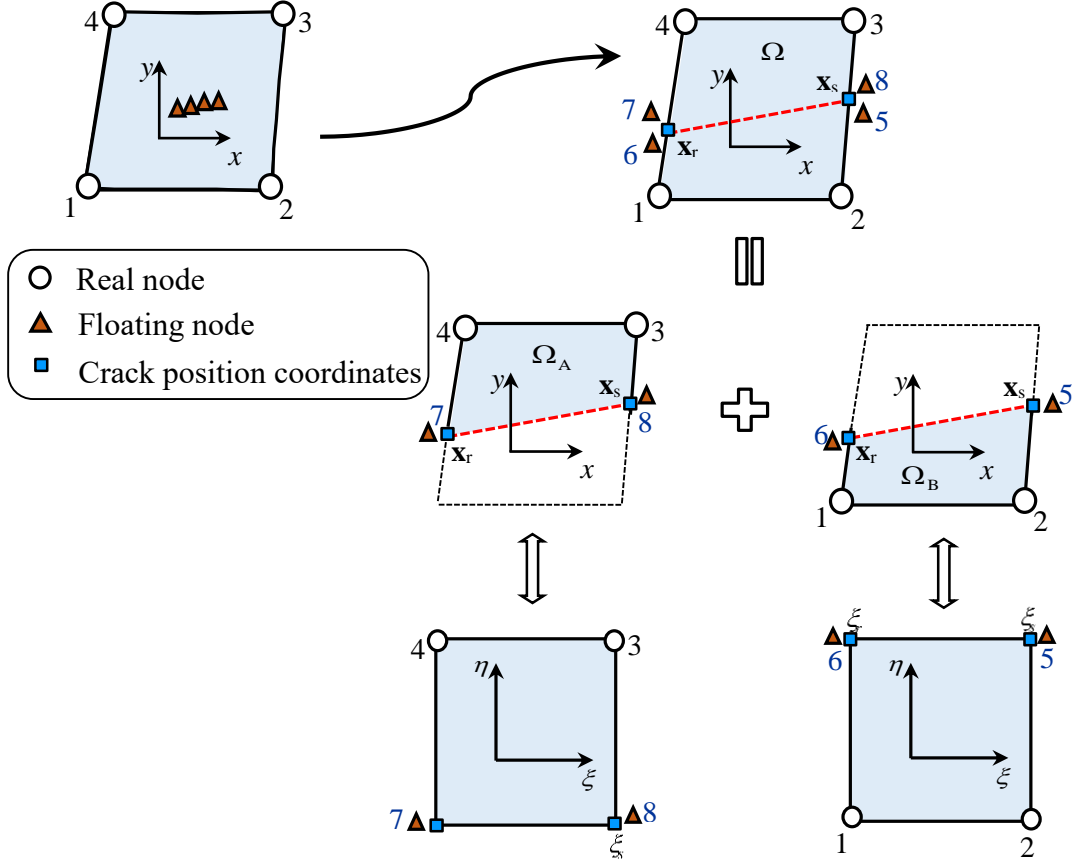


Figure 3.2: A schematic representation of strong discontinuity modelling in an element using floating node method.

$$\mathbf{f}_A = \int_{\Omega_A} \mathbf{N}^T \mathbf{b} d\Omega + \int_{\Gamma_t \cap \Gamma_{\Omega_A}} \mathbf{N}^T \bar{\mathbf{t}} d\Gamma \quad (3.11a)$$

$$\mathbf{f}_B = \int_{\Omega_B} \mathbf{N}^T \mathbf{b} d\Omega + \int_{\Gamma_t \cap \Gamma_{\Omega_B}} \mathbf{N}^T \bar{\mathbf{t}} d\Gamma \quad (3.11b)$$

The equilibrium equations for both sub-elements are written as,

$$\mathbf{K}_A \mathbf{d}_A = \mathbf{f}_A \quad \text{and} \quad \mathbf{K}_B \mathbf{d}_B = \mathbf{f}_B \quad (3.12)$$

Finally, the equilibrium equation of the floating node element is the assembly of the two sub-elements, and given as,

$$\mathbf{K} \mathbf{d} = \mathbf{f} \quad (3.13)$$

where  $\mathbf{K} = \begin{bmatrix} \mathbf{K}_A & \\ & \mathbf{K}_B \end{bmatrix}$ ,  $\mathbf{d}^T = [\mathbf{d}_A^T, \mathbf{d}_B^T]$  and  $\mathbf{f}^T = [\mathbf{f}_A^T, \mathbf{f}_B^T]$  when the two sub-

elements are fully separated.

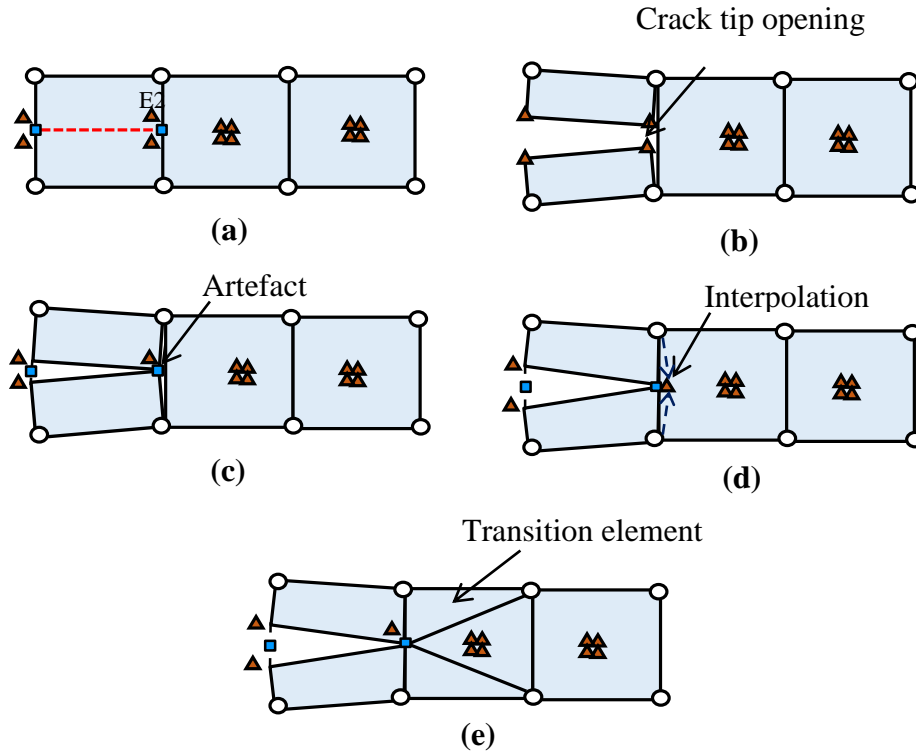


Figure 3.3: Crack tip modelling in floating node

The crack tip modelling in FNM is very important aspect for failure analysis of a structure. In FNM, each individual element has the floating nodes either dormant or activated. The crack is modelled by splitting the intact element into two sub-elements by activating the floating nodes, and positioning them to the points obtained from the intersection of crack with the element edge. The split element has two floating nodes at the edge E2 of the intact element, where the crack terminates, refer **Figure 3.3(a)**. Therefore, the crack tip remains open at the edge E2 as shown in **Figure 3.3(b)**. Though the crack tip can be modelled by considering two sets of dofs from both floating nodes at the crack tip to be identical, this procedure may lead to an artefact at the crack tip as shown in **Figure 3.3(c)**, i.e. the split elements at the crack tip do not have adequate topology for connecting with the adjacent intact element, resulting in a lack of displacement compatibility at the element edge E2. To alleviate this issue, the dofs at the crack tip are interpolated from the neighbouring dofs as illustrated in **Figure 3.3(d)**. Hence, the intact element adjacent to crack tip is considered as a transition element (refer **Figure 3.3(e)**) to maintain the displacement compatibility between the split element and intact element. The detailed procedure can be found in literature [14]. The transition

element is considered at the crack tip which is further divided into triangular elements to improve the accuracy of the results.

### 3.2.3 Strain smoothing technique

The strain smoothing was first introduced by Chen et al. [112] for meshfree methods, and later extended in the framework of FEM [113–116,133]. The strain smoothing technique can achieve higher accuracy and convergence rates than the standard finite element method, especially in the presence of singularities or distorted meshes, for a slightly smaller computational cost. In the meshfree method based on nodal integration form, the integration in **Eq. (3.5)** is performed over representative cells of nodes in the problem domain. To guarantee the convergence of the solution, the linear exactness in the solution of the weak form should be ensured. To meet this requisite, the following integration constraint should be satisfied [112,136],

$$\int_{\Omega} \mathbf{B}_I^T(\mathbf{x}) d\Omega = \int_{\Gamma_t} \mathbf{N}_I^T(\mathbf{x}) d\Gamma \quad (3.14)$$

$$\text{With} \quad \mathbf{B}_I = \begin{bmatrix} N_{I,1} & 0 \\ 0 & N_{I,2} \\ N_{I,2} & N_{I,1} \end{bmatrix}, \quad \mathbf{N}_I = \begin{bmatrix} N_I n_1 & 0 \\ 0 & N_I n_2 \\ N_I n_2 & N_I n_1 \end{bmatrix} \quad (3.15)$$

where  $\mathbf{B}_I$  is the standard gradient matrix of node  $I$ ,  $N_I$  is the shape function of node  $I$ ,  $n_1$  and  $n_2$  are the first and second components of the outward boundary normal vector of the smoothing cell. This condition is met by applying strain smoothing techniques for each representative nodal cell.

The motivation of this work is to develop a Smoothed FNM (SFNM) by incorporating the strain smoothing technique in the framework of FNM. In SFNM, sub-elements are formed as in the FNM, but they are further subdivided into several smoothing subcells (see **Figure 3.4**) and integrated using the smoothing technique to elevate distortion sensitivity. When choosing a constant smoothing function, area integration over the subcell becomes line integration along its boundaries, and no gradient of shape functions is required in computing the field gradients or in forming the stiffness matrix. The integration along the edges of each subcell is done numerically using 1D Gauss integration scheme. **Figure 3.5** shows the field nodes and integration points corresponding to different number of subcells. A smoothing operation is performed to the gradient of displacement for all the subcells in an element.

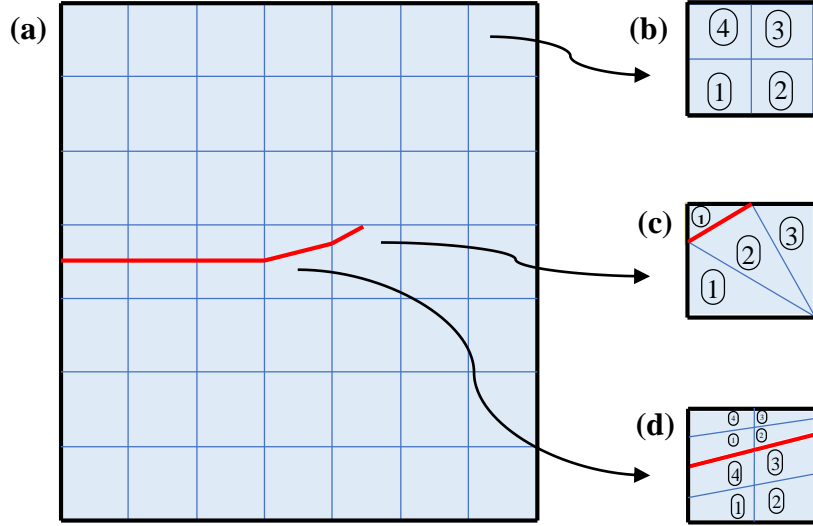


Figure 3.4: Schematic of subcells formation for integration in SFNM: (a) crack growth in domain (b) intact element subcells (c) 2 sub-elements with inclined crack path and further subdivision into triangular subcells and (d) 2 quadrilateral sub-elements with inclined crack path and further subdivision into quadrilateral subcells.

Let  $u$  represent the displacement along a certain direction, the smoothing operation for its gradient at a point  $\mathbf{x}_c$  (belonging to a subcell domain  $\Omega_C$ ) is given as,

$$\tilde{\nabla}u(\mathbf{x}_c) = \int_{\Omega} \nabla u(\mathbf{x}) \phi(\mathbf{x} - \mathbf{x}_c) d\Omega \quad (3.16)$$

Using Integration by parts, the right-hand side of **Eq. (3.16)** becomes

$$\tilde{\nabla}u(\mathbf{x}_c) = \int_{\Gamma} u(\mathbf{x}) \mathbf{n}(\mathbf{x}) \phi(\mathbf{x} - \mathbf{x}_c) d\Gamma - \int_{\Omega} u(\mathbf{x}) \nabla \phi(\mathbf{x} - \mathbf{x}_c) d\Omega \quad (3.17)$$

where  $\phi$  is a smoothing function. A piecewise constant smoothing function is considered here, which is constant within  $\Omega_C$  and vanish everywhere else,

$$\phi(\mathbf{x} - \mathbf{x}_c) = \begin{cases} 1/A_C & \mathbf{x} \in \Omega_C \\ 0 & \mathbf{x} \notin \Omega_C \end{cases} \quad (3.18)$$

where  $A_C = \int_{\Omega_C} d\Omega$ .

The second term of the right hand side of **Eq. (3.17)** vanishes with the chosen  $\phi$ . Substituting  $\phi$  into **Eq. (3.17)**, we get the smoothed gradient of displacement as,

$$\tilde{\nabla}u(\mathbf{x}_c) = \int_{\Gamma_C} u(\mathbf{x}) \mathbf{n}(\mathbf{x}) \phi(\mathbf{x} - \mathbf{x}_c) d\Gamma = \frac{1}{A_C} \int_{\Gamma_C} u(\mathbf{x}) \mathbf{n}(\mathbf{x}) d\Gamma \quad (3.19)$$



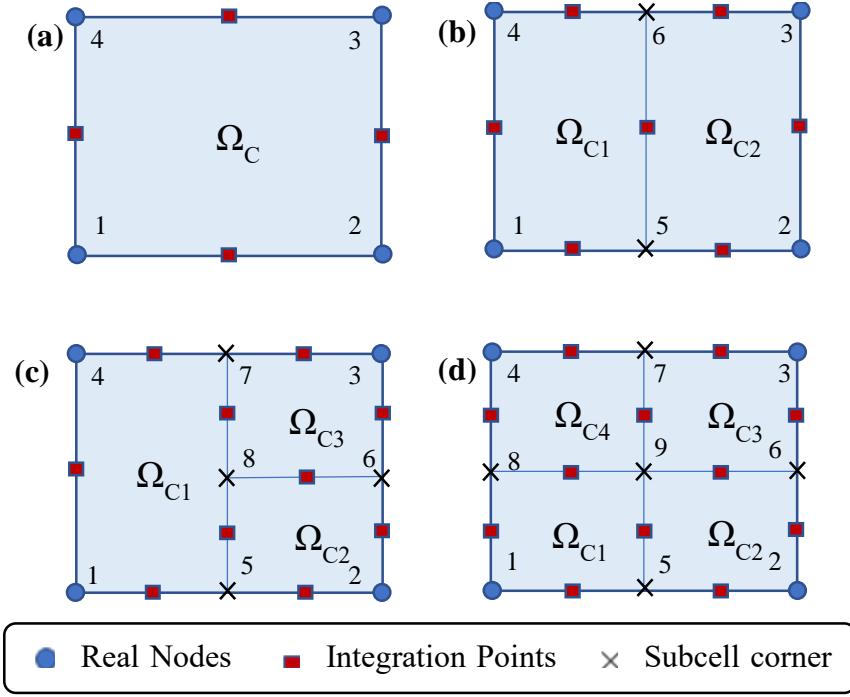


Figure 3.5: Quadratic element division into smoothing subcells and integration scheme: (a) 1-subcell (b) 2-subcells (c) 3-subcells and (d) 4-subcells.

where  $\Gamma_c$  is the boundary of the smoothing subcell. Here, the choice of piece-wise constant smoothing function  $\phi$  converts the area integration (Eq. (3.16)) into line integration along the edges of the subcell. The smoothed displacement gradient becomes independent of  $\mathbf{x}_c$ , i.e., constant within  $\Omega_c$ . Repeating the above procedure for the displacement vector  $\mathbf{u}$  and substituting the smoothed gradients into Eq. (3.3), the smoothed strain at  $\mathbf{x}_c$  can be obtained as,

$$\tilde{\boldsymbol{\epsilon}}(\mathbf{x}_c) = \sum_{I=1}^n \tilde{\mathbf{B}}_I(\mathbf{x}_c) \mathbf{d}_I \quad (3.20)$$

where  $n$  is the number of nodes and  $\tilde{\mathbf{B}}_I$  is the smoothed strain matrix of node  $I$ . For 2D, it is written as,

$$\tilde{\mathbf{B}}_I(\mathbf{x}_c) = \begin{bmatrix} \tilde{b}_{I1}(\mathbf{x}_c) & 0 \\ 0 & \tilde{b}_{I2}(\mathbf{x}_c) \\ \tilde{b}_{I2}(\mathbf{x}_c) & \tilde{b}_{I1}(\mathbf{x}_c) \end{bmatrix} \quad (3.21)$$

$$\text{where } \tilde{b}_{Ik}(\mathbf{x}_c) = \frac{1}{A_c} \int_{\Gamma_c} N_I(\mathbf{x}) n_k(\mathbf{x}) d\Gamma, \quad (k = 1, 2)$$

If one Gaussian point is used for line integration along each segment of the boundary  $\Gamma_i^C$  of  $\Omega_C$ , the above equation can be transformed to its algebraic form as,

$$\tilde{b}_{Ik}(\mathbf{x}_c) = \sum_{i=1}^M N_I(\mathbf{x}_i^{GP}) n_{ik}^C l_i^C \quad (3.22)$$

where  $M$  is the number of boundary segments,  $\mathbf{x}_i^{GP}$  is the Gaussian point of the  $i^{\text{th}}$  boundary segment  $\Gamma_i^C$ ,  $l_i^C$  is the length and  $n_i^C$  the outward unit normal vector of  $\Gamma_i^C$ , respectively. Once the smoothed gradient matrix over each subcell is evaluated, the smoothed element stiffness matrix of the sub-element  $e$  of SFNM can be obtained by assembly from all the subcells in the element as,

$$\mathbf{K}_e^{\text{SFNM}} = \sum_{\forall C \in e} \tilde{\mathbf{B}}_C^T \mathbf{D} \tilde{\mathbf{B}}_C A_C \quad (3.23)$$

where  $\tilde{\mathbf{B}}_C$  (i.e.,  $[\tilde{\mathbf{B}}_1(\mathbf{x}_c), \dots, \tilde{\mathbf{B}}_n(\mathbf{x}_c)]$ ) is the smoothed gradient matrix of the subcell  $C$ . Now, the final discretized algebraic system of equation for the split elements can be written as,

$$\mathbf{K}_A^{\text{SFNM}} \mathbf{d}_A = \mathbf{f}_A \quad \text{and} \quad \mathbf{K}_B^{\text{SFNM}} \mathbf{d}_B = \mathbf{f}_B \quad (3.24)$$

Finally, the algebraic equation of SFNM is the assembly of the two sub-elements,

$$\mathbf{K}^{\text{SFNM}} \mathbf{d} = \mathbf{f} \quad (3.25)$$

$$\text{where } \mathbf{K}^{\text{SFNM}} = \begin{bmatrix} \mathbf{K}_A^{\text{SFNM}} & \\ & \mathbf{K}_B^{\text{SFNM}} \end{bmatrix}$$

### 3.2.4 Shape function construction and numerical integration scheme

In this section, we focus on the construction of the shape functions and integration scheme for the elements used in SFNM. In SFNM, both 4-node quadrilateral and 3-node triangular elements are used for the numerical simulations as shown in **Figure 3.4**. The number of subcells in an element depends on the required accuracy. In this work during smoothing procedure, 4-node quadrilateral element is divided into 4-subcells, however the procedure for dividing the quadrilateral element from 1-subcell to 4-subcells is discussed and illustrated in **Figure 3.5**. Similarly, the 3-node triangular element is divided into 1-subcell during the simulations, but the procedure to divide it into 1-

subcell and 4-suncells is illustrated in **Figure 3.6**. For generalization. It is observed that SFEM solution using 1-subcell is equivalent to the FEM reduced integration [133]. The explicit shape functions themselves are used at the nodal points. The shape functions are interpolated simply by a linear function at any point on the boundary. For example, in **Figure 3.5(b)** the element is divided into 2-subcells and the nodal points (1, 2, 3, 4)

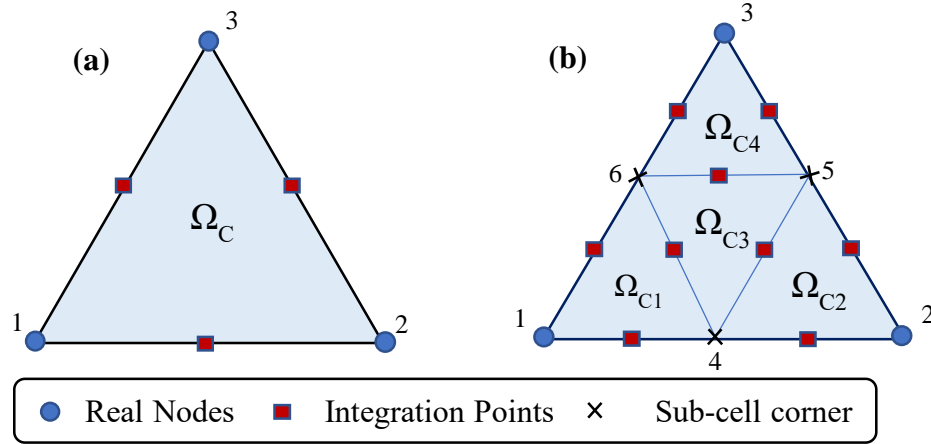


Figure 3.6: Triangular element division into smoothing subcells and integration scheme, (a) 1-subcell (b) 4-subcells.

Table 3.1: Shape function value at different sites within SC4Q4 element (**Figure 3.5(d)**)

SITE	NODE 1	NODE 2	NODE 3	NODE 4	DESCRIPTION
1	1	0	0	0	Field node
2	0	1	0	0	Field node
3	0	0	1	0	Field node
4	0	0	0	1	Field node
5	0.5	0.5	0	0	Edge midpoint
6	0	0.5	0.5	0	Edge midpoint
7	0	0	0.5	0.5	Edge midpoint
8	0.5	0	0	0.5	Edge midpoint
9	0.25	0.25	0.25	0.25	Intersection of two bi-medians

have the shape function values as node-1 (1, 0, 0, 0), node-2 (0, 1, 0, 0), node-3 (0, 0, 1, 0) and node-4 (0, 0, 0, 1) for a quadrilateral element. At intermediate midpoints 5 and 6, the shape functions are calculated through linear shape functions of two related nodes on the edge and obtained as (0.5, 0.5, 0, 0) and (0, 0, 0.5, 0.5) respectively. In the same manner, we can write the shape functions for the edges of 3-subcells and 4-subcells

shown in **Figure 3.5(c)** and **Figure 3.5(d)** respectively. Detailing of shape function values corresponding to 4-subcells of quadrilateral (SC4Q4) element is given in **Table 3.1**. Though the 4-node quadrilateral elements are used for meshing the problem domain, the element inside the domain may have triangular sub-elements at the split element cut by arbitrary crack (see **Figure 3.4(c)**) and inside the transition element (see **Figure 3.3**). Therefore, a set of nodal shape function values for triangular element may be taken as  $[(1, 0, 0), (0, 1, 0), (0, 0, 1)]$ . **Table 3.2** represents the shape function values of 4-smoothing subcells of triangular element (SC4T3) as shown in **Figure 3.6(b)**. For simplicity, 1-subcell (**Figure 3.6 (a)**) of triangular element is considered for the computational purpose in the current chapter.

Table 3.2: Shape function values at different sites within SC1T3 element (**Figure 3.6(b)**)

SITE	NODE 1	NODE 2	NODE 3	DESCRIPTION
1	1	0	0	Field node
2	0	1	0	Field node
3	0	0	1	Field node
4	0.5	0.5	0	Edge midpoint
5	0	0.5	0.5	Edge midpoint
6	0.5	0	0.5	Edge midpoint

To compute the smoothed strain-displacement gradient matrix, the shape function is required only along the boundary of the subcells. The stiffness matrix is obtained from linear integration along the boundaries of each subcell. The division of the cracked element and intact element along with subcells formation is shown in **Figure 3.4**. A crack separates element into two sub-elements and each sub-element further qualify for the number of subcells for the boundary integration. In case the crack makes a partition such that intact element is divided into 1-triangle and 5-sided polygon, then that element is divided into the number of triangular subcells as shown in **Figure 3.4(c)** and line integration is performed along each boundary of the triangular subcell. Crack touching any standard node of FE element may lead to the development of triangular as well as quadrilateral sub-elements. Smooth stiffness matrix is computed using **Eq. (3.23)** for smooth domain of subcell and global stiffness is calculated with the assemblage of the elemental stiffness. In the same way, smooth strain-displacement matrix and strain are computed corresponding to each subcell by using **Eq. (3.21)** and **Eq. (3.20)** respectively.

For the comparison purpose, conventional Gauss quadrature integration procedure is also applied with FNM, and the obtained results are compared with the SFNM results. Kumar et al. [5] discussed the integration scheme with respect to the aspect ratio for curved crack problems. A crack passing close to one of the standard nodes of the element may lead to a skewed aspect ratio. It shows the division of the element into a triangular

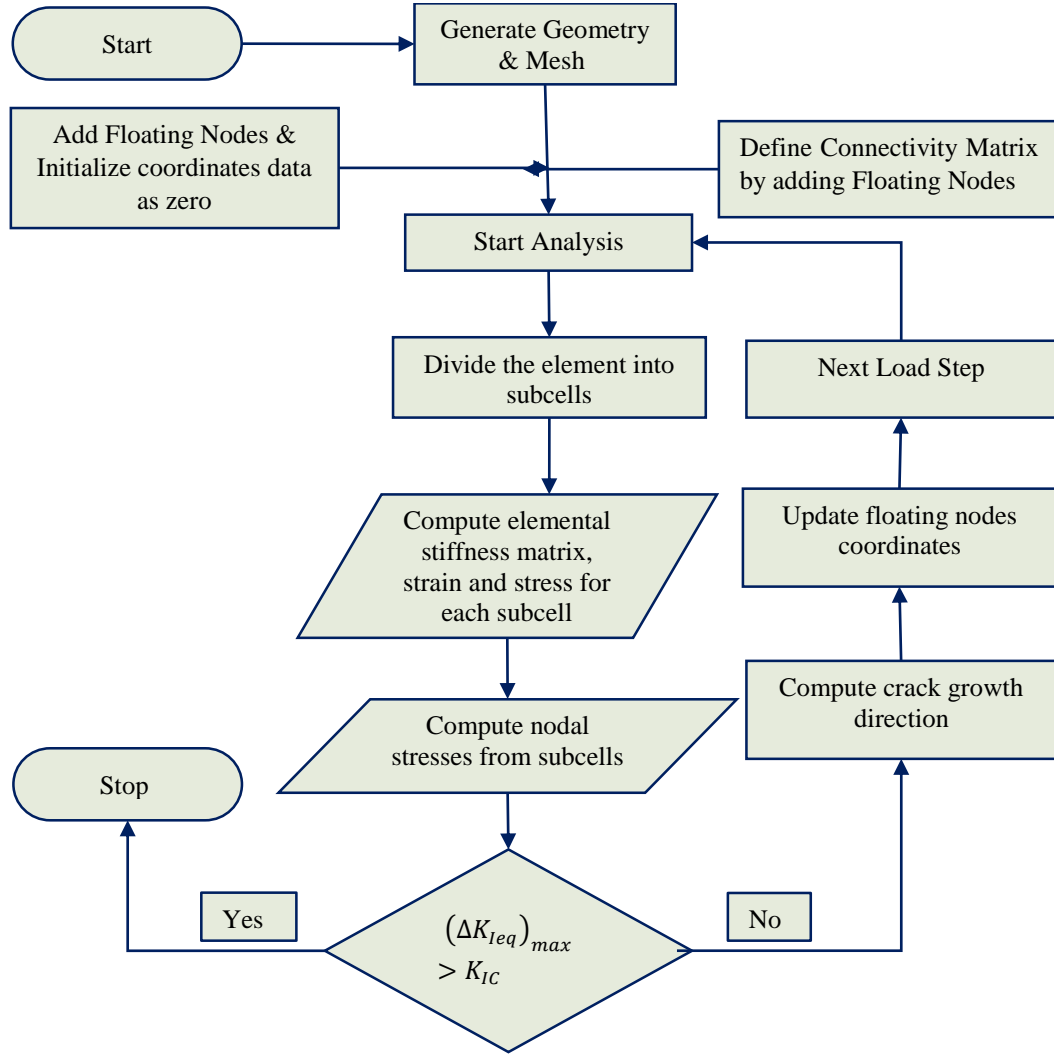


Figure 3.7: Detailed procedure in SFNM for modelling crack initiation to final failure.

and pentagon sub-elements. Integration of triangular sub-element using Gauss quadrature is straightforward but the pentagon sub-element is further divided into 3 triangles in case of the element is restricted to 4 floating nodes. To compensate the poor aspect ratio, instead of 4 floating nodes, 5 floating nodes are used to maintain the appropriate aspect ratio in accordance to Gauss quadrature integration. The 5<sup>th</sup> floating node inside the domain is inserted iteratively. The procedure to insert extra float node and creating the triangular sub-elements is available in [5]. To tackle the poor aspect ratio, inserting extra floating node adds the complexity in the computation. This

drawback may be resolved precisely by using the smoothing integration approach as shown in **Figure 3.5** and **Figure 3.6**.

#### 3.2.5 SFNM outline

FNM formulation is explained in Section 3.2.2. Detailing of the division of an intact element into sub-elements due to discontinuity and the activation and positioning of the floating nodes is also demonstrated in the same section. In the continuation of this, strain-displacement matrix according to the smoothing approach is required. Displacement gradient for the calculation of smoothed domain given in **Eq. (3.23)** can be recalled from the **Eq. (3.21)**. The explicit shape functions as mentioned in **Table 3.1** and normal unit vectors are sufficient to proceed for the line integration approach. The steps required in SFNM to model crack propagation is detailed in flow chart given in **Figure 3.7**.

### 3.3 SIF Computation

The stress intensity factor is a critical parameter that has frequently been used in fracture mechanics problems of brittle materials. The virtual crack closure technique (VCCT) and interaction integral approach are the commonly used approach in literature for calculating the SIF values. However, the VCCT approach is cumbersome to implement in generic crack propagation problems as it generally requires uniform mesh. Therefore, a domain based interaction integral approach is used in conjunction with SFNM to compute the values of SIF. For two independent equilibrium states of a cracked body, the domain form of interaction integral can be written as,

$$I^{(1,2)} = \int_A \left[ \sigma_{ij}^{(1)} \frac{\partial u_i^{(2)}}{\partial x_1} + \sigma_{ij}^{(2)} \frac{\partial u_i^{(1)}}{\partial x_1} - \mathbf{W}^{(1,2)} \delta_{1j} \right] \frac{\partial q}{\partial x_j} dA \quad (3.26)$$

where  $\mathbf{W}^{(1,2)}$  is the interaction strain energy term associated with actual and auxiliary states,  $q$  is a smoothing weight function,  $\sigma_{ij}$  is the stress field, 1 and 2 signify the actual and auxiliary state respectively. For the bi-material interface cracked body, the interaction integral form can be written as,

$$I^{(1,2)} = \sum_{m=1}^2 \int_{A_m} \left[ \sigma_{ij}^{(1)} \frac{\partial u_i^{(2)}}{\partial x_1} + \sigma_{ij}^{(2)} \frac{\partial u_i^{(1)}}{\partial x_1} - \mathbf{W}^{(1,2)} \delta_{1j} \right] \frac{\partial q}{\partial x_j} dA \quad (3.27)$$

where  $m$  represents a particular material in the bi-material domain. In LEFM, the relationship between interaction integral and SIF is given as,

$$I^{(1,2)} = \frac{2(K_I^{(1)}K_I^{(2)} + K_{II}^{(1)}K_{II}^{(2)})}{E^* \cosh^2(\pi\epsilon)} \quad (3.28)$$

where

$$\frac{2}{E^*} = \frac{1}{E_1} + \frac{1}{E_2}$$

For bi-material interfacial cracks, the auxiliary fields [137] can be written as,

$$u_i = \begin{cases} \frac{1}{4\mu_1 \cosh(\pi\epsilon)} \sqrt{\frac{r}{2\pi}} f_i(r, \theta, \epsilon, \kappa_1) & \text{for upper half plane} \\ \frac{1}{4\mu_2 \cosh(\pi\epsilon)} \sqrt{\frac{r}{2\pi}} f_i(r, \theta, \epsilon, \kappa_2) & \text{for lower half plane} \end{cases} \quad (3.29)$$

where  $\mu$  is the shear modulus,  $(r, \theta)$  are the polar coordinates. The details of computing the functions  $f_1$  and  $f_2$  can be found in literature [138]. The parameters  $\epsilon$  and  $\kappa$  are bi-material constants and defined as,

$$\epsilon = \frac{1}{2\pi} \log \left( \frac{1 - \bar{\beta}}{1 + \bar{\beta}} \right)$$

where,  $\bar{\beta}$  is the second Dundurs parameter and defined as,

$$\bar{\beta} = \frac{\mu_1(\kappa_2 - 1) - \mu_2(\kappa_1 - 1)}{\mu_1(\kappa_2 + 1) + \mu_2(\kappa_1 - 1)}$$

and

$$\kappa_i = \begin{cases} 3 - 4\nu_i & \text{plane strain} \\ \frac{3 - \nu_i}{1 + \nu_i} & \text{plane stress} \end{cases}$$

where  $\nu$  is Poisson's ratio.

The mixed mode SIF values can be obtained from **Eq. (3.28)** using  $K_I^{(2)}=1$  and  $K_{II}^{(2)}=0$  and vice versa.

$$K_I = \frac{E^* \cosh^2(\pi\epsilon)}{2} I^{(1)} \quad (3.30a)$$

$$K_{II} = \frac{E^* \cosh^2(\pi\epsilon)}{2} I^{(2)} \quad (3.30b)$$

### 3.4 Crack Propagation Criterion

To determine the crack growth direction, a particular requisite criterion needs to be prescribed. Due to the cyclic loading, crack may reach to the critical length which causes severe fracture failure of the structural components. To avoid the fracture failure, crack growth rate and propagation direction are predicted. The discrete set of equations are solved to obtain the displacements, and the stress intensity factor values are extracted from **Eq. (3.30)**. The range of SIF for both mode-I and mode-II under constant amplitude cyclic loading is defined as,

$$\Delta K = K_{\max} - K_{\min} \quad (3.31)$$

where  $K_{\max}$  and  $K_{\min}$  are the SIF values corresponding to maximum and minimum applied loads respectively. In this study, the maximum circumferential stress criterion is employed to obtain the direction of crack growth. The equivalent SIF and the direction of crack growth  $\theta_c$ , at each crack increment are obtained using the following expressions,

$$\Delta K_{Ieq} = \Delta K_I \cos^3\left(\frac{\theta_c}{2}\right) - 3\Delta K_{II} \cos^2\left(\frac{\theta_c}{2}\right) \sin\left(\frac{\theta_c}{2}\right) \quad (3.32)$$

$$\theta_c = 2 \arctan \frac{1}{4} \left\{ \frac{K_I}{K_{II}} \pm \text{sign}(K_{II}) \sqrt{\left(\frac{K_I}{K_{II}}\right)^2 + 8} \right\} \quad (3.33)$$

Failure takes place whenever  $(\Delta K_{Ieq})_{\max} > K_{IC}$ , where  $(\Delta K_{Ieq})_{\max}$  is the equivalent stress intensity factor corresponding to maximum load and  $K_{IC}$  is the fracture toughness of the material.

### 3.5 Numerical Examples

In this section to illustrate the accuracy and effectiveness of the proposed SFNM, both static and crack propagation examples are considered for simulations and the results obtained by SFNM are compared with the FNM and available literature results. All the simulations are performed under plane strain condition. In all the problems, uniform



initial mesh of quadrilateral elements is used in the entire domain. The LEFM theory is considered in the simulations, where the crack tip is singular at the crack tip. Thus, special crack tip elements are required to model the crack tip singularity. However, in the present work, special transition element within the SFNM framework is used just ahead of the crack tip (see **Figure 3.3(e)**), which improves the accuracy of the results. Moreover, the values of SIF are obtained using domain based interaction integral approach, which considers the global quantities far from the crack tip for SIF computation and reduces the effect of singularity on the numerical results.

### 3.5.1 Static crack examples

In this section, the accuracy and convergence properties of the proposed SFNM are numerically studied within the LEFM framework in 2D static crack problems under mode-I and mode-II loading conditions. The numerical results from the proposed SFNM formulation are compared with the FNM and literature results. The strain energy and error in SIF are used to estimate the error and convergence properties of the proposed SFNM.

#### 3.5.1.1 Plate with an edge crack under mode-I loading

In this example, a rectangular plate with an edge crack is analysed under tension loading ( $\sigma = 10$  MPa). The basic geometry along with the dimensions ( $a = 4$  mm,  $H = 16$  mm,  $W = 8$  mm) and boundary conditions are shown in **Figure 3.8**. The thickness of the plate is taken as 1 mm. The material properties are taken from Ref. [116]. They are given as: Young's modulus  $E = 1$  MPa; Poisson's ratio  $\nu = 0.3$ . The strain energy and the error in the SIF are given as,

$$E_{(\Omega)} = \frac{1}{2} \int_{\Omega} \boldsymbol{\epsilon}^T \mathbf{D} \boldsymbol{\epsilon} d\Omega \quad (3.34)$$

$$e_k = \left| \frac{K_{SIF}^{num} - K_{SIF}^{ref}}{K_{SIF}^{ref}} \right|^{1/2} \times 100\%, \quad \text{SIF} = I, II \quad (3.35)$$

where the superscript “ref” denotes the reference solution and “num” denotes the numerical solution.

For the simulation purpose, the domain is discretized by a structured mesh with 4-node quadrilateral (Q4) elements for both FNM and SFNM. Different mesh sizes i.e. 242 nodes (11×22), 882 nodes (21×42), 1922 nodes (31×62), 3362 nodes (41×82), 5202

nodes (51×102) and 7442 nodes (61×122) are considered for checking convergence properties of the proposed approach. The strain energy and relative error in SIF values

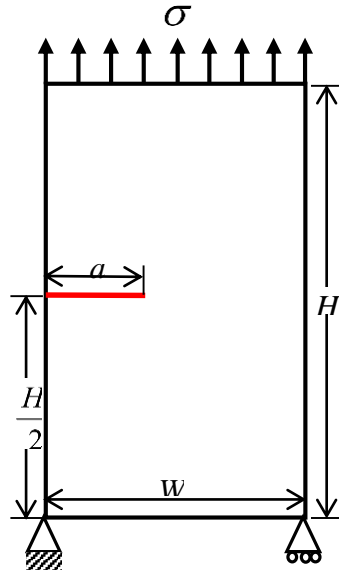


Figure 3.8 A rectangular plate with an edge crack under mode-I loading

are computed and plotted with respect to mesh size, then SFNM results are compared with the FNM and literature results. **Figure 3.9** shows the comparison of strain energy values obtained through SFNM and FNM with the literature in mode-I loading. From the figure, it is apparent that the convergence of SFNM is slightly better than FNM.

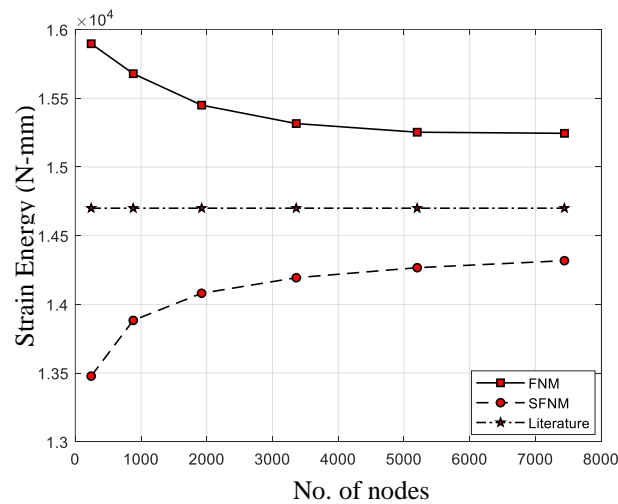


Figure 3.9 The convergence in strain energy for the rectangular plate with edge crack under mode-I loading.

Further, the relative error in SIF values is plotted with the mesh size in log scale for SFNM and FNM as shown in **Figure 3.10**. From the comparison, it is evident that SFNM technique is more accurate and gives better convergence rate than the FNM. The

SIF relative error using SFNM is significantly less in comparison to SIF relative error using FNM as shown in **Figure 3.10**. The stress contours are also plotted for illustration purpose in **Figure 3.11**.

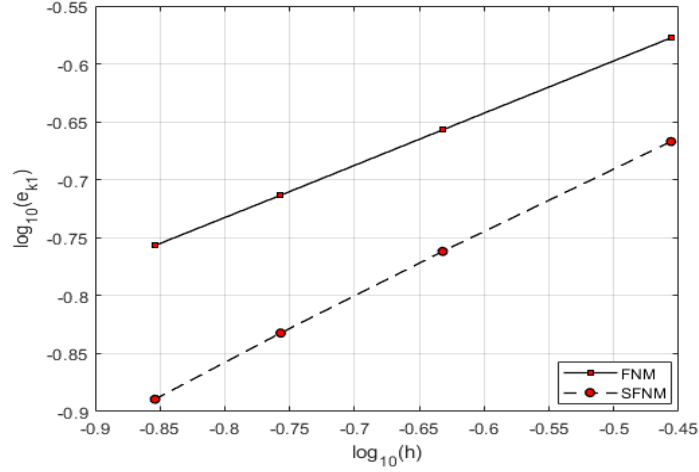


Figure 3.10 Comparison of convergence rate between FNM and SFNM in the SIF

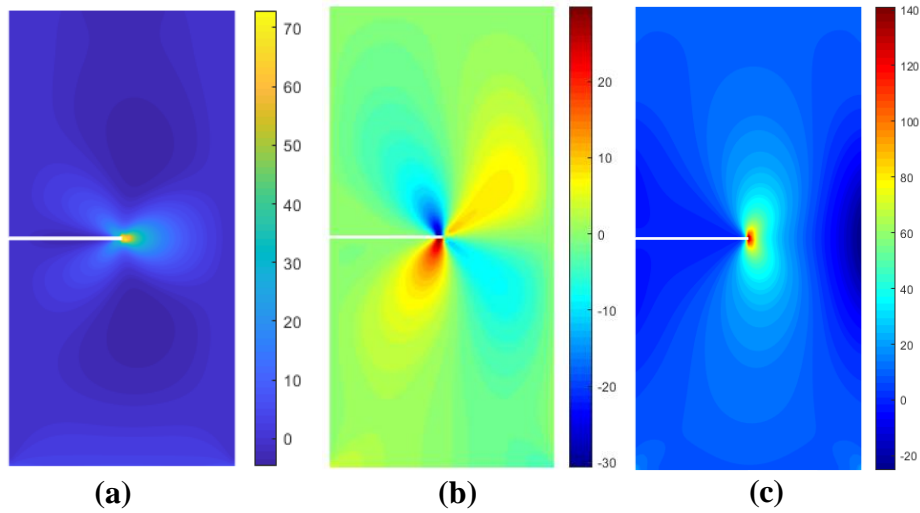


Figure 3.11 Static edge crack plate stress contours under mode-I loading: (a)  $\sigma_{xx}$  (b)  $\sigma_{xy}$  (c)  $\sigma_{yy}$ .

### 3.5.1.2 Plate with an edge crack under shear

Next, to illustrate the ability of the SFNM, we consider a rectangular plate with an edge crack subjected to pure shear traction on the top surface as shown in Figure 3.12. The bottom of the plate is fixed and plane strain condition is assumed for simulation. The geometry parameters used in the computation are: width  $W = 7$  mm, height  $H = 16$  mm, crack length  $a = 3.5$  mm. The material properties; Young's modulus  $E$  and Poisson's ratio  $\nu$  are taken as  $3 \times 10^7$  Pa and 0.25 respectively. The reference values of SIFs for

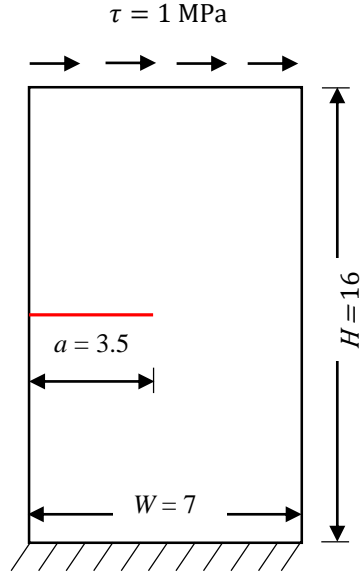


Figure 3.12 : A rectangular plate with an edge crack under shear (mode-II) loading, dimensions are in mm.

this case are taken from the literature [139] and given as  $K_I = 34 Pa\sqrt{mm}$ ,  $K_{II} = 4.55 Pa\sqrt{mm}$ . Different mesh sizes i.e. 882 nodes (21×42), 1922 nodes (31×62), 3362 nodes (41×82), 5202 nodes (51×102), 7442 nodes (61×122) and 10082 nodes

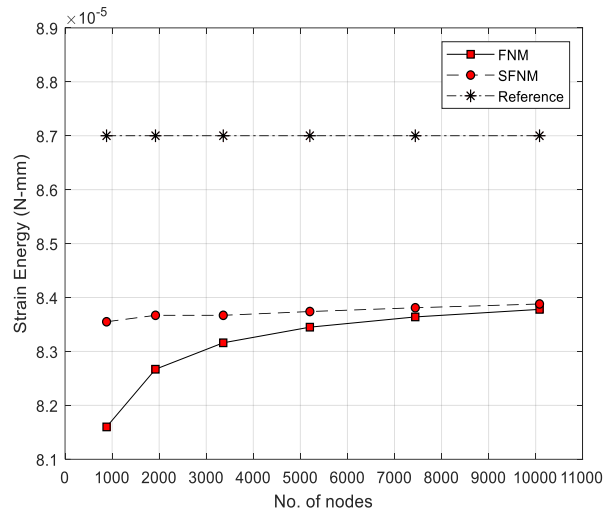


Figure 3.13: The convergence in strain energy for the rectangular plate with edge crack under mode-II loading.

(71×142) are considered to analyse the convergence properties of the proposed framework. The strain energy convergence with respect to mesh refinement is shown in **Figure 3.13**, which depicts that the strain energy convergence is better in SFNM than in FNM. In addition, the mesh convergences of stress intensity factors  $K_I$  and  $K_{II}$  are

presented in **Figure 3.14 (a)** and **Figure 3.14 (b)** respectively. In both cases, it is evident that a significant reduction of error is achieved in SFNM as compared to FNM.

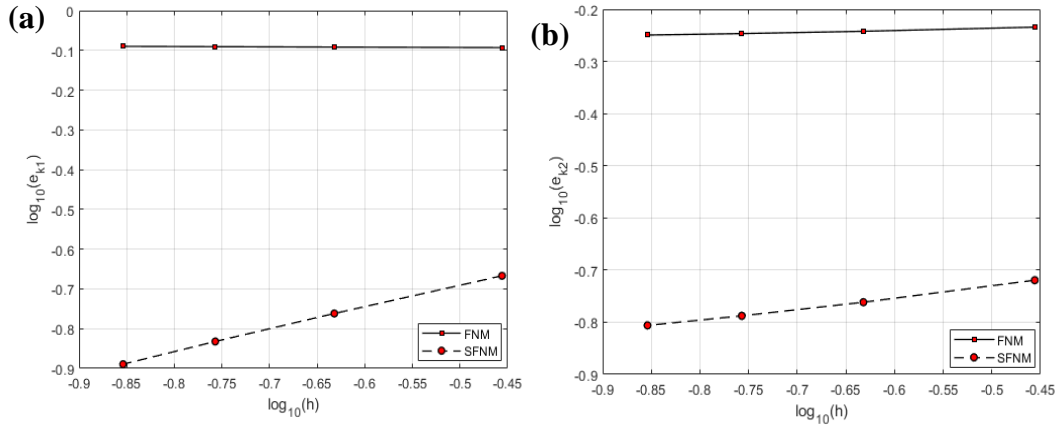


Figure 3.14: Comparison of convergence rate of SIF vs mesh size ( $h$ ) between FNM and SFNM; (a) convergence in SIF  $K_I$  (b) convergence in SIF  $K_{II}$ .

### 3.5.2 Crack propagation examples

After verifying the accuracy and convergence properties of SFNM for static crack problems under mode-I and mode-II loading conditions, here we extend it for simulating the crack propagation problems. Three 2D problems are considered in this section for verifying the accuracy of the proposed SFNM. In the first problem, an edge crack plate is simulated under mode-I cyclic loading. In the second problem, an edge crack plate is considered under mode-II cyclic loading. Finally, a plate with a bi-material interfacial edge crack is simulated under mode-I cyclic loading.

#### 3.5.2.1 Plate with an edge crack under tensile loading

In this section, we revisit the problem of an edge crack as mentioned in Section 5.1.1 under cyclic loading condition. The initial crack length is considered as  $\frac{a}{W} = 0.2$ . The crack is considered to propagate under mode-I condition and analysed in the range of  $\frac{a}{W} = 0.2$  to  $\frac{a}{W} = 0.6$ . The plate is subjected to a tensile load of intensity  $\sigma = 10$  MPa at the top edge of the plate as shown in **Figure 3.8**. The material properties and other geometric conditions are given in Section 3.5.1.1. It is well known that the numerical results are strongly mesh size dependent, hence a converged uniform initial mesh of 7442 nodes (61 and 122 nodes in  $x$ - and  $y$ - directions respectively), is adopted for the simulation, refer Section 3.5.1.1 for more detail. To compare the SFNM results, the stress intensity values are also calculated theoretically. Further, the SIF values obtained

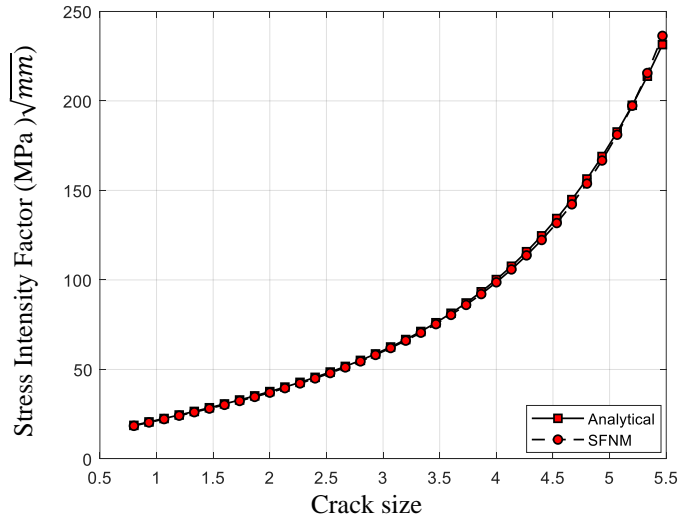


Figure 3.15: SIF variation with crack length under mode-I loading for edge crack plate.

by SFNM are compared with the analytical (theoretical) solutions. They are found to be in good agreement as shown in **Figure 3.15**. Finally, the normal stress contour plots obtained by smoothed FNM are shown in **Figure 3.16** for different crack lengths. From the results, it is observed that the SFNM captures the crack propagation behaviour effectively without the requirement of remeshing and additional enrichment terms.

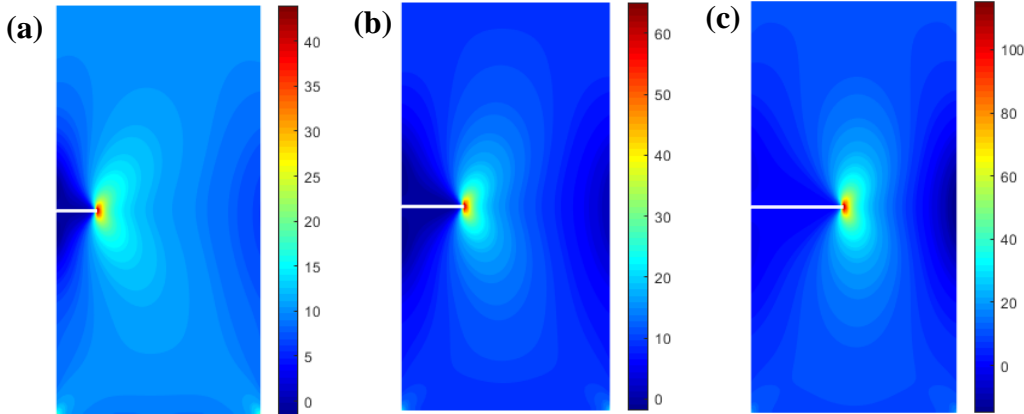


Figure 3.16: Normal stress contour of edge crack plate under normal load; (a)  $a/W=0.2$ , (b)  $a/W=0.3$  and (c)  $a/W=0.45$ .

### 3.5.2.2 Plate with an edge crack under shear loading

A rectangular plate with an edge crack under pure shear, shown in **Figure 3.12**, is considered for the simulation. The geometry parameters used in the computation are: width  $W = 7$  mm, height  $H = 16$  mm, initial crack length is taken as  $\frac{a}{W} = 0.2$  where  $a$  is the crack length. The material properties Young's modulus  $E$  and Poisson's ratio  $\nu$  are

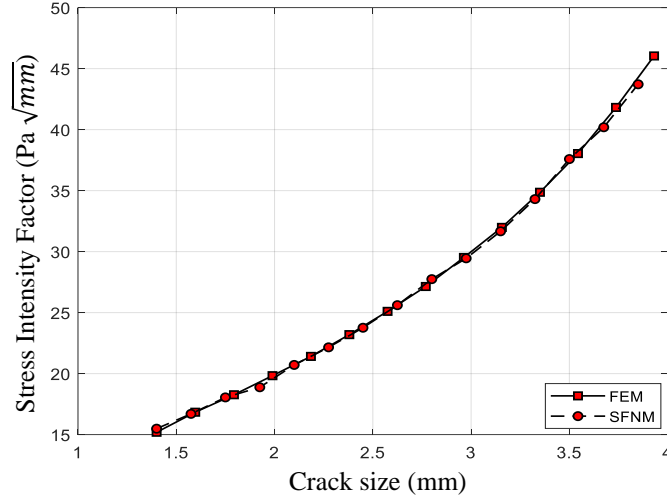


Figure 3.17: SIF variation with crack length under mode-II loading for edge crack plate

taken as  $3 \times 10^7$  Pa and 0.25 respectively. The specimen is subjected to shear load  $\tau = 1$  MPa at the top edge of the plate. A converged initial mesh with 7442 nodes (61 and 122 nodes in  $x$ - and  $y$ - directions respectively), is considered for the simulation as discussed in section 5.1.2. For the simulations, crack propagation range is taken as  $\frac{a}{W} = 0.2$  to  $\frac{a}{W} = 0.6$ . The SIF values obtained by SFNM using interaction integral approach

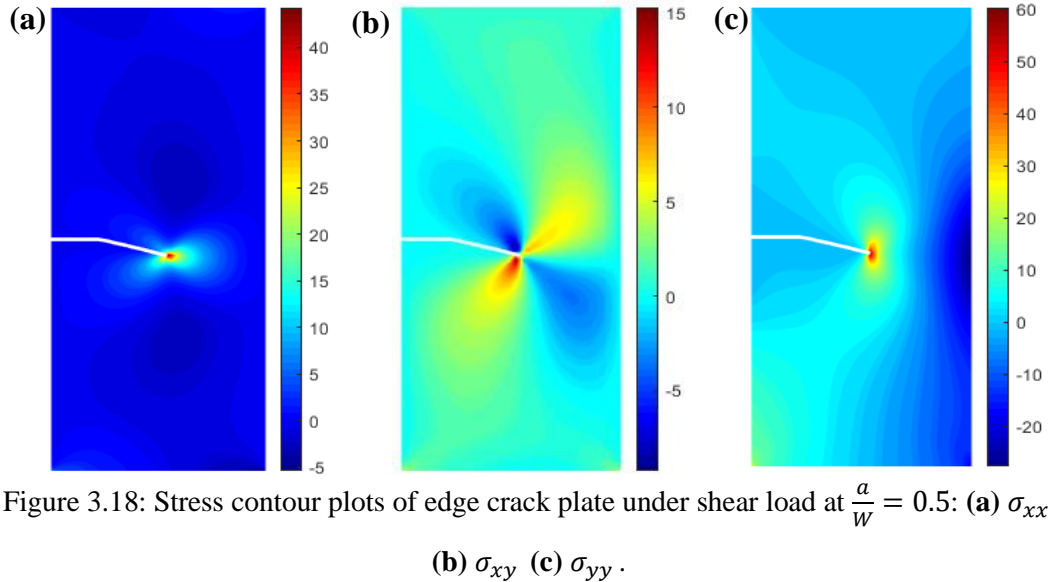


Figure 3.18: Stress contour plots of edge crack plate under shear load at  $\frac{a}{W} = 0.5$ : (a)  $\sigma_{xx}$  (b)  $\sigma_{xy}$  (c)  $\sigma_{yy}$ .

are plotted against crack length and compared with FEM results, shown in **Figure 3.17**. Further, the stress contour plots obtained through SFNM are also shown in **Figure 3.18** under pure shear loading. Due to pure shear all three stress components variation is plotted at a crack to width ratio of 0.5. From these results, it is observed that the SFNM

captures the crack propagation behaviour effectively even for the curved crack growth problems. Finally, the crack trajectory obtained through SFNM and FEM are compared in **Figure 3.19** and found in good agreement.

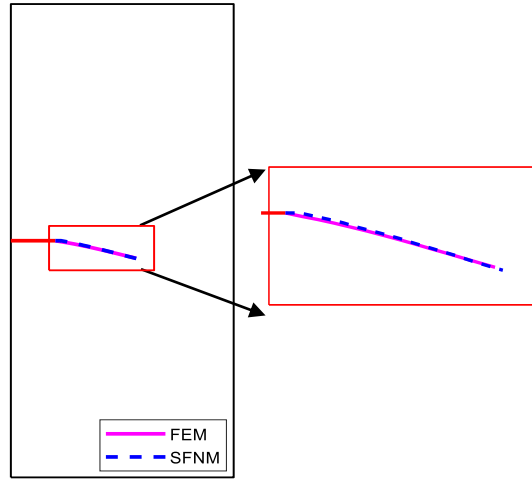


Figure 3.19: Crack growth trajectory comparison of an edge crack plate under mode-II loading.

### 3.5.2.3 Bi-materials edge crack under normal load

A bi-material plate of size 50 mm  $\times$  100 mm with an interfacial edge crack of initial length  $a = 10$  mm ( $\frac{a}{W} = 0.2$ ) is taken for the simulation as shown in **Figure 3.20(a)**. The thickness of the plate is assumed to be 1 mm. A tensile load of intensity  $\sigma = 50$  MPa is applied at the top edge of the plate, while the bottom edge of the plate is constrained. An initial uniform mesh of 7442 nodes (61 and 122 nodes in  $x$ - and  $y$ - directions respectively), is taken for simulations. There is a difference in the elastic properties of the two materials on either side of the interface and symmetry is disrupted even though the geometry of the body is symmetric. The material properties of both the base materials are taken from literature [5] and given in **Table 3.3**.

Table 3.3: Properties of the constituents of bi-materials rectangular plate.

	Young's Modulus, E (GPa)	Poisson's ratio, $\nu$	Fracture toughness, $K_{IC}$ (MPa.m <sup>0.5</sup> )
<b>Material-1</b>	74	0.30	40
<b>Material-2</b>	200	0.30	60

The fracture toughness of the interface is considered higher than both the base materials for simulation purpose, hence the crack may propagate into either of the material



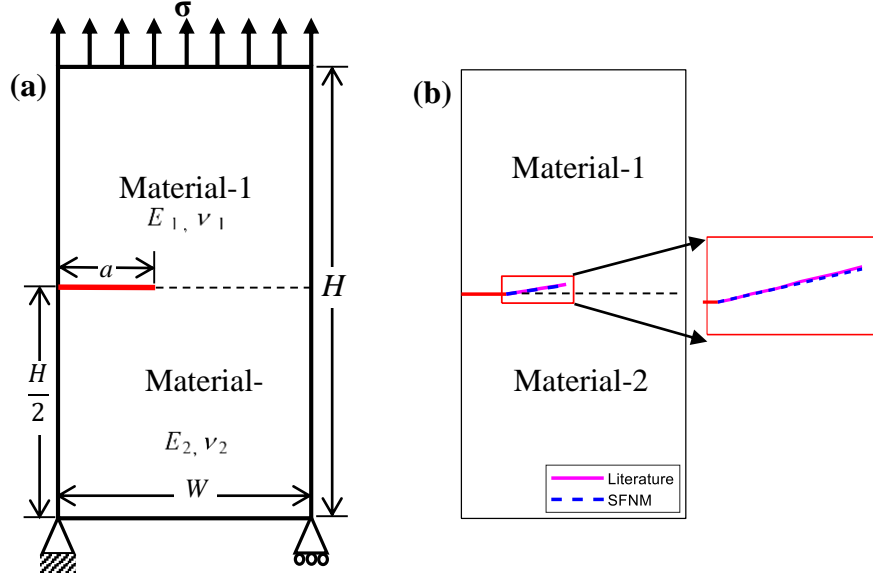


Figure 3.20: (a) Bi-material plate with an interfacial edge crack under mode-I loading; (b) Crack growth trajectory comparison of a bi-material interface edge crack.

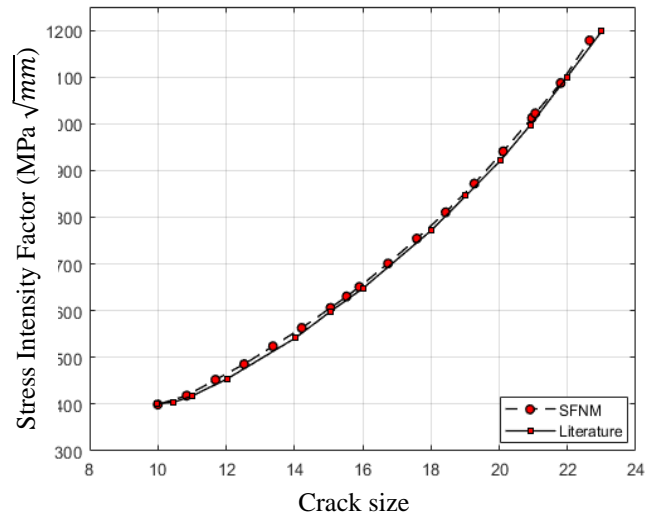


Figure 3.21: SIF vs crack length plot for bi-materials edge crack plate under mode-I.

depending on their material properties. The computed equivalent SIF ( $\Delta K_{Ieq}$ ) is compared with the local fracture toughness of both materials to determine the crack trajectory. For this purpose, two ratio  $R_1$  and  $R_2$  are calculated as [140],

$$R_1 = \frac{(\Delta K_{Ieq})_{m1}}{(K_{IC})_{m1}} \quad \text{and} \quad R_2 = \frac{(\Delta K_{Ieq})_{m2}}{(K_{IC})_{m2}}$$

where  $m_1$  and  $m_2$  represent the material-1 and material-2 respectively. If the  $R_1 > R_2$ , the crack will propagate into the first material along the predicted angle  $\theta = \theta_c$ . Otherwise, it will propagate into the second material. The obtained crack path through SFNM is compared with the literature in Figure 3.20(b). Further, the obtained SIF

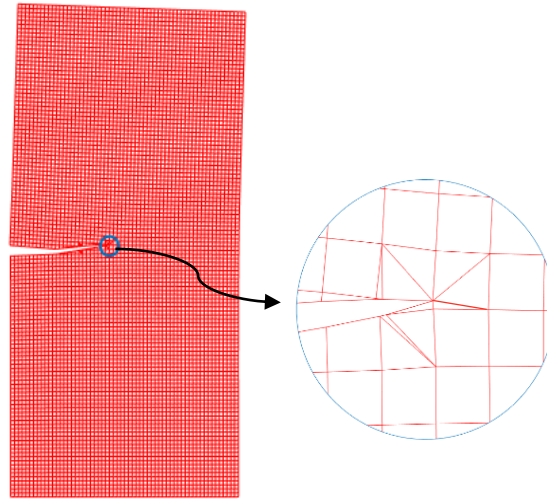


Figure 3.22: Deformed configuration with element subdomains for bi-material edge crack plate under mode-I loading

values using SFNM are compared with the literature results and a good agreement is obtained as shown in **Figure 3.21**. The angle of crack propagation is computed using the maximum circumferential stress theory as discussed in Section 3.4. The advancement of crack divides the element into several sub-elements. The final deformed configuration at enlarged scale along with sub-elements is depicted in **Figure 3.22**. A

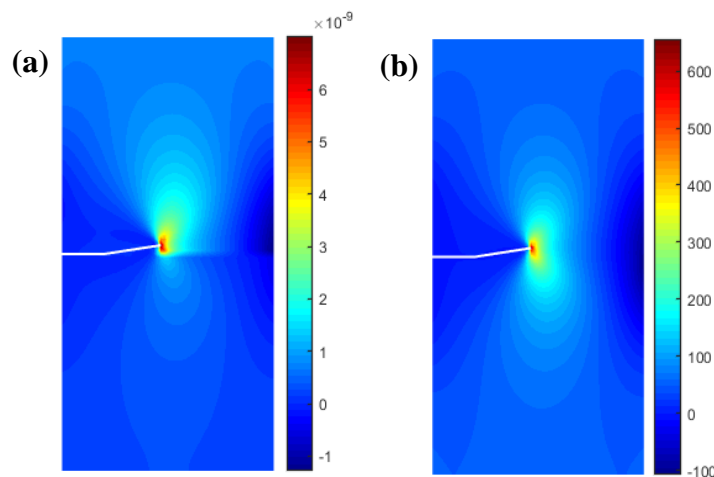


Figure 3.23: Stress and Strain contour plot at failure condition; **(a)** strain contour plot in y-direction **(b)** stress contour plot in y-direction.

small portion of the growth path is magnified and shown in the same figure to illustrate the split and transition elements. From the zoomed view, it can be observed that some

of the sub-elements in the split element and transition element maintain poor aspect ratio, lead to error during integration and may deteriorate the convergence rate in FNM. However, in the smoothed FNM such kind of issue does not occur as the domain integral is converted into line integral using the smoothing procedure. The SFNM could be more effective for large deformation problems, where an element distortion is a major problem which reduce the accuracy and convergence rate. The normal stress and normal strain contours at final crack length are shown in **Figure 3.23**.

### 3.6 Conclusions

In this chapter, a smoothed floating node numerical framework for the 2D linear elastic problem is developed by combining FNM with the smoothed FEM. The cell-based smoothing procedure is adopted for the sub-element integration. The proposed framework is easy to implement and can be applied to triangular or quadrilateral or any distorted elements. Field gradients are computed directly using shape functions at midpoints of the boundary segments of the smoothing cells. The combination of SFNM with interaction integral approach offers accurate and path independent evaluation of SIFs. The issue of (sub-)element distortion can be avoided as it does not require the inverse of Jacobian during integration. Moreover, SFNM's convergence rate is better than FNM, hence computationally more efficient. From the simulations, it is observed that the SFNM combines the advantages of SFEM and FNM, making it an attractive method for solving fracture mechanics problems.

This chapter investigates the convergence and accuracy of FNM and SFNM when dealing with 2D arbitrary crack. This comparison is particularly significant when the fracture process zone is disregarded in comparison to the crack. However, for quasi-brittle materials, where managing singularity and the nonlinear fracture process zone becomes a challenge, special treatment of this zone is imperative. To tackle this challenge, we introduce cohesive law capable of addressing both the singularity at the crack tip and the nonlinear characteristics of micro-crack accumulation ahead of the crack tip. The subsequent chapter features the implementation of the cohesive zone modelling framework, utilizing the developed SFNM methodology.

Page left blank intentionally

### SFNM Implementation with CZM for Quasi-Brittle Materials

---

This chapter presents a numerical framework for implementation of cohesive zone model with smoothed floating node method for failure analysis of quasi-brittle materials. The nonlinear behaviour of material inside the fracture process zone in front of the crack tip is modelled with a potential-based intrinsic cohesive zone approach. A strain smoothing technique is adopted over the domain through which classical domain integration changes to line integration along each boundary of the smoothing cell, hence derivative of shape functions are not required in the computation of the field gradients, thus resolves the issue of element distortion. The proposed numerical framework is firstly verified using the patch test of the 2D specimen under mode I and mode II loading conditions and subsequently extended for solving the 2D standard fracture problems. The effectiveness of the proposed framework is checked by comparing the computational results with the available literature results.

#### 4.1 Introduction

In quasi-brittle materials, the nonlinear nature of fracture process zone (FPZ) in front of an open crack induces an analytical challenge. The region ahead of the crack tip has micro-cracks or voids but still cohesive stress can be transferred across the discontinuity. Negligence of this small nonlinear behaviour region can lead to errors in crack propagation calculations and inaccurate predictions of life of the structures. Many researchers have studied the crack propagation mechanism in different types of problems. The basis for all the theories developed is Griffith's innovative work in this field, which discusses the energy-based crack propagation criterion [141]. This criterion was further improved by taking the stress intensity factor for crack propagation, but suffers with the issue of stress singularity at the crack tip. Later, cohesive zone model (CZM) formulation was developed by Brenblatt which introduced the criterion to eliminate the singularity at the crack tip by fixing the computed stresses to a finite value [142]. Dugdale, further, modified the maximum value of the stress at the crack tip as equivalent to the strength of the material [8]. In the same context, Hillerborg [10] has

proposed the so-called ‘fictitious crack model’ for the analysis of crack propagation in concrete structures.

The FEM-based numerical methods for determining the fracture behaviour of the materials are typically classified into two groups: smeared crack approach and the discrete crack approach. The discrete crack approaches are an efficient tool for the numerical approximation of fracture analysis and have been widely employed to study the macroscopic fracture behaviour of the quasi-brittle materials [86,143]. In this context, the cohesive zone modelling has been reported as a powerful concept to tackle the nonlinearity in the FPZ that depicts the traction separation law (TSL). Particularly, FPZ is a partially damaged zone with stress transferring capability, where the stresses applied on the crack surfaces decrease with the increase in the crack opening. The interface stresses resist the opening of the crack and prevents crack propagation until the crack interface displacement reaches the decohesive displacement. TSL is independent of the externally applied stress and can be calibrated from the experimental characterization or the micromechanics analysis. The TSLs are implemented with the help of zero-thickness interface elements inserted in the bulk elements. Different traction separation laws have been proposed in the literature with variations in maximum traction, maximum separation, and shapes. These laws mainly include the linear softening cohesive law [144], the exponential cohesive law [145], Xu and Needleman law [146], the trapezoidal cohesive law [147], and the polynomial cohesive law [148]. These cohesive laws correlate failure load, fracture energy, and crack growth of the cracked structures.

As outlined in the previous chapter, the SFNM technique amalgamates the advantages of FNM and strain smoothing, effectively mitigating challenges like remeshing during crack propagation, and the problem of significant element distortion during integration. Therefore, in this chapter, smoothed floating node method framework is applied with intrinsic CZM for modelling the nonlinear fracture process zone in quasi-brittle materials. Generally, special treatment functions or higher order shape functions induced to the blending elements of the crack discontinuity may lead to the ill conditioned systems [149,150]. The proposed framework removes the shortcomings of the blending elements without using any enrichment functions. It also avoids the isoparametric mapping and simplifies the numerical integration scheme by suppressing the integration of singular terms. Moreover, the implement of CZM into

SFNM is straight forwarded and easy to implement. To demonstrate the effectiveness of the proposed approach, first two patch test under mode I and mode II loading conditions are solved and results are validated with the available literature data. Further, three benchmark fracture mechanics problems, taken from the literature, are examined under mode I and mixed mode loading conditions. In the first problem, a three-point bending test with an edge cracked plate under mode I loading is considered and the force-displacement curves are compared. The second problem deals with an eccentric edge cracked plate under mixed mode loading conditions. In the third problem, an L-shaped panel is also analysed under mixed mode loading conditions.

This chapter is organized as follows: Section 4.2 describes the governing equations and mathematical formulation of SFNM and smoothing technique. Section 4.3 illustrates the CZM formulation and its implementation in to SFNM. Sections 4.4 contains the SIF computation and crack growth criterion. The numerical problems are presented in Section 4.5 to demonstrate the effectiveness of the SFNM framework. Finally, the conclusions are drawn in Section 4.6.

## 4.2 Numerical Formulation

In this section, the governing equations for the static analysis of an elastic medium containing a traction-free crack are briefly discussed. A brief review of FNM and SFEM is also presented for completeness. Further, the shape function generation, numerical integration procedure in SFNM, and its implementation procedure are discussed.

### 4.2.1 Governing equations for elasto-statics

Consider a linear elastic body with a discontinuity as shown in **Figure 4.1**. The domain  $\Omega$  is divided into three parts;  $\Gamma_t$  where the traction boundary conditions are applied,  $\Gamma_u$  where the displacement boundary conditions are applied and  $\Gamma_{cr}$  which is the traction-free surface representing the discontinuity. The strong form of the static equilibrium equation along with the boundary conditions are given as,

$$\nabla \cdot \boldsymbol{\sigma} + \mathbf{b} = \mathbf{0} \text{ in } \Omega \quad (4.1)$$

$$\boldsymbol{\sigma} \cdot \hat{\mathbf{n}} = \bar{\mathbf{t}} \text{ on } \Gamma_t \quad (4.2a)$$

$$\boldsymbol{\sigma} \cdot \hat{\mathbf{n}} = \mathbf{0} \text{ on } \Gamma_{cr} \quad (4.2b)$$

$$\mathbf{u} = \bar{\mathbf{u}} \quad \text{on } \Gamma_u \quad (4.2c)$$

where  $\nabla$  is the gradient operator,  $\boldsymbol{\sigma}$  is the Cauchy stress tensor,  $\mathbf{b}$  is the body force vector per unit volume,  $\bar{\mathbf{t}}$  is the applied traction vector and  $\hat{\mathbf{n}}$  is the unit outward normal. For small strains and displacements, the strain-displacement relation can be written as,

$$\boldsymbol{\varepsilon} = \nabla^s \mathbf{u} \quad (4.3)$$

where  $\nabla^s$  is the symmetric part of the gradient operator. The constitutive relation for linear elastic material is given by Hooke's law,

$$\boldsymbol{\sigma} = \mathbf{D}\boldsymbol{\varepsilon} \quad (4.4)$$

where  $\mathbf{D}$  is the material elasticity tensor.

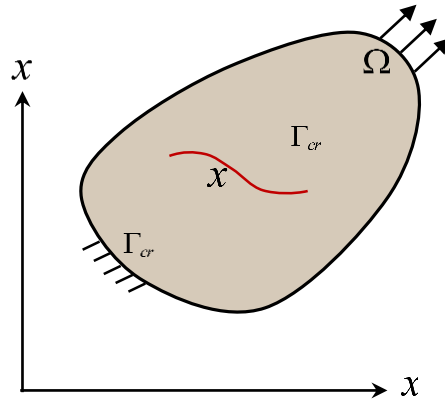


Figure 4.1: A cracked domain with boundary conditions

After substituting the constitutive relation and the strain-displacement relation, the weak form of the equilibrium equation can be expressed as,

$$\int_{\Omega} \boldsymbol{\sigma}(\mathbf{u}) : \boldsymbol{\varepsilon}(\mathbf{v}) \, d\Omega = \int_{\Omega} \mathbf{b} \cdot \mathbf{v} \, d\Omega + \int_{\Gamma_t} \bar{\mathbf{t}} \cdot \mathbf{v} \, d\Gamma \quad (4.5)$$

where  $\mathbf{u}$  and  $\mathbf{v}$  are the displacement trial and the test functions, respectively. Upon discretization of  $\mathbf{u}$  and  $\mathbf{v}$ , the above weak form can be transformed into the following discrete set of equations,

$$\mathbf{Kd} = \mathbf{f} \quad (4.6)$$



where  $\mathbf{K}$  is the global stiffness matrix,  $\mathbf{d}$  is the nodal displacements vector and  $\mathbf{f}$  is the externally applied force vector.

#### 4.2.2 Basic formulation of FNM

Initially, each element in the domain contains suitable number of floating nodes and their corresponding degrees of freedom (dofs). These floating nodes are dormant in the intact element, thus intact element is identical to the standard finite element. As the discontinuity appears inside the element, the floating nodes get activated to model the

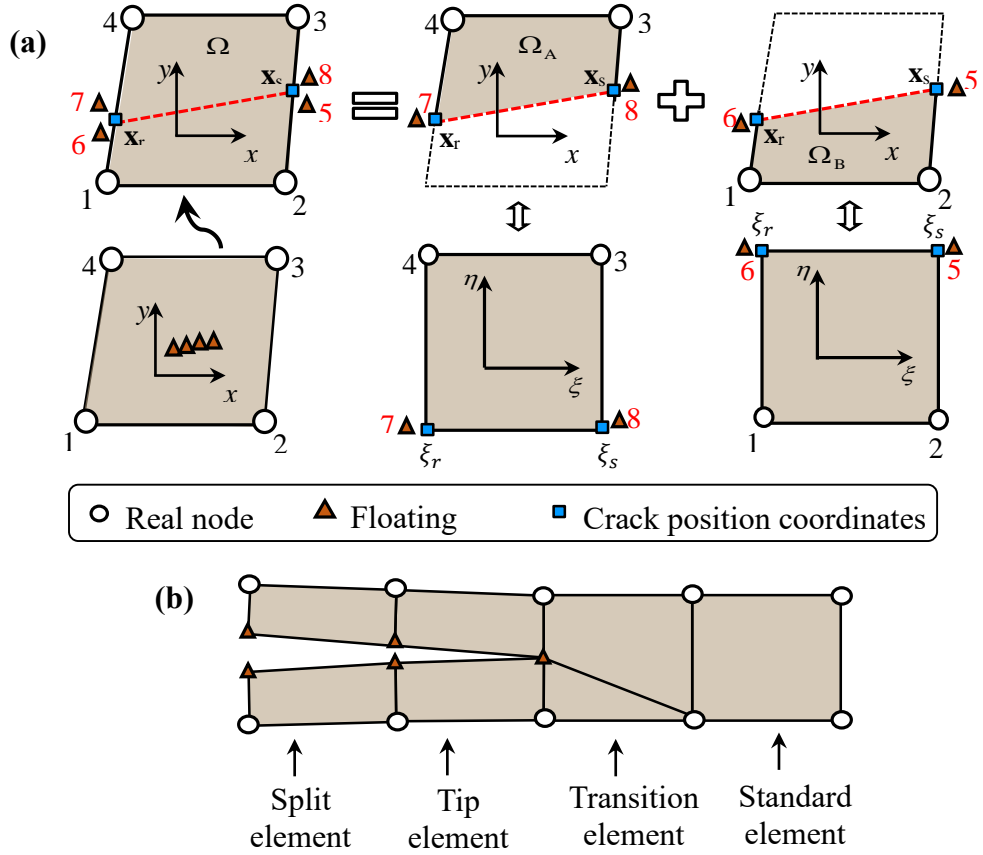


Figure 4.2: (a) Schematic representation of strong discontinuity modelling in an element using FNM, (b) Schematic representation of crack tip modelling in FNM

discontinuity in the element. The diagrams detailing the FNM is redrawn for the reference purpose. The nodal position vectors of the floating nodes are defined by the crack position coordinates (points with coordinates  $\mathbf{x}_r$  and  $\mathbf{x}_s$ ), as shown in **Figure 4.2(a)**. As the crack occurs inside the element, the cracked element is split into two sub-elements  $\Omega_A$  and  $\Omega_B$ , depending on the direction of the crack [106]. The description concerning the floating nodes within the deformation domain can be found in the

preceding chapter. The final results of stiffness matrices and force vectors of the sub-elements are defined as,

$$\mathbf{K}_A = \int_{\Omega_A} \mathbf{B}_A^T \mathbf{D} \mathbf{B}_A d\Omega \quad \text{and} \quad \mathbf{K}_B = \int_{\Omega_B} \mathbf{B}_B^T \mathbf{D} \mathbf{B}_B d\Omega \quad (4.7)$$

$$\mathbf{f}_A = \int_{\Omega_A} \mathbf{N}^T \mathbf{b} d\Omega + \int_{\Gamma_t \cap \Gamma_{\Omega_A}} \mathbf{N}^T \bar{\mathbf{t}} d\Gamma \quad (4.8a)$$

$$\mathbf{f}_B = \int_{\Omega_B} \mathbf{N}^T \mathbf{b} d\Omega + \int_{\Gamma_t \cap \Gamma_{\Omega_B}} \mathbf{N}^T \bar{\mathbf{t}} d\Gamma \quad (4.8b)$$

The equilibrium equations for both sub-elements are written as,

$$\mathbf{K}_A \mathbf{d}_A = \mathbf{f}_A \quad \text{and} \quad \mathbf{K}_B \mathbf{d}_B = \mathbf{f}_B \quad (4.9)$$

In FNM framework, the split elements, tip element and transition element are the most prevalent. Tip element is the one in which the crack segment intersects the ahead standard element edge, while split elements are fully stress-free and detached. The floating node that is situated on the crack tip is unattended, therefore the transition element is required for the integration purpose as shown in **Figure 4.2(b)**. The detailed procedure for crack modelling using FNM can be found in literature [5,106,108].

### 4.2.3 Strain smoothing technique

In this section, we present a concise overview of the strain smoothing technique to ensure a comprehensive understanding of the topic. Strain smoothing enhances accuracy and convergence, especially with irregular meshes, at a slightly lower computational cost. It was first introduced in meshfree methods and later extended to FEM [113–116,133]. Linear exactness in the weak form is vital for convergence in nodal integration-based meshfree methods. The elements are divided into smoothing cells for strain smoothing. Using a constant smoothing function simplifies area integration to line integration along cell boundaries, negating the need for shape function gradients in stiffness matrix formation or field gradient computation. Linear integration is applied at cell edges following the given formulation. The formulation for strain smoothing is explained in the previous chapter, and the final equations are presented below.

$$\tilde{\boldsymbol{\varepsilon}}(\mathbf{x}_c) = \sum_{I=1}^n \tilde{\mathbf{B}}_I(\mathbf{x}_c) \mathbf{d}_I \quad (4.10)$$

where  $n$  is the number of nodes and  $\tilde{\mathbf{B}}_I$  is the smoothed strain matrix of node  $I$ . For 2D, it is written as,

$$\tilde{\mathbf{B}}_I(\mathbf{x}_c) = \begin{bmatrix} \tilde{b}_{I1}(\mathbf{x}_c) & 0 \\ 0 & \tilde{b}_{I2}(\mathbf{x}_c) \\ \tilde{b}_{I2}(\mathbf{x}_c) & \tilde{b}_{I1}(\mathbf{x}_c) \end{bmatrix} \quad (4.11)$$

where

$$\tilde{b}_{Ik}(\mathbf{x}_c) = \frac{1}{A_C} \int_{\Gamma_C} N_I(\mathbf{x}) n_k(\mathbf{x}) d\Gamma, \quad (k = 1, 2) \quad (4.12)$$

It can be transformed to its algebraic form as,

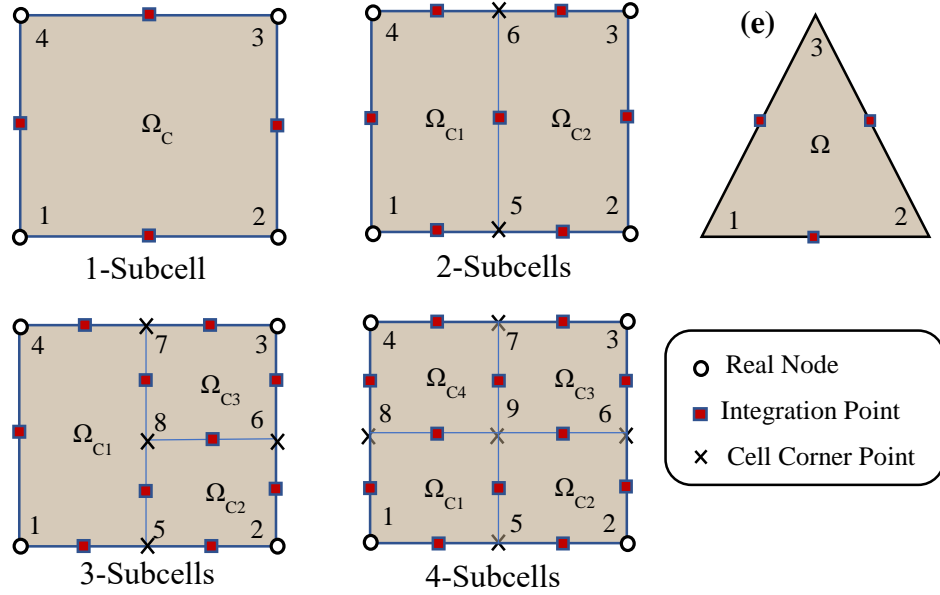


Figure 4.3: Quadratic element division into smoothing cells and integration scheme: (a) Q4, 1-cell (b) Q4, 2-cells (c) Q4, 3-cells (d) Q4, 4-cells and (e) T3, 1-cell.

$$\tilde{b}_{Ik}(\mathbf{x}_c) = \sum_{i=1}^M N_I(\mathbf{x}_i^{GP}) n_{ik}^C l_i^C \quad (4.13)$$

where  $\mathbf{x}_i^{GP}$  is the Gaussian point of the  $i^{\text{th}}$  boundary segment  $\Gamma_i^C$ ,  $l_i^C$  is the length of  $\Gamma_i^C$ ,  $M$  is the number of boundary segments, and  $n_i^C$  the outward unit normal vector of  $\Gamma_i^C$ .

### 4.3 Cohesive Zone Interface Model

In SFNM, though the quadrilateral elements (Q4) are used for meshing the problem domain, the element inside the domain may also have 3-node triangular elements (T3) at the split element cut by an arbitrary crack and inside the transition element. Therefore, both 3-node triangular and 4-node quadrilateral elements are used for modelling the crack discontinuity. In this analysis, 4-node quadrilateral elements or 4-node sub-elements are divided into 4 smoothing cells and T3 element is considered as single cell for numerical integration. Detailing of shape function values corresponding to 1 cell of T3 element and 4 cells of Q4 element is given in **Table 4.1** and **Table 4.2** respectively.

Table 4.1: Shape functions values at different sites (refer **Figure 4.3**) within T3 element

Site	Node 1	Node 2	Node 3	Description
1	1	0	0	Field node
2	0	1	0	Field node
3	0	0	1	Field node

Table 4.2: Shape functions values at different sites (refer **Figure 4.3**) within Q4 element

Site	Node 1	Node 2	Node 3	Node 4	Description
1	1	0	0	0	Field node
2	0	1	0	0	Field node
3	0	0	1	0	Field node
4	0	0	0	1	Field node
5	0.5	0.5	0	0	Edge midpoint
6	0	0.5	0.5	0	Edge midpoint
7	0	0	0.5	0.5	Edge midpoint
8	0.5	0	0	0.5	Edge midpoint
9	0.25	0.25	0.25	0.25	Intersection of two bi-medians

### 4.3 Cohesive Zone Interface Model

The inelastic region in the vicinity of the crack tip is approximated by the cohesive zone model, which accounts for the nonlinear region and considered as a straight line along the crack propagation path. The remaining domain is considered an elastic medium. **Figure 4.4** illustrates different zones around the fictitious crack tip, such as traction free zone, fracture process zone, and elastic domain. The implementation of cohesive zone

in the proposed SFNM framework is straightforward. By neglecting the body forces, the equilibrium **Eq. (4.5)** can be modified to **Eq. (4.14)**, as given below. Now, the weak form of the governing equation is a combination of strain energy, cohesive fracture energy, and external work done.

$$\int_{\Omega} \boldsymbol{\sigma}(\mathbf{u}) : \boldsymbol{\varepsilon}(\mathbf{v}) d\Omega + \int_{\Gamma_c} \mathbf{t}_c \cdot \boldsymbol{\Delta} d\Gamma = \int_{\Gamma_t} \bar{\mathbf{t}} \cdot \mathbf{v} d\Gamma \quad (4.14)$$

where  $\mathbf{t}_c$  is the cohesive traction vector and  $\boldsymbol{\Delta}$  is the displacement jump along the crack surface.

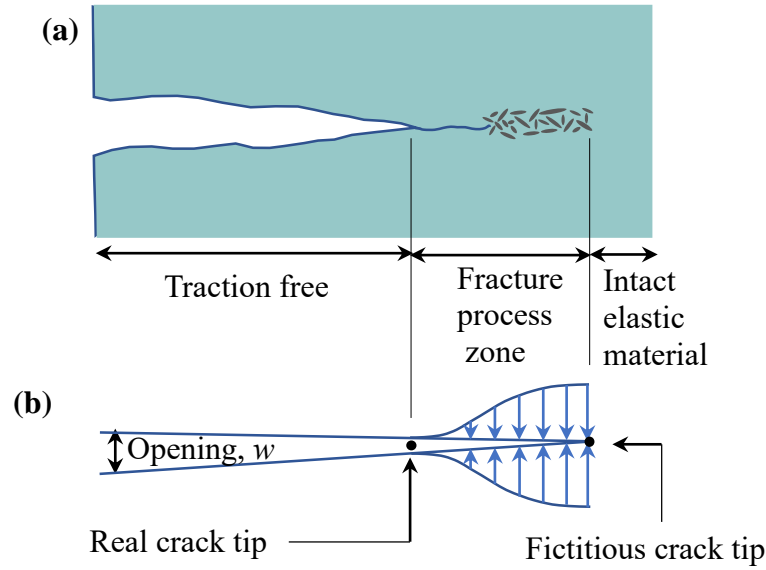


Figure 4.4: Schematic representation of fracture process zone; **(a)** crack with traction free, FPZ and intact elastic domain, **(b)** stress transfer inside the nonlinear FPZ.

In cohesive zone modelling, the traction separation law defines the mechanism of the failure of the fracture process zone. The peak value of traction transferred by the material in the fracture process zone is equal to the cohesive strength of the material. Intrinsic and extrinsic cohesive zone modelling are the extensively reported approaches in the literature to study the fracture behaviour in quasi-brittle and composite materials [151–154]. In this chapter, intrinsic cohesive zone model, based on the PPR approach [155,156], is considered for the numerical analysis. This model describes both the tangential and normal cohesive tractions along the FPZ interface. The potential function ( $\Psi$ ) depends on the fracture energies and separation variables in normal and tangential directions, and is given as,

$$\begin{aligned} \Psi(\Delta_n, \Delta_t) = & \min(\phi_n, \phi_t) \\ & + \left[ \Gamma_n \left( 1 - \frac{\Delta_n}{\delta_n} \right)^\alpha \left( \frac{m}{\alpha} + \frac{\Delta_n}{\delta_n} \right)^m \right. \\ & \left. + \langle \phi_n - \phi_t \rangle \right] \left[ \Gamma_t \left( 1 - \frac{|\Delta_t|}{\delta_t} \right)^\beta \left( \frac{n}{\beta} + |\Delta_t| \delta_t \right)^n + \langle \phi_t - \phi_n \rangle \right] \end{aligned} \quad (4.15)$$

where  $\langle . \rangle$  is the Macauley bracket.  $\phi_n, \Gamma_n, \delta_n, \Delta_n$  represent the fracture energy, energy constant, crack opening width and separation at crack interface respectively, in the normal direction. The same variables with subscripts 't' means the variables in the tangential direction. Exponents  $m$  and  $n$  are associated with the initial slope, whereas  $\alpha, \beta$  act as shape parameters constants. The first derivative of the PPR potential provides cohesive tractions under the softening region.

$$\mathbf{t}_c(\Delta_n, \Delta_t) = \begin{Bmatrix} \partial \Psi / \partial \Delta_t \\ \partial \Psi / \partial \Delta_n \end{Bmatrix} = \begin{Bmatrix} T_t(\Delta_n, \Delta_t) \\ T_n(\Delta_n, \Delta_t) \end{Bmatrix} \quad (4.16)$$

The second derivative of the PPR potential results in the tangent stiffness matrix,

$$\mathbf{D}_c(\Delta_n, \Delta_t) = \begin{bmatrix} D_{tt} & D_{tn} \\ D_{nt} & D_{nn} \end{bmatrix} = \begin{bmatrix} \partial^2 \Psi / \partial \Delta_t^2 & \partial^2 \Psi / \partial \Delta_t \partial \Delta_n \\ \partial^2 \Psi / \partial \Delta_n \partial \Delta_t & \partial^2 \Psi / \partial \Delta_n^2 \end{bmatrix} \quad (4.17)$$

The considered cohesive zone model works for four stages: contact condition, softening condition, unloading-reloading, and complete failure. The complete failure separation is evaluated by equating the fracture energy to the area under the traction–separation curve.

#### 4.3.1 Kinematics of the interfacial surface

The displacement fields are computed from the nodal displacement with the help of shape functions as,

$$\mathbf{u} = \mathbf{N} \mathbf{d} \quad (4.18)$$

$$\bar{\mathbf{u}} = \mathbf{R} \mathbf{d} \quad (4.19)$$

$$\bar{\Delta} = \mathbf{L} \bar{\mathbf{u}} \quad (4.20)$$

$$\Delta = \mathbf{N} \bar{\Delta} \quad (4.21)$$

where  $\mathbf{d}$  denotes the nodal displacements,  $\mathbf{N}$  is the shape function matrix,  $\bar{\mathbf{u}}$  is the local nodal displacements and  $\bar{\Delta}$  is the local displacement jump or local separation.  $\Delta$  denotes the separation along the cohesive surface element. The rotational matrix  $\mathbf{R}$  is given by,

$$\mathbf{R} = \begin{bmatrix} \Upsilon & 0 & 0 & 0 \\ 0 & \Upsilon & 0 & 0 \\ 0 & 0 & \Upsilon & 0 \\ 0 & 0 & 0 & \Upsilon \end{bmatrix} \quad (4.22)$$

where transformation matrix ( $\Upsilon$ ) is given as,

$$\Upsilon = \begin{bmatrix} \cos\theta & \sin\theta \\ -\sin\theta & \cos\theta \end{bmatrix} \quad (4.23)$$

Local separation is given in **Eq. (4.24)** which can be calculated with the help of the  $\mathbf{L}$  operator given in **Eq. (4.25)**. The  $\mathbf{L}$  operator is the local displacement-separation relation matrix.  $\mathbf{N}$  is the shape function matrix of 2 node linear elements given by **Eq. (4.26)**.

$$\bar{\Delta}_1 = \bar{u}_7 - \bar{u}_1, \bar{\Delta}_2 = \bar{u}_8 - \bar{u}_2, \bar{\Delta}_3 = \bar{u}_5 - \bar{u}_3, \bar{\Delta}_4 = \bar{u}_6 - \bar{u}_4. \quad (4.24)$$

$$\mathbf{L} = \begin{bmatrix} -1 & 0 & 0 & 0 & 0 & 0 & 1 & 0 \\ 0 & -1 & 0 & 0 & 0 & 0 & 0 & 1 \\ 0 & 0 & -1 & 0 & 1 & 0 & 0 & 0 \\ 0 & 0 & 0 & -1 & 0 & 1 & 0 & 0 \end{bmatrix} \quad (4.25)$$

$$\mathbf{N} = \begin{bmatrix} N_1 & 0 & N_2 & 0 \\ 0 & N_1 & 0 & N_2 \end{bmatrix} \quad (4.26)$$

Finally, the relation between global nodal displacement and the separation along the cohesive surface can be written in a form as given in **Eq. (4.27)**.

$$\Delta = \mathbf{B}_c \mathbf{d} \quad (4.27)$$

where  $\mathbf{B}_c = \mathbf{NRL}$ . The internal force vector and cohesive stiffness matrix are given by **Eq. (4.28)** and **Eq. (4.29)** respectively for the cohesive surface elements.

$$\mathbf{f}_c = \int_{\Gamma_c} \mathbf{B}_c^T \mathbf{T}_c d\Omega \quad (4.28)$$

$$\mathbf{K}_c = \frac{\partial \mathbf{f}_c}{\partial \mathbf{d}} = \int_{\Gamma_c} \mathbf{B}_c^T \frac{\partial \mathbf{T}_c}{\partial \Delta} \frac{\partial \Delta}{\partial \mathbf{d}} d\Omega = \int_{\Gamma_c} \mathbf{B}_c^T \frac{\partial \mathbf{T}_c}{\partial \Delta} \mathbf{B}_c d\Omega \quad (4.29)$$

#### 4.3.2 Implementation of a cohesive element in SFNM

The implementation of cohesive element in SFNM is shown in **Figure 4.5** for a quadrilateral element. In SFNM, the quadrilateral element having 4 standard nodes at the corners is divided into two sub-elements along the direction of the crack growth with the help of floating nodes. Then, a line element ‘AB’ (cohesive element) is inserted between these two sub-elements using floating nodes. The node numbering is considered counter clockwise for the sub-elements as well as for the cohesive element, and the nodal connectivity matrix for sub-elements and cohesive elements is defined as; first sub-element [1 2 5 6], second sub-element [7 8 3 4] and cohesive element [6 5 8 7]. For 2D analysis, each standard and the floating node has 2 degrees of freedom.

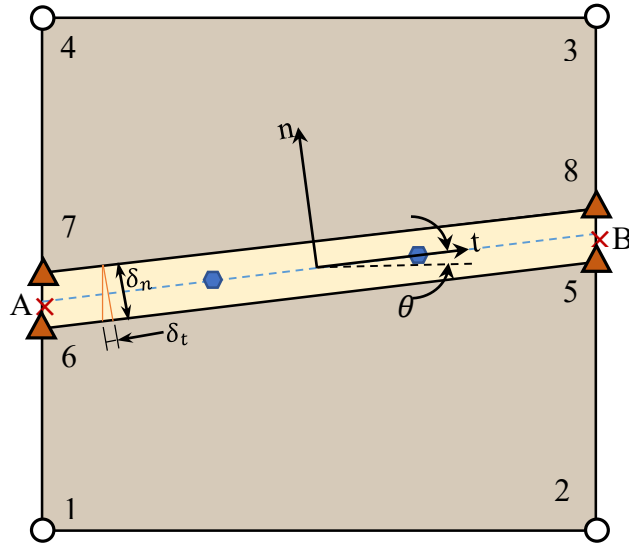


Figure 4.5: Representation of the cohesive element inside FPZ as per the crack propagation direction. Dotted line defines the linear cohesive element to calculate displacement separation. Two hexagonal points on the linear cohesive element denotes integration points.

Therefore, an intact element has 8 nodal displacement quantities, hence global nodal displacement quantities for an intact Q4 element are represented by  $d_1, d_2, d_3, d_4, d_5, d_6, d_7, d_8$  and the local nodal displacement quantities as  $\bar{u}_1, \bar{u}_2, \bar{u}_3, \bar{u}_4, \bar{u}_5, \bar{u}_6, \bar{u}_7, \bar{u}_8$ . Similarly, the cohesive surface element has 8 global nodal displacements quantities as  $d_9, d_{10}, d_{11}, d_{12}, d_{13}, d_{14}, d_{15},$  and  $d_{16}$ . The points ‘A’ and ‘B’ shown in **Figure 4.5** are taken as the midpoints of the floating node coordinates along the vertical edge



side. Two integration points are considered and shown with hexagon along the 1D element for the integration purpose. The local coordinate system ( $n$ - $t$ ) is shown in **Figure 4.5** in tangential and normal directions. Using **Eq. (4.15)** to **Eq. (4.29)** the cohesive stiffness matrix and the cohesive force vector can be calculated for the cohesive element.

#### 4.4 Crack Growth and Direction Criterion

To determine the crack propagation direction, a particular requisite criterion needs to be prescribed. The crack propagates when the crack driving forces exceed the crack resisting forces in the FPZ. Hence, correct estimation of the induced stresses at crack tip becomes extremely important. The stresses at local points computed inside the FPZ may have a significant variation and may lead to the unreliable prediction of the stresses at tip. In order to avoid the influence of the local stress values near the crack tip, a nonlocal equivalent stress value can be calculated [157]. In this analysis, the nonlocal von Mises stress is calculated at the crack tip using the averaging technique. The equivalent stress

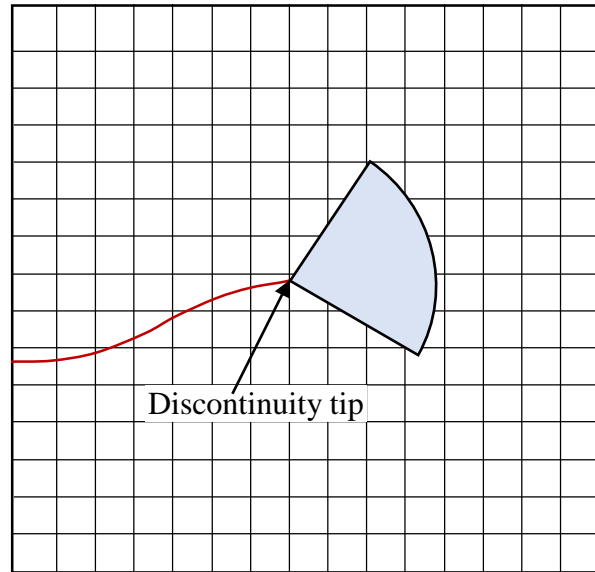


Figure 4.6: Illustration of crack growth criterion. A 90° sector considered for the computation of nonlocal stresses at crack tip using weighted average method

is determined by applying the weighted average technique by using **Eq. (4.30)** [17]. The local stresses calculated in the region behind the fracture tip have little impact on the equivalent stress calculation because of the stress-free crack space. Additionally, the crack does not advance in the reverse direction. A symmetric area sector is consequently taken into consideration for the accurate assessment of the stresses at the vicinity of the

tip. Thus, a 90° circular sector is considered as shown in **Figure 4.6** for calculating the equivalent stress. The weight function is given in **Eq. (4.31)**, where length  $l$  determines how fast the weight function decay from the crack tip and  $A_i$  is the associated area. The length is taken as 4 times the size of the element for the weighted averaging.  $\bar{\sigma}$  represents the nonlocal weighted average stress. The calculated stress is compared with the tensile strength of the material. If the computed value is greater than the tensile strength of the material, then the crack segment is added else the applied load is further increased.

$$\bar{\sigma} = \frac{\sum_{i=1}^{n_G} \sigma_i w_i A_i}{\sum_{i=1}^{n_G} w_i A_i} \quad (4.30)$$

$$w(r) = \frac{1}{(2\pi)^{3/2} l^3} \exp\left(-\frac{r^2}{2l^2}\right) \quad (4.31)$$

The direction in which the crack propagates is required after the crack growth criterion is fulfilled. The crack growth length is added in the currently existing crack. One such criterion based on the energy conservation principle [158], asserts that a crack propagates when the strain energy release rate is greater than the energy dissipation rate in FPZ. The other most extensively adopted criterion is the stress intensity factor (SIF) based criterion [2,159] used for the quasi brittle material for mode I and mixed mode applications. To implement this criterion, the discrete set of equations is solved to obtain the displacements, and the stress intensity factor values are extracted. In this study, the maximum circumferential stress criterion is employed to obtain the direction of crack growth. The direction of crack growth  $\theta_c$ , at each crack increments are obtained using the following expression,

$$\theta_c = 2 \arctan \frac{1}{4} \left\{ \frac{K_I}{K_{II}} \pm \text{sign}(K_{II}) \sqrt{\left(\frac{K_I}{K_{II}}\right)^2 + 8} \right\} \quad (4.32)$$

where  $K_I$  and  $K_{II}$  are the mode I and mode II SIFs, and are obtained using interaction integral approach [160].

## 4.5 Numerical Examples

In this section, to illustrate the accuracy and effectiveness of the proposed SFNM, first mode I, mode II patch problems are considered for the simulation. Once the method is

verified, the versatility and adaptability of the proposed approach are assessed by solving the standard fracture problems taken from the literature and the outcomes of the simulations are compared with the available results. For this purpose, first three-point bending problems under mode I and mixed mode are solved. Finally, the L-shaped panel problem is analysed under the mixed mode loading condition. All the simulations are performed under plane strain conditions, and a uniform initial mesh of quadrilateral elements is used for all the problems.

#### 4.5.1 Patch test validation of SFNM

First, the proposed framework is tested by implementing it on a single-element patch test. To check the robustness of the method, both tensile and shear loading cases are considered and results are compared with the literature. The cohesive element insertion is flexible in the proposed framework and depends on the nature of the problem. It can be inserted along the edge of the element and also across the element in any arbitrary direction.

##### 4.5.1.1 Patch test under mode I loading

To verify the implementation of the SFNM coupled with cohesive TSL, here, we consider a patch test (an element) and perform the pull test analysis by applying uniaxial loading on the upper edge and fixing the bottom edge of the element. Specimen size of  $0.1\text{m} \times 0.1\text{m}$  is considered for the mode I test. The analysis is performed by using in-house generated Matlab code. The material properties such as modulus of elasticity and

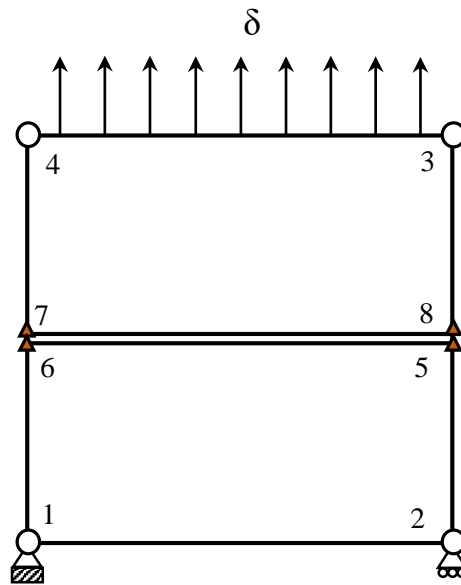


Figure 4.7: Geometry and boundary conditions of mode I specimen with cohesive element inserted horizontally at the centre.

Poisson's ratio are taken as 32 GPa and 0.2 respectively. Here the displacement-controlled approach is adopted and the displacement is applied at the top edge in the vertical direction. The geometry with boundary conditions shown in **Figure 4.7** demonstrates the element discretization into two quadrilateral sub-elements (nodal connectivity: [1 2 5 6] and [7 8 3 4]) and one cohesive element (nodal connectivity: [6 5 8 7]). Here 1,2,3 and 4 are the standard field nodes, whereas 5,6,7 and 8 are the inserted

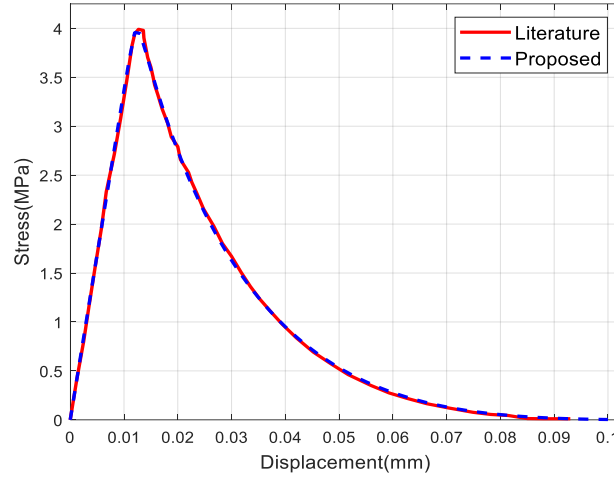


Figure 4.8: Comparison of stress vs displacement curve of proposed method and literature [49] results under mode I test

floating nodes which are located at the intersection point of the cohesive crack segment with the element edges. The intersection points are computed based on the crack

Table 4.3: Material properties and fracture parameters for mode I test

Property Name/Parameters	Symbol	Value	Unit
Young's modulus	$E$	32	GPa
Poisson's ratio	$\nu$	0.2	-
Fracture energy (normal)	$\phi_n$	100	N/m
Fracture energy (tangential)	$\phi_t$	200	N/m
Tensile strength	$\sigma_{max}$	4	MPa
Shear strength	$\tau_{max}$	3	MPa
Shape parameter normal	$\alpha$	5	-
Shape parameter tangential	$\beta$	1.6	-
Normal initial Slope indicator	$\lambda_n$	0.005	-
Tangential initial Slope indicator	$\lambda_t$	0.005	-

propagation criterion as discussed in Section 4.4. In this case, the cohesive element is inserted in the mid-plane of the element along the  $x$ -direction i.e. at  $0^\circ$  angle which is assumed as the crack propagation direction in the cohesive zone ahead of the crack tip for given boundary conditions. This angle may be taken as nonzero depending on the boundary conditions. The material properties and fracture parameters are given in **Table 4.3**. The variation of stress with displacement is plotted in **Figure 4.8**. From the figure, it can be observed that the stress increases until it reaches the cohesive strength (tensile strength) of the material followed a softening behaviour after the peak value equal to the cohesive strength. The obtained response is similar to the literature results of PPR [156]. The sub-element displacement separation and normal stress contour corresponding to the crack growth for this test are shown in **Figure 4.9**. The stress contour illustrates the cohesive stress variation acting in the sub-elements due to cohesive element. The stress variation from zero to peak and subsequently drop to zero in the softening region, depicts the variation of the stresses with the increase in displacement separation. Finally, there is no change in the stresses after the displacement separation exceeds the decohesive value. From the test, it can be observed that the proposed framework is able to model the fracture behaviour in quasi-brittle material under mode I loading.

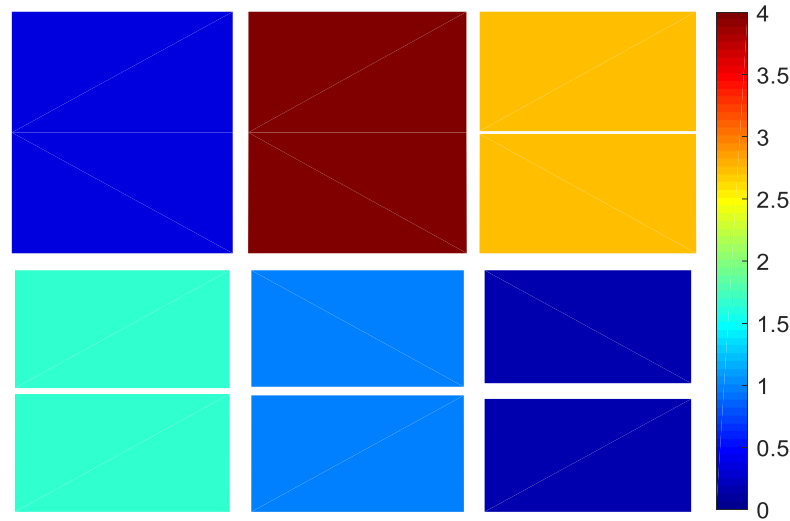


Figure 4.9: Displacement (separation) and normal stress distribution in sub-elements during mode I specimen test

#### 4.5.1.2 Patch test under mode II loading

In this section, the patch test problem under mode II loading is considered. The specimen size of  $0.1\text{m} \times 0.1\text{m}$  is subjected to both tensile and compressive loadings. The geometry

and boundary conditions are shown in **Figure 4.10**, where  $\delta$  is the applied displacement in the negative  $x$ - and positive  $y$ -direction. The specimen is initially discretized with one quadrilateral (Q4) element. To model the cohesive crack, it is further divided into 2 triangular sub-elements (nodal connectivity: [1 2 6] and [8 3 4]) and one cohesive element (nodal connectivity: [6 2 8 4]) inserted along the diagonal of the specimen with

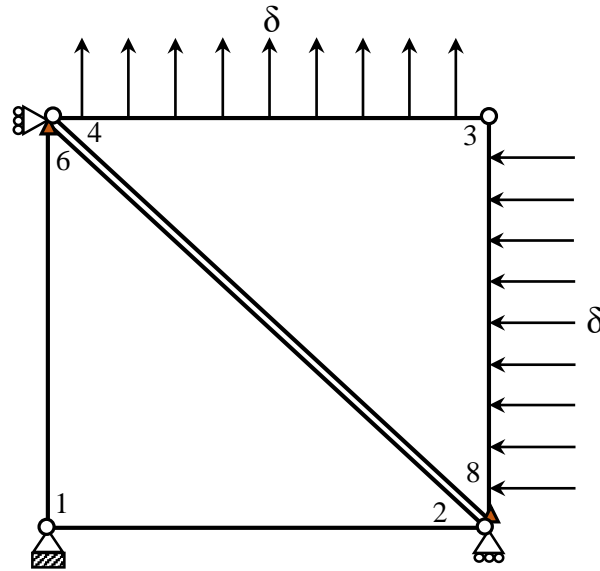


Figure 4.10: Geometry and boundary conditions of mode II specimen with cohesive element along the diagonal

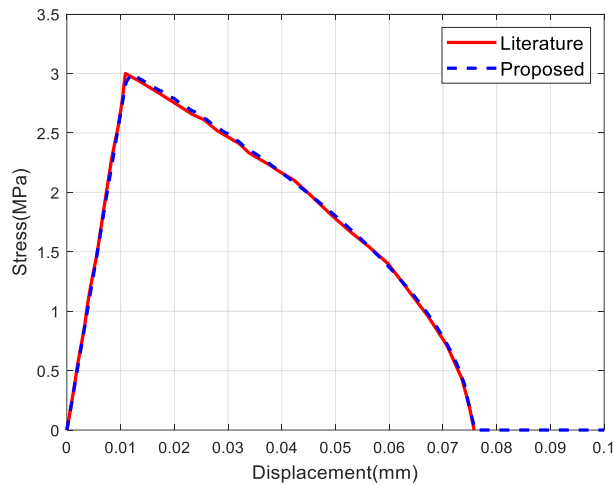


Figure 4.11: Comparison of stress vs displacement curve of proposed method and literature [49] results under mode II test

the help of additional floating nodes. In this case, only 2 floating nodes are sufficient to form the cohesive element, and the remaining floating nodes are condensed for the computational purposes due to the inactiveness nature of these nodes. The material

properties and fracture parameters remain the same as given in **Table 4.3**. The stress-displacement variation of the analysis is plotted in **Figure 4.11** along with the literature results [156] and it shows that the obtained results trace the exact reference curve. From the plot, one can predict the decohesive displacement separation as approximate 0.075 mm and beyond that, there is no resistance from the cohesive element side. From the test, it can be observed that the proposed framework is also able to model the fracture behaviour in quasi-brittle material under mode II loading condition.

#### 4.5.2 Three-point bending test

To further check the effectiveness of the proposed framework, it is extended for simulating the three-point bending beam test. A specimen of size  $0.3048\text{m} \times 0.762\text{m}$  is considered for mode I analysis. The geometry and boundary conditions of the specimen

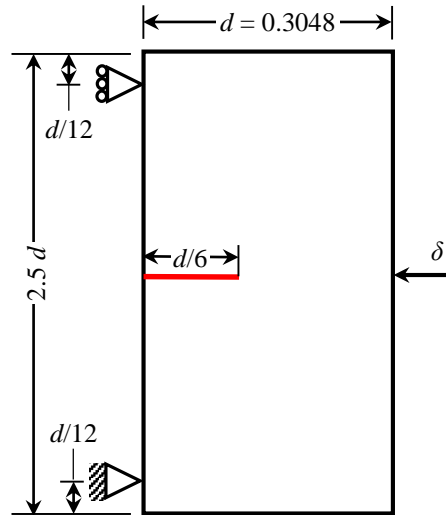


Figure 4.12: Geometry and boundary conditions of three-point beam specimen with an edge crack under mode I loading.

Table 4.4: Material properties and parameters for the three-point bending test

Property/Parameter Name	Symbol	Value	Unit
Young's modulus	$E$	27413	MPa
Poisson's ratio	$\nu$	0.18	-
Fracture energy	$G_f$	40.29	N/m
Tensile strength	$f_t$	2.886	MPa
Out plane thickness	$t$	38.1	mm

are shown in **Figure 4.12**. The thickness of specimen is taken equal to 0.0381m. An initial crack of length 0.051m is considered for the analysis. The displacement is applied at the middle point on the right edge of the specimen as shown in the figure. The beam is initially discretized with only Q4 elements under plane strain condition. The material properties and numerical parameters are taken from the literature [161] and given in **Table 4.4**. The obtained results are plotted as a structural force-displacement curve

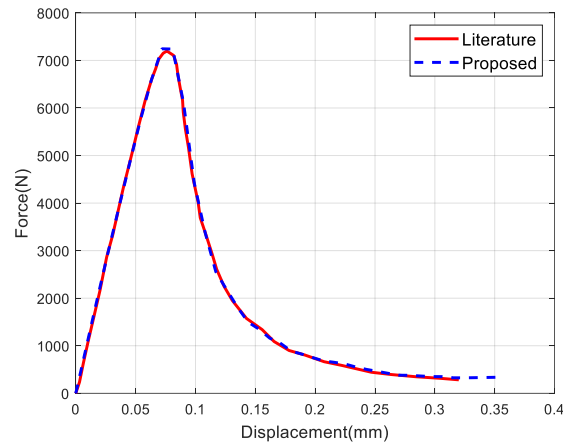


Figure 4.13: Comparison of Force vs displacement curve of proposed method and literature [55] results of three-point bending test under mode I loading

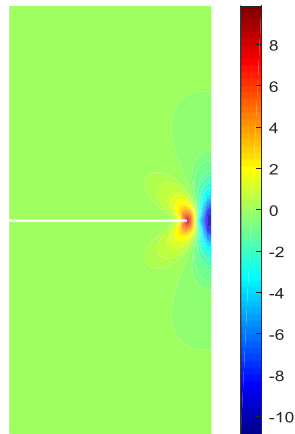


Figure 4.14: Stress contour of three-point bending test specimen.

shown in **Figure 4.13** and compared with the literature results. From the figure, it can be observed that the softening behaviour of the material starts just after the peak of the tensile strength of the material and is driven by the fracture energy. The problem is solved under mode I loading hence the crack propagation is straight i.e. at zero degrees



angle from the initial crack length. **Figure 4.14** displays the normal stress contour for the three-point bending test at final stage of loading. Thus, from the simulation we can conclude that the proposed framework is able to model the crack growth behaviour of quasi-brittle materials effectively and accurately.

#### 4.5.3 Mixed mode fracture in eccentrically notched beam

In this section, a three-point bending problem of eccentrically notched concrete beam is considered to capture the cohesive effects using SFNM [162,163]. The center-to-center distance between the supports is taken as  $2.5d$ , and the length of the beam is equal

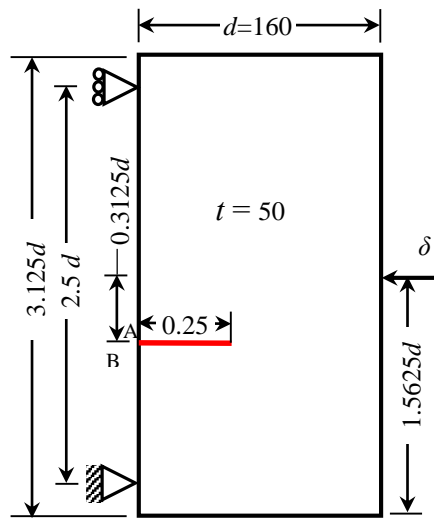


Figure 4.15: Geometry and boundary conditions of three-point beam specimen with eccentric crack under mixed mode loading

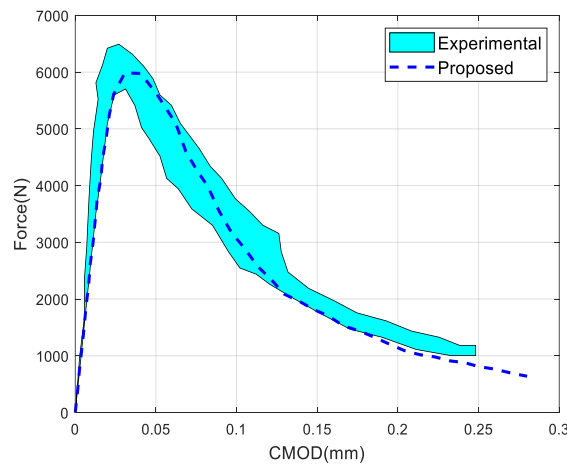


Figure 4.16: Comparison of Force vs CMOD curve of three-point bending test of proposed method with literature [56] results for eccentric crack under mixed mode loading

to  $3.125d$ . The analysis is performed by considering the beam depth ( $d$ ) value equal to 160 mm. The out-of-plane thickness ( $t$ ) is set to 50 mm. The specimen is subjected to mixed mode loading. The geometry and boundary conditions of the eccentrically notched beam are shown in **Figure 4.15**. The eccentricity of the initial notch is  $0.3125d$ . The detailed material properties and parameters associated with this numerical study are provided in **Table 4.5**. The points marked as *A* and *B* on the specimen are considered to record the crack mouth opening displacement (CMOD). The obtained force versus CMOD curve is plotted for this case and compared with the experimental one [162,163] as shown in **Figure 4.16**. The comparison of force versus CMOD shows that the peak load lies within the range of experimental data. Further, a normal stress contour obtained through proposed approach is also shown in **Figure 4.17**. The crack propagates towards the point of application of load, similar to the literature observations. From these results, it is observed that the proposed framework captures the crack propagation behaviour accurately even for curved crack growth problems.

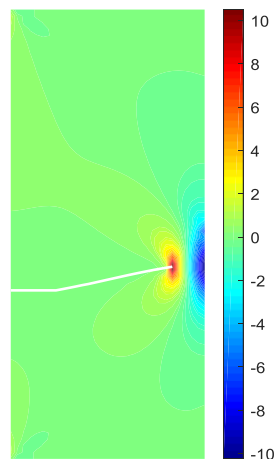


Figure 4.17: Stress contour of eccentrically loaded three-point bending specimen

Table 4.5: Material properties and parameters for three-point bending eccentrically notched beam test

Property/Parameter Name	Symbol	Value	Unit
Young's modulus	$E$	33.8	GPa
Poisson's ratio	$\nu$	0.2	-
Fracture energy	$G_f$	0.06	N/mm
Tensile strength	$f_t$	3.5	MPa
Out plane thickness	$t$	50	mm

#### 4.5.4 Mixed mode failure of an L-shaped panel

Finally, a mixed mode problem of the L-shaped panel is considered for numerical simulation. The geometry and boundary conditions of the L-shaped panel are shown in **Figure 4.18**. The bottom surface of the specimen is fixed and a vertical displacement ( $\delta$ ) is applied at point 'A' positioned 30 mm from the left vertical face. Point B is considered the crack initiation point. The L-shaped panel is discretized with an initial uniform mesh of Q4 element size of 5 mm. The material properties and numerical parameters are given in **Table 4.6**.

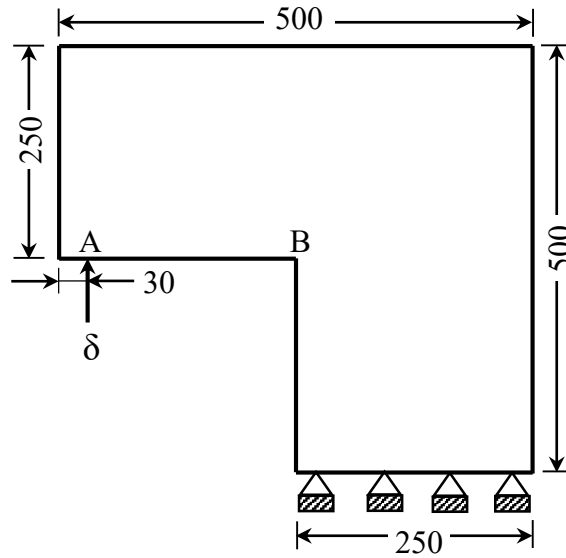


Figure 4.18: L-shape panel geometry with boundary conditions (all dimensions are in mm).

Table 4.6: Material properties and parameters for L-shaped panel

Property/Parameter Name	Symbol	Value	Unit
Young's modulus	$E$	20	GPa
Poisson's ratio	$\nu$	0.18	-
Fracture energy	$G_f$	0.13	N/mm
Tensile strength	$f_t$	2.9	MPa
Out plane thickness	$t$	100	mm

The L-shaped panel is considered without initial crack for the simulation under mixed loading. The maximum circumferential stress criterion is applied for finding out the initial fracture process zone direction and inserting the cohesive element in the domain. Similar to this, when the crack propagation criterion is met, the crack segment is extended further from the fictitious tip. The structural response of the L-shape panel

using the proposed SFNM framework is obtained and compared with the literature results in **Figure 4.19**. Further the deformed shape of the L-shape panel is shown in **Figure 4.20(a)** using a magnification factor of 25. Also the comparison of the obtained crack path with the available literature is shown in **Figure 4.20(b)**. From the **Figure 4.20**, it can be observed that the crack initiates exactly from the corner, similar to the

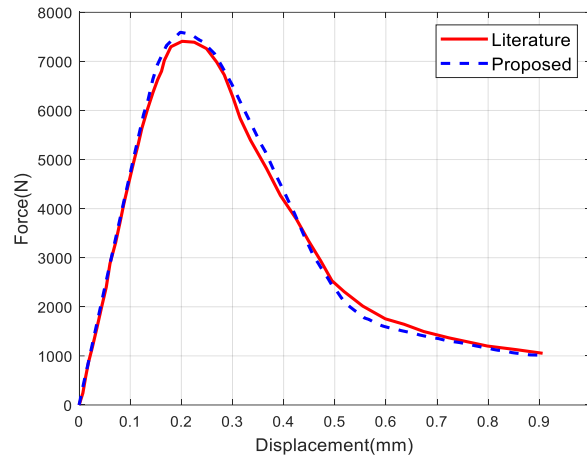


Figure 4.19: Comparison of force vs displacement curve of proposed method and literature [23] results of L-shaped panel under mixed mode loading.

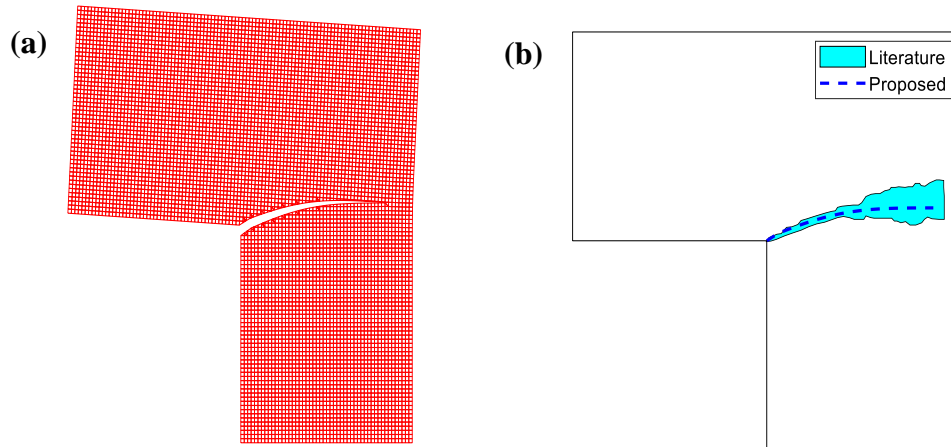


Figure 4.20: (a) L-shaped panel deformed shape (magnification factor 25), (b) Comparison of the crack path with experimental [23].

experimental observations. Finally, a normal stress contour is plotted for the L-shaped panel in **Figure 4.21**. Based on the comparison, it can be concluded that the proposed cohesive SFNM framework is able to reproduce the experimentally obtained structural response and crack pattern with good accuracy for mixed mode problems.

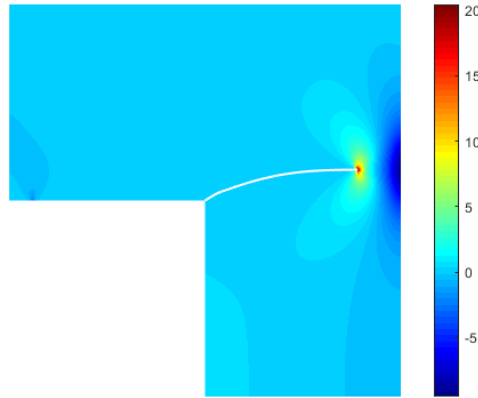


Figure 4.21: Stress Contour plot of L-shaped panel

## 4.6 Conclusions

In this chapter, smoothed floating node method is coupled with cohesive zone approach for modelling crack growth behaviour in quasi-brittle materials. The cell-based smoothing procedure is adopted for the integration of sub-elements and standard elements, and a potential-based intrinsic cohesive zone model is implemented to capture the nonlinear fracture behaviour of the material ahead of the crack tip. The SFNM combines the benefits of strain smoothing and the floating node method, making it an attractive method for solving fracture mechanics problems without the requirement of additional enrichment functions and remeshing during crack growth. The implementation of cohesive zone nonlinear behaviour in SFNM is straight forward. The assessment of the SFNM coupled with CZM is carried out for the straight and curved crack growth problems. The method is tested for the cohesive strengths of the material in the normal and tangential directions. The simulated examples have shown the robustness and effectiveness of the proposed numerical framework for solving generic fracture mechanics problems.

In this chapter, we conducted the analysis of nonlinearity within the fracture process zone of quasi-brittle materials under the influence of external mechanical loads. This analysis employs the SFNM technique coupled with cohesive zone modelling. In practical scenarios, thermal-induced stress is recognized as an influential factor, especially when the specimen faces thermal loads in conjunction with boundary constraints. These circumstances can greatly influence the crack growth behaviour. To address these factors, a comprehensive evaluation of these conditions will be conducted in the upcoming chapter.

Page left blank intentionally

## Chapter 5

### Thermo-elastic Brittle Fracture using SFNM with CZM

---

This paper presents an extension of the recently developed smoothed floating node method with cohesive zone approach to model crack growth in elastic materials under thermo-elastic loading conditions. The SFNM utilizes floating nodes to accurately model the crack by activating dormant nodes at intersection points of crack path and the corresponding element edges. Through the activation of floating nodes, the cracked element transforms into sub-elements, facilitating separate integration of each sub-element. A smoothing cell-based integration technique is employed to convert the area integral to line integral which mitigates the element distortion issues. The temperature distribution is initially determined across the entire domain, and then imposed as thermal loads in the 2D domain. The thermal stress intensity factor is calculated for both homogeneous and bi-material specimens using the interaction energy integral approach, and the crack propagation is predicted using circumferential stress criterion. The accuracy of the proposed framework is demonstrated with several benchmark problems of fracture mechanics. The developed framework yields comparable results with the available literature with less modelling complexity.

#### 5.1 Introduction

In engineering, the behaviour of materials under various loading conditions is of great interest. These materials can be subjected to different types of loads, such as mechanical, thermal, or a combination of both. Thermo-mechanical loading can occur in many engineering applications, such as in aerospace, fuel cells, automotive, and power generation industries. One of the key challenges in analysing materials under thermo-mechanical loading is the presence of thermal stresses. These stresses arise due to the difference in thermal expansion coefficients between different materials, or due to changes in temperature within the material itself. In addition to causing cracks in materials, the temperature fluctuations also induce changes in the material's microstructure, which in turn have a significant impact on its mechanical properties and behaviour. Mechanical characteristics, such as weight, strength, and stiffness, primarily in concrete, start to deteriorate at temperatures beyond 300 °C, which causes the material

to fracture [164]. Thermal stresses act in addition to the mechanical stresses, and significantly affect the propagation of cracks in the material. To properly analyse materials under thermo-mechanical loading, it is important to take into account the presence of thermal stresses. This requires a comprehensive understanding of the material properties, as well as accurate modelling techniques that can capture the behaviour of the material under these conditions. As a result, numerous analytical and numerical techniques have been developed by researchers to evaluate steady state thermo-mechanical fracture problems. In order to get rid of drawbacks posed by discontinuity by using FEM only, advanced numerical methods are necessary to analyse the fracture behaviour of the growing cracks. In the context of the advanced numerical technique, this study aims to investigate the behaviour of a cracked specimen under steady state thermo-elastic loading conditions using the smoothed floating node method in conjunction with CZM. The employed method avoids the use of the virtual or enriched nodes to represent the crack discontinuity and ensures the real positioning of the floating nodes as per the crack growth orientation.

The chapter is structured as follows: In Section 5.2, smoothed floating node method formulation with implementation is described. In Section 5.3, governing equations, and temperature framework is discussed. Further, the implementation of cohesive zone approach into SFNM is described in Section 5.4. The extraction of the SIFs for homogeneous and inhomogeneous materials is presented in Section 5.5. Crack growth evaluation scheme is also provided in the same section. Section 5.6, illustrates the method through numerical examples involving static and crack propagation under different thermo-elastic loading conditions. Section 5.7, summarizes the findings and conclusions drawn from the study.

## 5.2 Smoothed Floating Node Method

In this section, the formulation and implementation of the smoothed floating node method is presented in reference to the cracked domain. **Figure 5.1** illustrates the utilization of the floating node method (FNM), which demonstrates the presence of discontinuity within the element. The domain's discretized mesh includes various types of elements such as intact, split, tip, and transition elements. Each element possesses floating nodes and real nodes with their corresponding dofs as shown in **Figure 5.2**. When there is no crack present, the floating nodes within each element remain inactive, resulting in a structure that resembles a regular finite element with only the real nodes.



However, as soon as a crack appears, these floating nodes become active to accurately represent the crack discontinuity [5,106,108]. In contrast to XFEM, the floating nodes in this model precisely depict their position along the path of crack growth. The element containing the crack is divided into two or more sub-elements depending on the location of the crack, and their nodal coordinate vectors are defined accordingly. The vectors of nodal coordinates for the element that is split into two sub-elements  $\Omega_A$  and  $\Omega_B$  (Figure 5.1) are defined as follows:

$$\mathbf{x}_{\Omega_A}^T = [\mathbf{x}_r^T, \mathbf{x}_s^T, \mathbf{x}_3^T, \mathbf{x}_4^T] \quad \text{and} \quad \mathbf{x}_{\Omega_B}^T = [\mathbf{x}_1^T, \mathbf{x}_2^T, \mathbf{x}_s^T, \mathbf{x}_r^T] \quad (5.1)$$

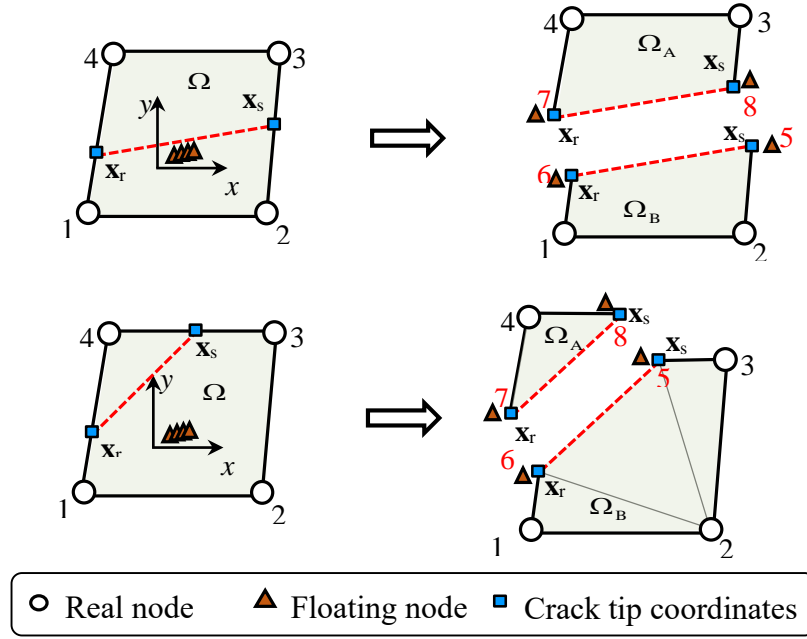


Figure 5.1: Schematic representation of strong discontinuity of an element dividing into sub-elements.

These nodal vectors of the sub domains  $\Omega_A$  and  $\Omega_B$  are further used to calculate the stiffness matrix and force vectors individually.

$$\mathbf{K}_A = \int_{\Omega_A} \mathbf{B}_A^T \mathbf{D} \mathbf{B}_A \det(\mathbf{J}_A) d\Omega \quad \text{and} \quad \mathbf{K}_B = \int_{\Omega_B} \mathbf{B}_B^T \mathbf{D} \mathbf{B}_B \det(\mathbf{J}_B) d\Omega \quad (5.2)$$

$$\mathbf{f}_A = \int_{\Omega_A} \mathbf{N}^T \mathbf{b} \det(\mathbf{J}_A) d\Omega + \int_{\Gamma_t \cap \Gamma_{\Omega_A}} \mathbf{N}^T \bar{\mathbf{t}} \det(\mathbf{J}_A) d\Gamma \quad (5.3a)$$

$$\mathbf{f}_B = \int_{\Omega_B} \mathbf{N}^T \mathbf{b} \det(\mathbf{J}_B) d\Omega + \int_{\Gamma_t \cap \Gamma_{\Omega_B}} \mathbf{N}^T \bar{\mathbf{t}} \det(\mathbf{J}_B) d\Gamma \quad (5.3b)$$

$$[\mathbf{K}_A]\{\mathbf{u}_A\} = \{\mathbf{f}_A\} \quad \text{and} \quad [\mathbf{K}_B]\{\mathbf{u}_B\} = \{\mathbf{f}_B\} \quad (5.4)$$

Finally, the equilibrium equation of the floating node element is the assembly of the two sub-elements, and is given as,

$$[\mathbf{K}]\{\mathbf{u}\} = \{\mathbf{f}\} \quad (5.5)$$

where  $\mathbf{K} = \begin{bmatrix} \mathbf{K}_A & \\ & \mathbf{K}_B \end{bmatrix}$ ,  $\mathbf{u}^T = [\mathbf{u}_A^T, \mathbf{u}_B^T]$  and  $\mathbf{f}^T = [\mathbf{f}_A^T, \mathbf{f}_B^T]$  when the two sub-elements are fully separated.

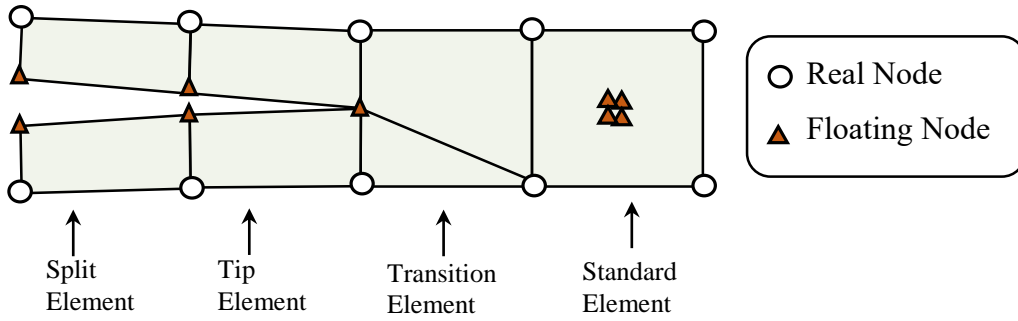


Figure 5.2: Representation of different types of elements in domain under strong discontinuity.

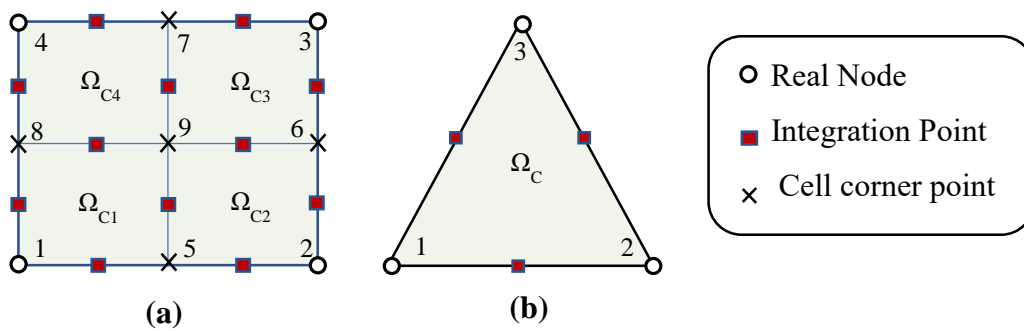


Figure 5.3: Quadrilateral and Triangular elements division into smoothing cells and integration scheme: (a) Q4, 4-cells and (b) T3, 1-cell.

The floating node method is implemented by utilizing the equations mentioned earlier. Further, the smoothing procedure employs a strain smoothing technique [40,41] for each smoothing cell within an element, as shown in **Figure 5.3**. In this process, the area integration for each cell is transformed into line integration along its boundaries using a

constant smoothing function. This eliminates the need to compute the gradient of shape functions while determining field gradients and forming the stiffness matrix. **Figure 5.3** illustrates the integration points and field nodes for a specified number of cells. The gradient of displacement for each smoothing cell within an element, utilizing the smoothing function, is presented as follows [133,134,165]

$$\nabla u^h(\mathbf{x}_C) = \int_{\Omega} \nabla u^h(\mathbf{x}) \phi(\mathbf{x} - \mathbf{x}_C) d\Omega \quad (5.6)$$

After simplifying **Eq. (5.6)** and substituting the constant area function, the smoothed strain can be obtained and given as,

$$\tilde{\boldsymbol{\epsilon}}^h(\mathbf{x}_C) = \sum_{I=1}^n \tilde{\mathbf{B}}_I(\mathbf{x}_C) u_I \quad (5.7)$$

where  $\tilde{\mathbf{B}}_I$  is the smoothed strain matrix. For 2D, it is written as,

$$\tilde{\mathbf{B}}_I(\mathbf{x}_C) = \begin{bmatrix} \tilde{b}_{I1}(\mathbf{x}_C) & 0 \\ 0 & \tilde{b}_{I2}(\mathbf{x}_C) \\ \tilde{b}_{I2}(\mathbf{x}_C) & \tilde{b}_{I1}(\mathbf{x}_C) \end{bmatrix} \quad (5.8)$$

$$\text{where } \tilde{\mathbf{b}}_{Ik}(\mathbf{x}_C) = \frac{1}{A_C} \int_{\Gamma_C} \mathbf{N}_I(\mathbf{x}) n_k(\mathbf{x}) d\Gamma, \quad (k = 1, 2)$$

where  $A_C = \int_{\Omega_C} d\Omega$  and  $\Omega_C$  is the smoothing cell. If one Gaussian point is used for line integration along each segment of the boundary  $\Gamma_i^C$  of  $\Omega_C$ , the above equation can be transformed to its algebraic form as,

$$\tilde{\mathbf{b}}_{Ik}(\mathbf{x}_C) = \sum_{i=1}^M \mathbf{N}_I(\mathbf{x}_i^{GP}) n_{ik}^C l_i^C \quad (5.9)$$

where  $\mathbf{x}_i$  is the Gaussian point of the piecewise boundary segment of  $\Gamma_i^C$ ,  $l_i^C$  is the length of boundary segment,  $\mathbf{N}_I$  is the shape function of node I and  $n_i^C$  is the outward unit normal vector of the boundary segment. Once the smoothed gradient matrix over each smoothing cell is evaluated, the smoothed element stiffness matrix can be obtained by assembly from all the sub-cells in the element and is given as,

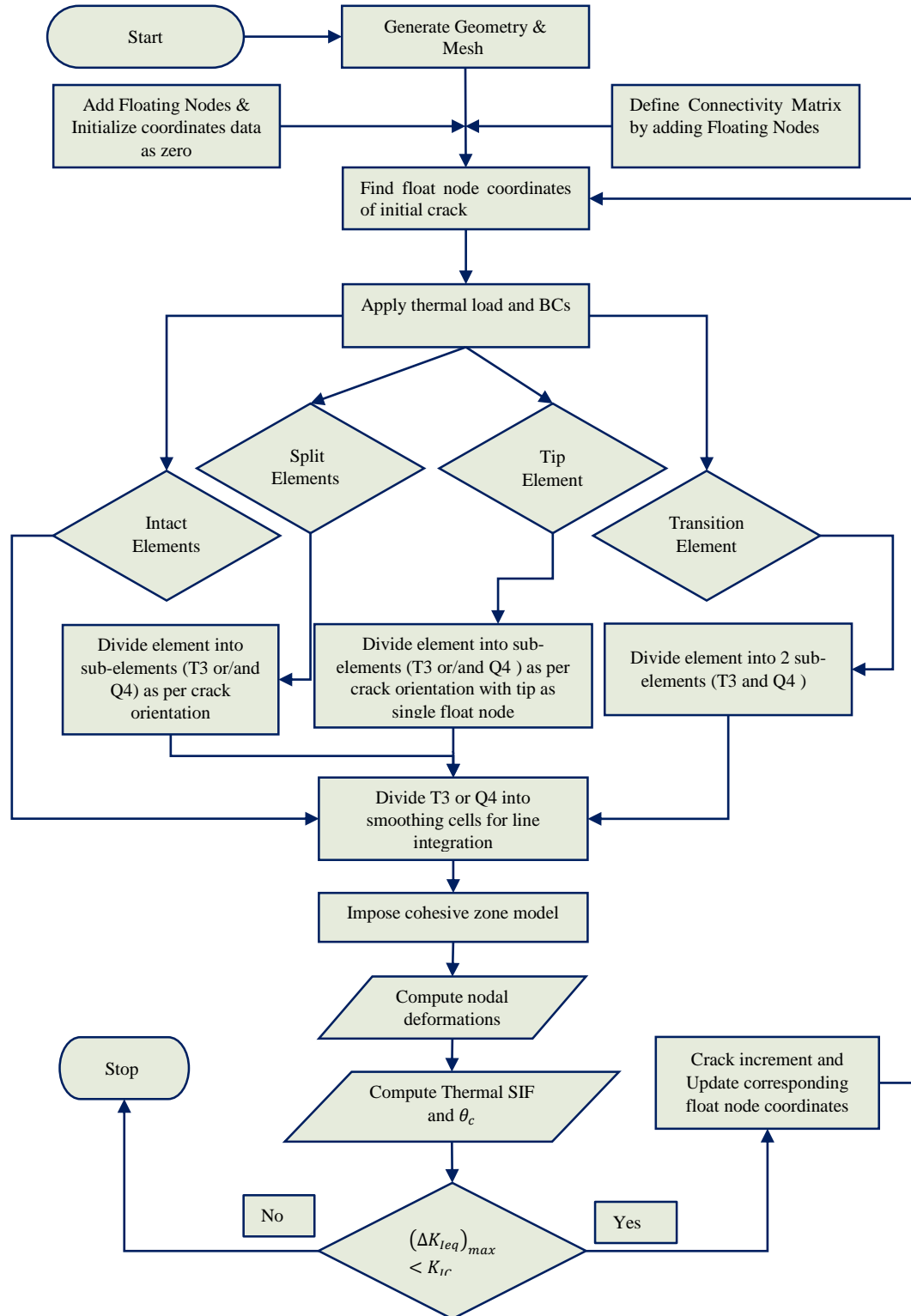


Figure 5.4: Flow chart of SFNM to model crack propagation under thermo-elastic loading conditions.

$$\mathbf{K}_e = \sum_c \tilde{\mathbf{B}}_c^T \mathbf{C} \tilde{\mathbf{B}}_c A_c \quad (5.10)$$

where  $\tilde{\mathbf{B}}_c$  smoothed gradient matrix of the single sub-cell. **Figure 5.4** presents a comprehensive step-by-step process for applying the SFNM method to simulate crack discontinuity. The procedure is outlined specifically for thermo-mechanical loading conditions in a steady state. The use of SFNM enhances both accuracy and convergence rate. Details regarding errors in L2 norm and convergence analysis utilizing SFNM can be found in the reference [108].

### 5.3 Governing Equations

The planar domain, as depicted in **Figure 5.5**, is divided into different parts denoted as  $\Gamma_u$ ,  $\Gamma_t$ ,  $\Gamma_T$  and  $\Gamma_c$ . On the boundary  $\Gamma_u$ , displacement boundary conditions are applied, while tractions are enforced on  $\Gamma_t$ . The boundary  $\Gamma_T$  is subjected to temperature fields while the boundary  $\Gamma_c$  is kept traction free. The steady-state heat conduction in a cracked domain, along with thermo-elastic equilibrium considering small displacements, can be described as follows [166],

$$-\nabla \cdot \mathbf{q} + Q = 0 \quad (5.11)$$

$$\mathbf{q} = -k \nabla T \quad (5.12)$$

$$\nabla \cdot \boldsymbol{\sigma} + \mathbf{b} = \mathbf{0} \text{ in } \Omega \quad (5.13)$$

$$\boldsymbol{\sigma} = \mathbf{C} : (\boldsymbol{\varepsilon} - \boldsymbol{\varepsilon}_T) \quad (5.14)$$

where,  $\boldsymbol{\sigma}$  and  $\boldsymbol{\varepsilon}$  represent the second order stress and strain tensors respectively,  $\mathbf{q}$ ,  $k$ ,  $Q$  and  $\mathbf{b}$  are the heat flux, thermal conductivity, heat source and body force vector respectively, and  $\mathbf{C}$  is the fourth order elastic tensor.

$$\boldsymbol{\varepsilon} = \nabla_s \mathbf{u} \quad (5.15)$$

$$\boldsymbol{\varepsilon}_T = \alpha (T - T_{ref}) \mathbf{I} \quad (5.16)$$

The thermal and mechanical boundary conditions for the domain can be expressed in the following manner:

$$T = \bar{T} \text{ on } \Gamma_T \quad (5.17a)$$

$$\mathbf{q} \cdot \mathbf{n} = \bar{q} \text{ on } \Gamma_q \quad (5.17b)$$

$$\boldsymbol{\sigma} \cdot \mathbf{n} = \bar{\mathbf{t}} \text{ on } \Gamma_t \quad (5.17c)$$

$$\mathbf{u} = \bar{\mathbf{u}} \text{ on } \Gamma_u \quad (5.17d)$$

where the displacement and temperature field variables are denoted as  $\mathbf{u}$  and  $T$ , respectively. The thermal expansion coefficient is represented by  $\alpha$ . The operator  $\nabla_s$  refers to the symmetric gradient operator on a vector field, while  $\mathbf{I}$  denotes the second-order identity tensor. Within the domain  $\Omega$ , it is assumed that there exists a crack denoted by  $\Gamma_c$ . The following conditions are followed: for adiabatic crack  $\Gamma_c \subset \Gamma_q$ ,  $\bar{q} = 0$  on  $\Gamma_c$  and for isothermal crack  $\Gamma_c \subset \Gamma_T$ ,  $\bar{T} = \bar{T}_c$  on  $\Gamma_c$ .

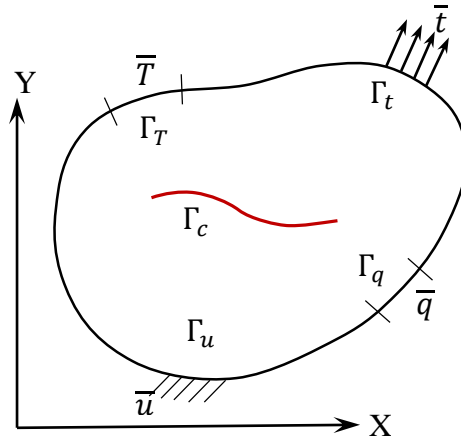


Figure 5.5: Two dimensional cracked domain with loading and boundary conditions.

### 5.3.1 Weak formulation for thermo-elastic loading

For an adiabatic crack scenario, the weak form of the governing **Eq. (5.11 & 5.13)** using the constitutive equation can be expressed as follows [166],

$$\int_{\Omega} \mathbf{q}(S) : \mathbf{k} \mathbf{q}(T) \, d\Omega + \int_{\Omega} S Q \, d\Omega - \int_{\Gamma_q} S \bar{q} \, d\Gamma - \delta W_T(T, W \nabla_s \lambda) = 0 \quad (5.18)$$

$$\int_{\Omega} \boldsymbol{\varepsilon}(\mathbf{u}) : \mathbf{C} : \boldsymbol{\varepsilon}(\mathbf{v}) \, d\Omega - \int_{\Omega} \mathbf{b} \cdot \mathbf{v} \, d\Omega - \int_{\Gamma_t} \bar{\mathbf{t}} \cdot \mathbf{v} \, d\Gamma - \int_{\Omega} \boldsymbol{\varepsilon}_T(\mathbf{u}) : \mathbf{C} : \boldsymbol{\varepsilon}(\mathbf{v}) \, d\Omega = 0 \quad (5.19)$$

Above equations are satisfied for  $\forall (S, \mathbf{v}) \in (T_0, u_0)$  where the subscript denotes homogeneous essential boundary conditions. The term  $\delta W_T(T, W \nabla_s \lambda)$  is due to the enforcement of the essential boundary condition by using the Lagrange multiplier. The thermal boundary conditions are imposed using Lagrange multiplier approach coupled

with FEM shape function. A set of discrete equation using temperature and nodal approximations, trial and test functions can be written as [97,167],

$$\begin{bmatrix} \mathbf{K}_{\text{thermal}} & \mathbf{G} \\ \mathbf{G}' & 0 \end{bmatrix} \begin{Bmatrix} \mathbf{T} \\ \boldsymbol{\lambda} \end{Bmatrix} = \begin{Bmatrix} \mathbf{f}_{\text{thermal}} \\ \mathbf{q}_{\text{thermal}} \end{Bmatrix} \quad (5.20)$$

$$[\mathbf{K}_{\text{elastic}}]\{\mathbf{u}\} = \{\mathbf{f}\} \quad (5.21)$$

where  $\mathbf{u}$  and  $\mathbf{T}$  are nodal displacement and temperature nodal unknowns, and  $\mathbf{K}$  and  $\mathbf{f}$  are the global stiffness matrix and external force vector respectively. Thermo-elastic fracture problems are dissociated into thermal and mechanical problems. First, the temperature distribution has been computed throughout the domain by solving the heat conduction discrete equations and structural field variables are computed using the temperature as input loading parameter.

Discrete set of equations from the weak form is given by

$$\mathbf{G}_{IJ} = - \int_{\Gamma_u} \phi_I \mathbf{N}_J \, d\Gamma \quad (5.22)$$

$$(\mathbf{q}_J)_{\text{thermal}} = - \int_{\Gamma_T} \mathbf{N}_J \bar{T} \, d\Gamma \quad (5.23)$$

$$\boldsymbol{\lambda}(s) = \mathbf{N}_J(s) \lambda_I \quad (5.24)$$

where  $\boldsymbol{\lambda}$  is Lagrange multiplier,  $\mathbf{N}_J(s)$  is Lagrange interpolant and  $s$  is the arc length along the boundary.

$$(\mathbf{K}_{ij}^e)_{\text{thermal}} = \int_{\Omega^e} (\mathbf{B}_i)_{\text{thermal}}^T \text{Cond} (\mathbf{B}_j)_{\text{thermal}} \, d\Omega \quad (5.25)$$

$$(\mathbf{K}_{ij}^e)_{\text{elastic}} = \int_{\Omega^e} (\mathbf{B}_i)_{\text{elastic}}^T \mathbf{C} (\mathbf{B}_j)_{\text{elastic}} \, d\Omega \quad (5.26)$$

$$(\mathbf{f}_i)_{\text{thermal}} = \int_{\Gamma_i} \mathbf{N}_i \mathbf{q} \, d\Gamma + \int_{\Omega^e} \mathbf{N}_i Q \, d\Omega \quad (5.27)$$

$$(\mathbf{f}_i)_{\text{elastic}} = \int_{\Gamma_i} \mathbf{N}_i \bar{\mathbf{t}} d\Gamma + \int_{\Omega^e} \mathbf{N}_i \mathbf{b} d\Omega \quad (5.28)$$

where  $\mathbf{N}_i$  is finite element shape function.

The thermal conductivity matrix ‘Cond’ for 2D isotropic materials is given by,

$$\text{Cond} = \begin{bmatrix} k & 0 \\ 0 & k \end{bmatrix} \quad (5.29)$$

The thermal and elastic stiffness matrix discussed in **Eq. (5.25)** and **Eq. (5.26)** respectively, can be calculated using **Eq. (5.10)**. In the case of an isothermal crack, the heat flux is discontinuous across the crack surface instead of the temperature field. The crack region is considered as part of  $\Gamma_T$ , where the minimum heat flux is introduced. On the other hand, for an adiabatic crack, the heat flux along the crack surface is set to zero, and the temperature field exhibits a discontinuity across the crack surface due to the insulation condition.

## 5.4 Thermal Cohesive Zone

As the crack appears in the material, the interfaces of the crack act as obstacles to the conduction of heat, causing changes in the evolving temperature distribution within the solid material. This phenomenon distinctly impacts the thermal stresses and has the potential to induce significant changes in the subsequent mechanical response. The fracture process zone near the tip of a crack in brittle materials is extremely small and can often be disregarded. However, the singularity remains present at the crack tip, which can be effectively addressed by incorporating the cohesive zone model. The implementation of cohesive zone in the SFNM framework is straightforward. By neglecting the heat source, the **Eq. (5.18)** can be modified to **Eq. (5.30)**, as given below.

$$\int_{\Omega} \mathbf{q}(S) k \mathbf{q}(T) d\Omega + \int_{\Gamma_c} S q_c d\Gamma - \int_{\Gamma_q} S \bar{q} d\Gamma - \delta W_T(T, W \nabla_s \lambda) = 0 \quad (5.30)$$

In a manner analogous to applying the mechanical cohesive law, the calculation of crack separation occurring at the interface within the cohesive zone is performed [168,169] as provided in the following formulation. This separation within the cohesive elements results from thermal stresses induced by the external application of heat.



$$\bar{\mathbf{u}}_L = \mathbf{R}\mathbf{u} \quad (5.31)$$

$$\bar{\Delta} = \mathbf{L}\bar{\mathbf{u}}_L \quad (5.32)$$

$$\Delta = \mathbf{N}\bar{\Delta} \quad (5.33)$$

where  $\mathbf{u}$  denotes the nodal displacements,  $\mathbf{N}$  is the shape function matrix,  $\bar{\mathbf{u}}_L$  is the local nodal displacements and  $\bar{\Delta}$  is the local displacement jump or local separation.  $\Delta$  denotes the separation along the cohesive surface element. The rotational matrix  $\mathbf{R}$  is given by,

$$\mathbf{R} = \begin{bmatrix} \Upsilon & 0 & 0 & 0 \\ 0 & \Upsilon & 0 & 0 \\ 0 & 0 & \Upsilon & 0 \\ 0 & 0 & 0 & \Upsilon \end{bmatrix} \quad (5.34)$$

where transformation matrix ( $\Upsilon$ ) is given as,

$$\Upsilon = \begin{bmatrix} \cos\theta & \sin\theta \\ -\sin\theta & \cos\theta \end{bmatrix} \quad (5.35)$$

Local separation is given in **Eq. (5.36)** which can be calculated with the help of the  $\mathbf{L}$  operator given in **Eq. (5.37)**. The  $\mathbf{L}$  operator is the local displacement-separation relation matrix.  $\mathbf{N}$  is the shape function matrix of 2 node linear elements given by **Eq. (5.38)**.

$$\bar{\Delta}_1 = \bar{u}_{L7} - \bar{u}_{L1}, \bar{\Delta}_2 = \bar{u}_{L8} - \bar{u}_{L2}, \bar{\Delta}_3 = \bar{u}_{L5} - \bar{u}_{L3}, \bar{\Delta}_4 = \bar{u}_{L6} - \bar{u}_{L4}. \quad (5.36)$$

$$\mathbf{L} = \begin{bmatrix} -1 & 0 & 0 & 0 & 0 & 0 & 1 & 0 \\ 0 & -1 & 0 & 0 & 0 & 0 & 0 & 1 \\ 0 & 0 & -1 & 0 & 1 & 0 & 0 & 0 \\ 0 & 0 & 0 & -1 & 0 & 1 & 0 & 0 \end{bmatrix} \quad (5.37)$$

$$\mathbf{N} = \begin{bmatrix} N_1 & 0 & N_2 & 0 \\ 0 & N_1 & 0 & N_2 \end{bmatrix} \quad (5.38)$$

Finally, the relation between global nodal displacement and the separation along the cohesive surface can be written in a form as given in **Eq. (5.39)**.

$$\Delta = \mathbf{B}_c \mathbf{u} \quad (5.39)$$

where  $\mathbf{B}_c = \mathbf{NRL}$ .

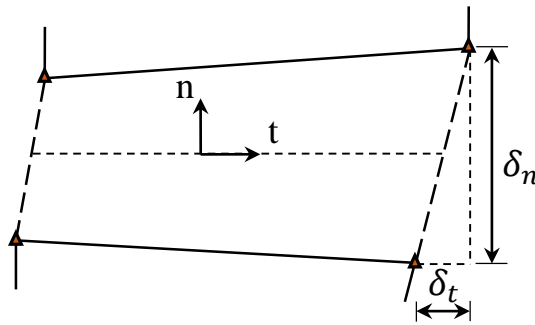


Figure 5.6: Cohesive zone crack interfaces separation with floating nodes along tangential and normal directions.

The parameter  $\Delta$  provides the tangential ( $\delta_t$ ) and normal ( $\delta_n$ ) separation and using this, the resultant separation of length  $\delta$  is calculated as shown in **Figure 5.6**. The heat flow via radiation within the partially damaged Fracture Process Zone (FPZ) is neglected in this model, while the heat conduction through the interconnected material patches is accounted by using Fourier's law. In thermal cohesive zone, it is assumed that the heat flux  $q_c$  through the cohesive crack can be determined by multiplying the cohesive conductance coefficient  $h_c$  by the temperature difference  $\Delta\theta_c$  across the cohesive crack [170].

$$q_c = h_c \Delta\theta_c \quad (5.40)$$

The temperature jump ( $\Delta\theta_c$ ) across the cohesive zone is calculated as the difference of the upper and lower nodal temperature. Using the linear cohesive law depicted in **Figure 5.7**, the cohesive conductance coefficient  $h_c$  that corresponds to this specific resultant separation  $\delta$  is established. Here,  $\delta_{max}$  represents the critical resultant separation within the thermal cohesive zone. The correlation between cohesive thermal conductance and the separation at the interface clarifies the decline in heat transfer within the cohesive zone. This critical resultant separation can be computed using either the materials parameters [168] or through the damage analysis [169,171]. Subsequently, employing **Eq. (5.40)**, the computation of the heat flux within the cohesive zone is determined.

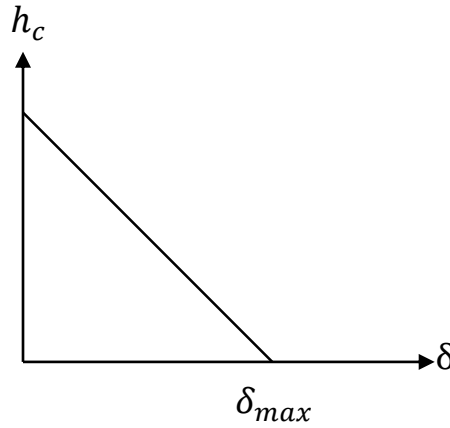


Figure 5.7: Normal separation law for heat transfer across a thermal cohesive crack.

## 5.5 SIF Computation and Crack Propagation Criterion

The interaction integral approach is used to determine the crack propagation. It applies to both homogeneous materials and bi-materials, involving the evaluation of interaction energy. Bi-material analysis requires considering additional factors due to different

mechanical properties of the materials involved. For a cracked body subjected to 2D deformation fields, the individual stress intensity factors ( $K_I$  and  $K_{II}$ ) are calculated using the domain form of interaction integral [77,82].

$$I^{(1,2)} = \int_A \left[ \boldsymbol{\sigma}_{ij}^{(1)} \frac{\partial u_i^{(2)}}{\partial x_1} + \boldsymbol{\sigma}_{ij}^{(2)} \frac{\partial u_i^{(1)}}{\partial x_1} - \mathbf{W}^{(1,2)} \delta_{1j} \right] \frac{\partial g}{\partial x_j} dA \quad (5.41)$$

In a similar way, thermal interaction integral can be defined as [172]

$$I^{(1,2)} = \int_A \left[ \boldsymbol{\sigma}_{ij}^{(1)} \frac{\partial u_i^{(2)}}{\partial x_1} + \boldsymbol{\sigma}_{ij}^{(2)} \frac{\partial u_i^{(1)}}{\partial x_1} - \mathbf{W}^{(1,2)} \delta_{1j} \right] \frac{\partial g}{\partial x_j} dA + \alpha \int_A \frac{\partial T}{\partial x_1} \boldsymbol{\sigma}_{kk}^{(2)} g dA \quad (5.42)$$

In this context,  $\mathbf{W}^{(1,2)}$  represents the interaction strain energy term related to the actual and auxiliary states,  $g$  denotes a smoothing weight function, and  $\boldsymbol{\sigma}_{ij}$  denotes the stress field. Here, 1 and 2 indicate the actual and auxiliary state, respectively. When considering a cracked body with a bi-material interface, the interaction integral form can be expressed as [138,173],

$$I^{(1,2)} = \sum_{m=1}^2 \int_{A_m} \left[ \boldsymbol{\sigma}_{ij}^{(1)} \frac{\partial u_i^{(2)}}{\partial x_1} + \boldsymbol{\sigma}_{ij}^{(2)} \frac{\partial u_i^{(1)}}{\partial x_1} - \mathbf{W}^{(1,2)} \delta_{1j} \right] \frac{\partial g}{\partial x_j} dA \quad (5.43)$$

where  $m$  represents a specific material in the bi-material domain. In a similar fashion, the thermal interaction integral for a crack along an interface in Bi-materials can be written as

$$I^{(1,2)} = \sum_{m=1}^2 \int_{A_m} \left[ \boldsymbol{\sigma}_{ij}^{(1)} \frac{\partial u_i^{(2)}}{\partial x_1} + \boldsymbol{\sigma}_{ij}^{(2)} \frac{\partial u_i^{(1)}}{\partial x_1} - \mathbf{W}^{(1,2)} \delta_{1j} \right] \frac{\partial g}{\partial x_j} dA + \sum_{m=1}^2 \alpha \int_{A_m} \frac{\partial T}{\partial x_1} \boldsymbol{\sigma}_{kk}^{(2)} g dA \quad (5.44)$$

The crack growth is simulated by introducing small linear increments to the crack tip in the updated model. The direction of crack propagation is determined using maximum circumferential stress criterion. Hence, the crack direction is determined for each increment using the following equation.

$$\theta_c = 2 \arctan \frac{1}{4} \left\{ \frac{K_I}{K_{II}} \pm \text{sign}(K_{II}) \sqrt{\left(\frac{K_I}{K_{II}}\right)^2 + 8} \right\} \quad (5.45)$$

Corresponding to this  $\theta_c$ , equivalent mode-I SIF is computed as,

$$\Delta K_{Ieq} = \Delta K_I \cos^3\left(\frac{\theta_c}{2}\right) - 3\Delta K_{II} \cos^2\left(\frac{\theta_c}{2}\right) \sin\left(\frac{\theta_c}{2}\right) \quad (5.46)$$

## 5.6 Numerical Results

Heat flux refers to the rate at which heat flows across a surface per unit area. It is analogous to the tractions that are exerted on a boundary. In the context of studying steady state heat conduction in a cracked specimen, researchers have solved a number of related problems. These problems include examining the behaviour of the crack under both isothermal and adiabatic thermo-elastic loading conditions, as well as investigating the mechanics of crack growth. In all of these scenarios, it is assumed that there is no heat source or external force acting on the specimen. In the present work, four thermal problems are examined under steady state thermo-elastic loading in order to validate the SFNM technique. First two thermal problems are pertaining to the static crack analysis while the other two deal with the crack propagation based on thermal SIF. The temperature distribution inside the domain is computed by enforcing the temperature boundary conditions. To impose the Dirichlet boundary conditions, Penalty method [174,175] in the framework of FEM and Lagrange multiplier [176] in framework of XFEM is available in the literature. Here, Lagrange multiplier is utilized in the framework of SFNM for all the thermal fracture problems. The obtained temperature is used as an input parameter to compute the forces for the elastic part. Finally, the domain is solved for the nodal deformations. The predefined crack regime is represented by the floating nodes as per the crack orientation. The elements and sub-elements are further divided into the cells for the boundary integration of each cell. The stress, strain data of the cell is transferred to the nodes as per their corresponding cell areas [177,178] for plotting purpose. The plane strain condition is utilized for simulating the problems.

### 5.6.1 Isothermal centre crack

Thermo-elastic analysis of a square plate with a horizontal centre crack subjected to pure opening mode (mode I) is studied in this section. The size of the square plate is

$2W$ , where  $W$  is taken equal to 100 mm. The study is carried out on the half-plate due to the symmetry of the problem. The right half specimen is considered for the analysis and the left edge is constrained in  $x$ -direction for the computation of displacement fields. The geometry and boundary conditions of the plate are illustrated in **Figure 5.8** taken from literature [166,179]. The specimen details are as follows: specimen size 100 mm  $\times$  200 mm, modulus of elasticity ( $E$ ) 218.4 GPa, thermal expansion coefficient  $1.67 \times 10^{-6} / ^\circ\text{C}$  and Poisson's ratio 0.3. The domain is discretized uniformly, and the analysis makes use of 50 nodes in  $x$ -direction and 100 nodes in  $y$ -direction. The boundary edges of the plate are subjected to temperatures of  $100^\circ\text{C}$  and  $0^\circ\text{C}$  at the crack.

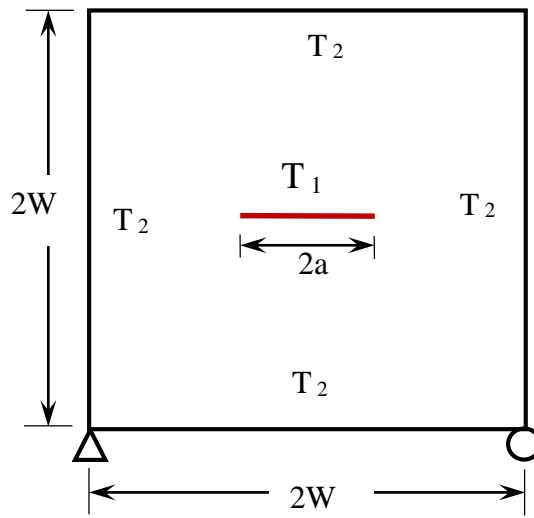


Figure 5.8: Geometry of homogeneous square plate with a centre crack under isothermal load.

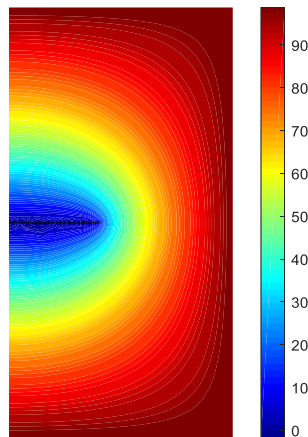


Figure 5.9: Temperature contour for a symmetrical half plate subjected to isothermal loads considering half of centre crack as an edge crack for  $a/W = 0.4$ .

The temperature distribution contour for symmetrical half plate is displayed in **Figure 5.9**. The distributed thermal load in the corresponding elements is utilized to compute the nodal deformation occurring in the specimen domain. The stress contours in different directions are plotted for the plane strain conditions in **Figure 5.10**. The thermal stress intensity factor (SIF) is computed using the interaction integral approach,

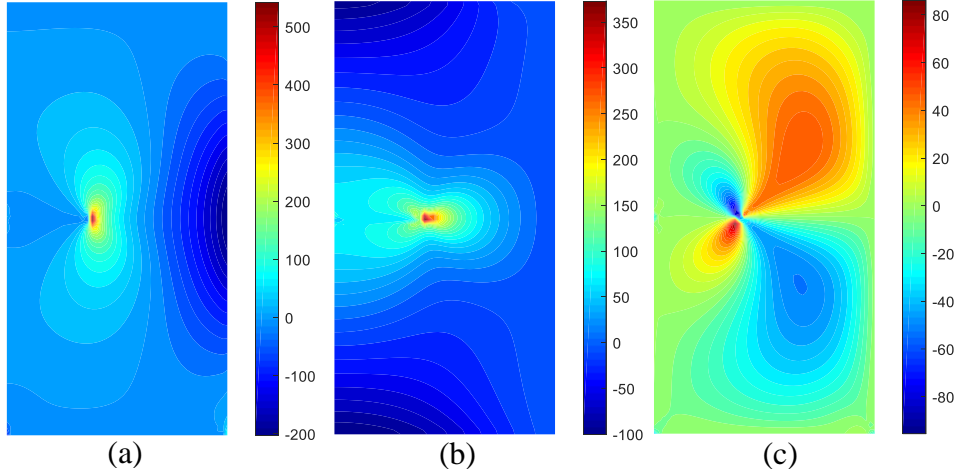


Figure 5.10: Stress contour plots for a symmetrical half plate subjected to isothermal loads considering half of centre crack as an edge crack. (a)  $\sigma_{yy}$ ; (b)  $\sigma_{xx}$ ; (c)  $\sigma_{xy}$ .

and path independency is verified. The convergence of SIF values is assessed at various numbers of nodes along the crack growth path as shown in **Figure 5.11**. Finally, it is normalized using  $E\alpha\Delta T\sqrt{W}$ , where  $\Delta T$  is the difference between the crack temperature and the applied temperature at the boundary. The SIF values are calculated at different crack values, primarily  $a/W$  varying from 0.1 to 0.6. The obtained results are plotted in

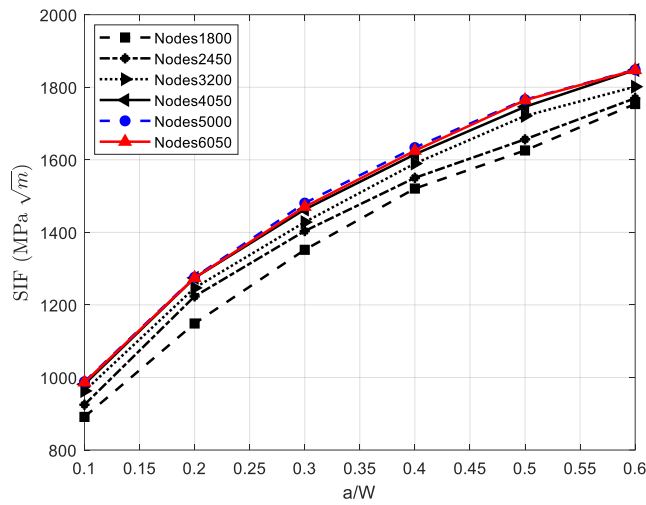


Figure 5.11: SIF Convergence analysis of the Isothermal centre crack in a square plate with varying of number of nodes.

**Figure 5.12** for comparison with the literature, where in literature [179] the extended meshfree method is used to analyse the thermo-elastic crack problem while [166] used the XFEM approach by enriching the thermal and mechanical fields. The results obtained in this study are in good agreement with the literature results.

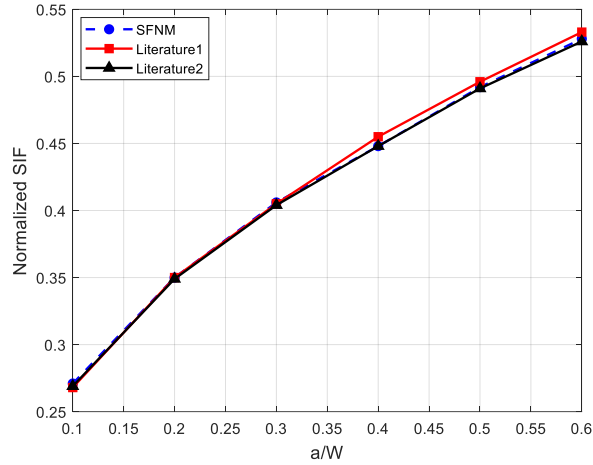


Figure 5.12: Normalized SIF comparison of the Isothermal centre crack in a square plate with Literature1 [166] and Literature2 [50].

### 5.6.2 Adiabatic centre crack

In this problem, a square specimen with a centre crack of size  $2a$  and dimensions of  $2W$  is examined, as demonstrated in **Figure 5.13**. The boundary conditions enforced in this instance cause pure sliding mode (mode II) to occur at the crack tip. Also, due to symmetry, the adiabatic simulation of the crack considers only half of the geometry.

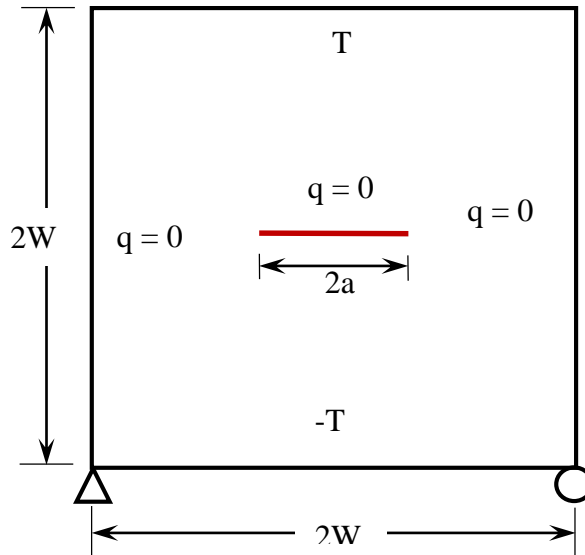


Figure 5.13: Geometry of homogeneous square plate with a centre crack under adiabatic thermal load.

The half specimen dimensions are  $100 \text{ mm} \times 200 \text{ mm}$ , with a modulus of elasticity of 218.4 GPa, a thermal expansion coefficient of  $1.67 \times 10^{-6} / ^\circ\text{C}$ , and a Poisson's ratio of 0.3. A uniformly distributed mesh of nodes  $50 \times 100$  in  $x$ - and  $y$ -direction respectively is utilized for the simulations. The temperature applied to the edges normal to the crack

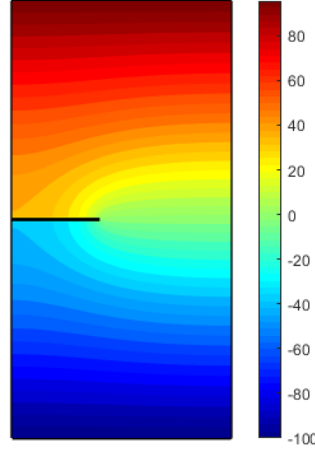


Figure 5.14: Temperature contour plot for a symmetrical half plate subjected to adiabatic thermal load considering half of centre crack as an edge crack for  $a/W = 0.4$ .

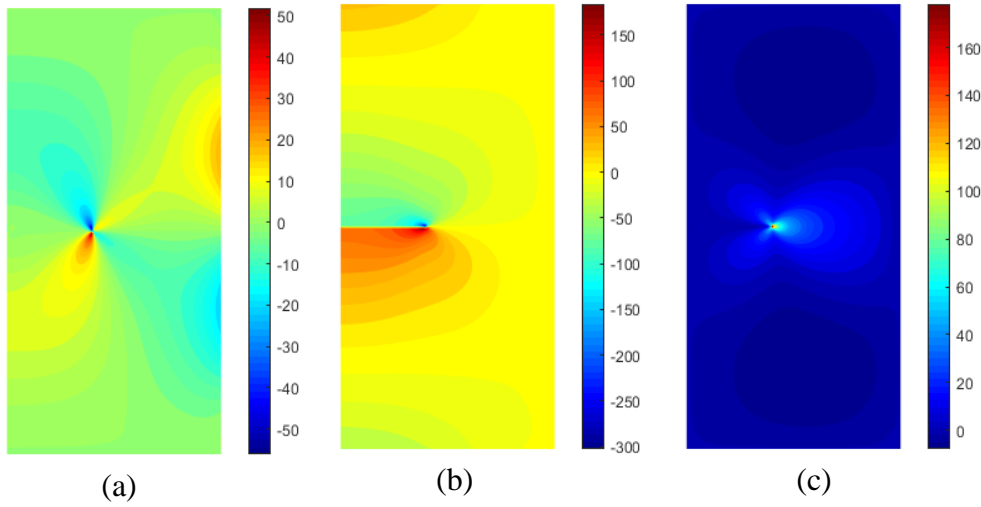


Figure 5.15: Stress contour plots for a symmetrical half plate subjected to adiabatic thermal loads considering half of centre crack as an edge crack. (a)  $\sigma_{yy}$ ; (b)  $\sigma_{xx}$ ; (c)  $\sigma_{xy}$ .

varies from  $-100^\circ\text{C}$  to  $100^\circ\text{C}$ , while the heat flux along the crack is of zero magnitude owing to insulation. Temperature and stress distribution contours for the specimen are plotted and displayed in **Figure 5.14** and **Figure 5.15** respectively corresponding to  $a/W = 0.4$ . The stress contours exhibited in the results closely align with the findings reported in the literature [179]. SIF values are calculated for the  $a/W$  varying from 0.1 to 0.6 in the step of 0.1 interval. The analysis findings of normalized SIFs are compared to



literature results and are presented in **Figure 5.16**. From the figure, it is observed that the SFNM provides results with good accuracy.

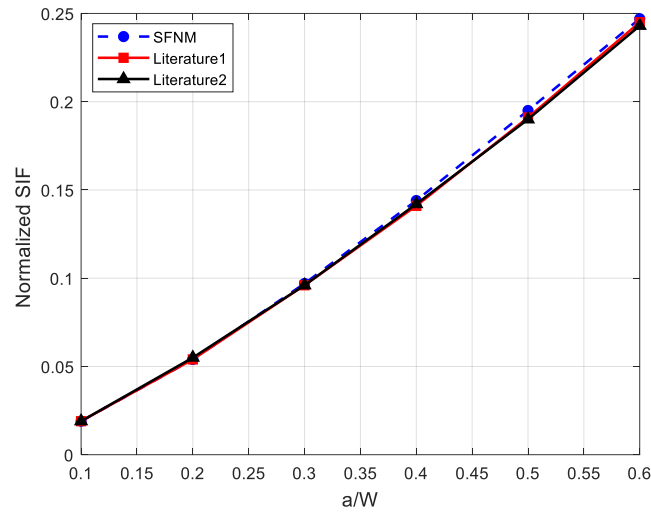


Figure 5.16: Normalized SIF comparison of the Adiabatic centre crack in a square plate with Literature1 [22] and Literature2 [50].

### 5.6.3 Adiabatic edge crack propagation

The problems described earlier dealt with the stationary crack that had a central position, while the current problem focuses on the implementation of SFNM for crack growth. The crack is allowed to expand until the material's fracture strength is reached. The adiabatic edge crack analysis involves a specimen size of 200 mm  $\times$  200 mm. **Figure 5.17** includes the geometry details and initial edge crack. The thermo-elastic properties

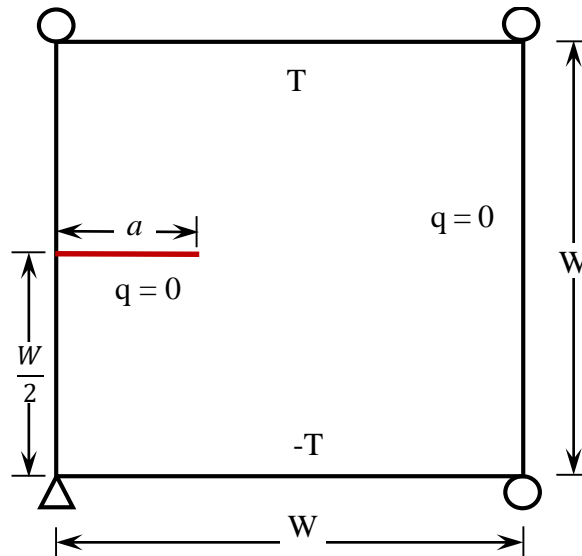


Figure 5.17: Square homogeneous plate with an edge crack under adiabatic thermal load.

considered for the present simulation are: modulus of elasticity  $E = 200$  GPa, thermal expansion coefficient  $\alpha = 15\text{e-}6$  / $^{\circ}\text{C}$  and Poisson's ratio  $\nu = 0.3$ . This example considers the following boundary conditions: a constant maximum cyclic heat flux applied perpendicular to the crack surface with temperatures varying from  $500^{\circ}\text{C}$  at the

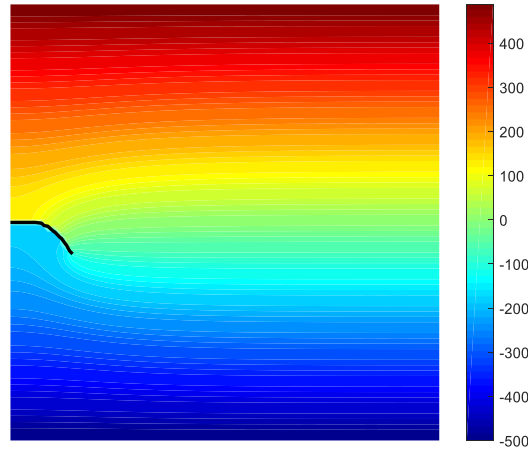


Figure 5.18: Temperature contour plot for homogeneous square plate with an edge crack under adiabatic thermal load.

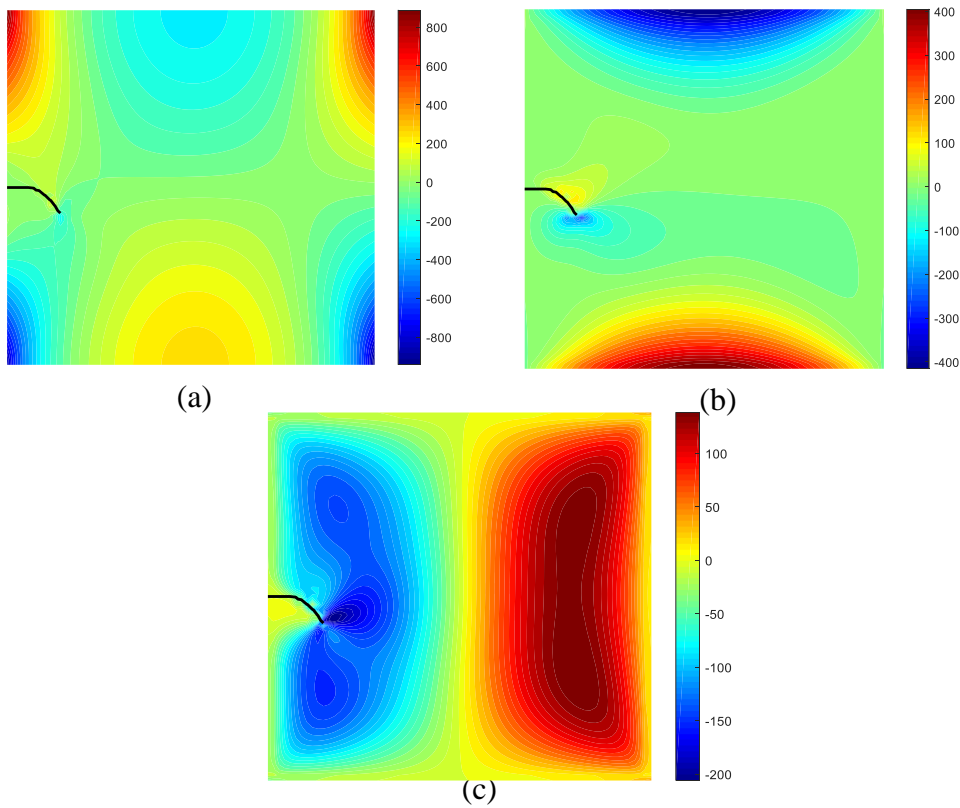


Figure 5.19: Stress contour plots for homogeneous square plate with an edge crack under adiabatic thermal load : (a)  $\sigma_{yy}$ ; (b)  $\sigma_{xx}$ ; (c)  $\tau_{xy}$ .

top edge to  $-500^{\circ}\text{C}$  at the bottom edge of the specimen. Deformation is limited in the  $y$ -direction at the boundaries that are normal to the pre-defined crack. The problem is sourced from [97], where it was numerically solved using the element-free Galerkin method. A minimum thermal load is applied at the crack surface, causing the temperature to drop to  $0^{\circ}\text{C}$ . The temperature and displacement fields are discontinuous across the crack surface. The temperature contour in the domain is displayed in the **Figure 5.18** for the critical crack length under adiabatic thermal loading conditions. Additionally, **Figure 5.19** illustrates the contour for normal and shear stress at the critical length of the crack. The crack increments suggest that the angle of propagation continuously increases and strives to incline vertically before reaching the critical stage. The SIF values are measured at various stages of crack growth, ranging from the initial crack length to the critical stage. A plot is generated to compare the SIF values against the corresponding crack lengths, and then compared with the XFEM results in **Figure 5.20**. The XFEM results incorporate the Heaviside step function for elements that are completely cut by the crack and asymptotic enrichment functions for elements at the crack tip that are only partially intersected.

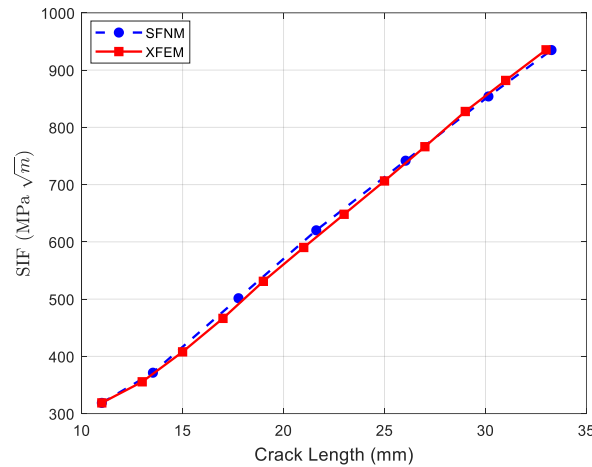


Figure 5.20: SIF vs crack length variation for edge crack of homogeneous square plate under adiabatic thermal load.

#### 5.6.4 Bi-material adiabatic interfacial crack propagation

A bi-material edge crack refers to a fracture that occurs specifically at the interface between two distinct materials with varying mechanical properties. To investigate this phenomenon, a square plate containing an edge crack located at the interface of two distinct materials is analysed, as shown in **Figure 5.21**. The specimen is characterized by the following material properties:  $E_1 = 200 \text{ GPa}$ ,  $\nu_1 = 0.3$ ,  $\alpha_1 = 15 \times 10^{-6} / ^{\circ}\text{C}$  for

material-1, and  $E_2 = 400$  GPa,  $\nu_2 = 0.25$ ,  $\alpha_2 = 8 \times 10^{-6} / ^\circ\text{C}$  for material-2. In this context,  $E$  represents the elastic modulus,  $\nu$  denotes the Poisson's ratio and  $\alpha$  symbolizes the thermal expansion coefficient. A maximum heat flux is applied perpendicular to the crack surface, while a zero heat flux is applied along the crack surface.

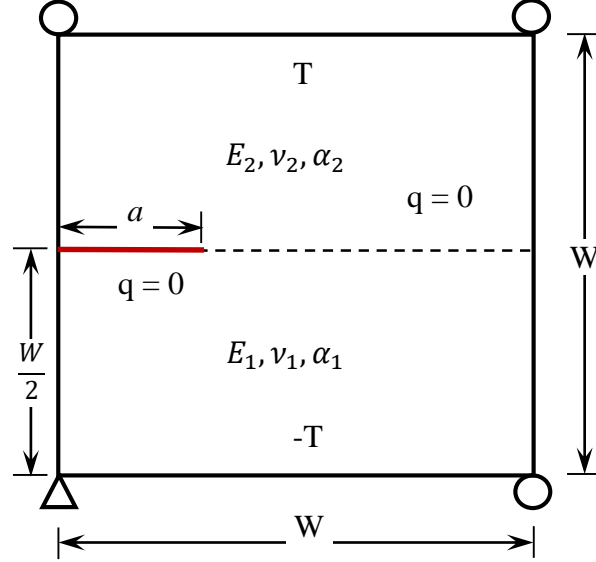


Figure 5.21: Bi-material plate with an edge crack under adiabatic thermal load.

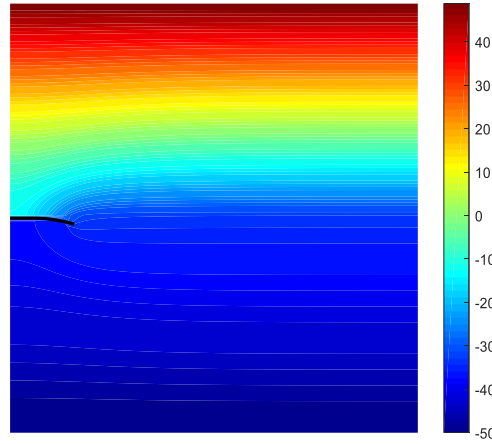


Figure 5.22: Temperature contour plot for bi-material plate with an edge crack under adiabatic thermal load.

The temperature is set to a maximum of 50 °C at the top edge and a minimum of -50 °C at the bottom edge. The resulting temperature profile and stress contours in the normal and shear-directions are plotted in **Figure 5.22** and **Figure 5.23** respectively, which confirms the findings reported in the study [97] using the EFGM method. It is observed that the edge crack deviates slightly towards the soft material side. Furthermore, the stress contour plot shows a continuous contour across the interface of

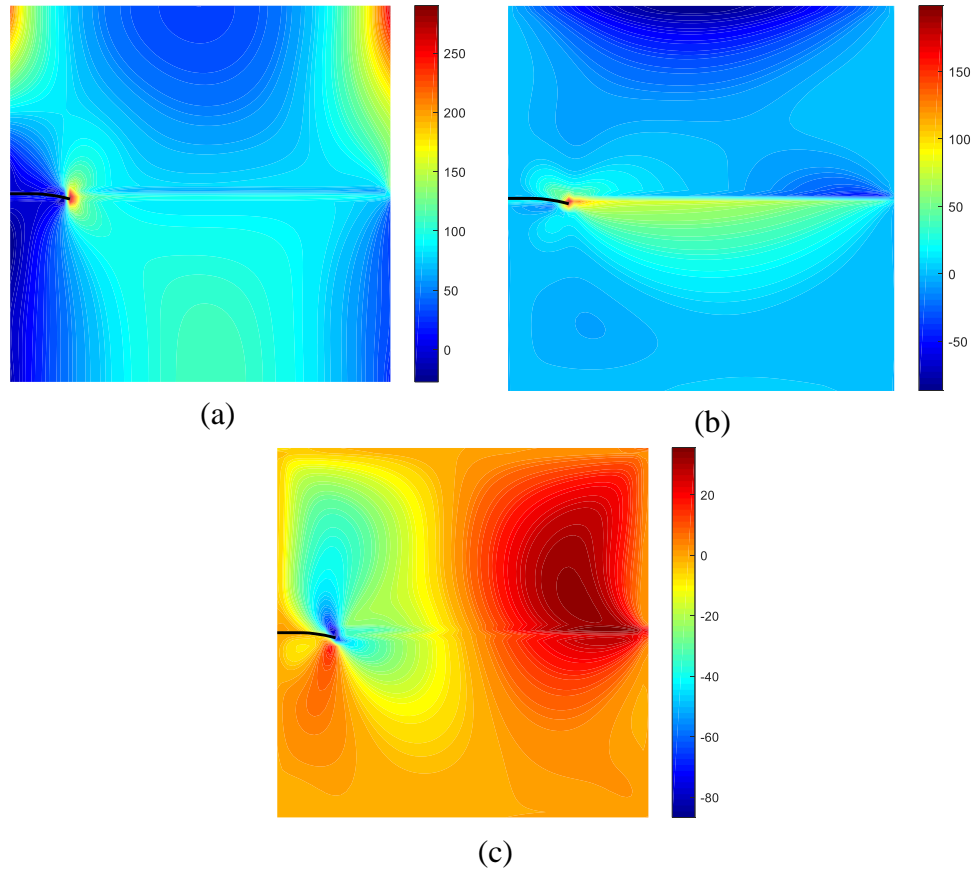


Figure 5.23: Stress contour plot for bi-material plate with an edge crack under adiabatic thermal load: (a)  $\sigma_{yy}$ ; (b)  $\sigma_{xx}$ ; (c)  $\tau_{xy}$ .

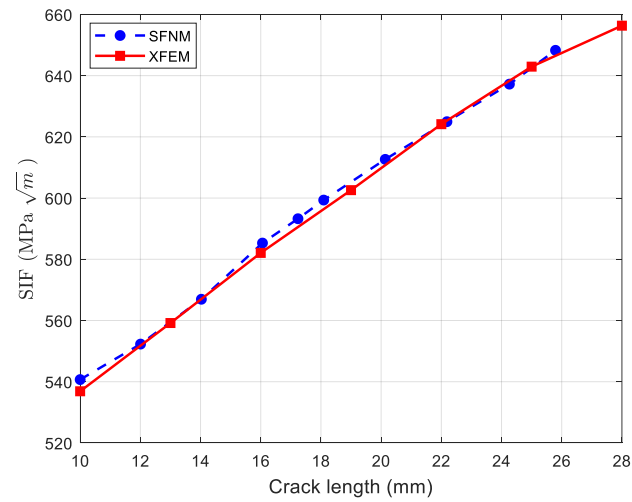


Figure 5.24: SIF variation with respect to crack length of an adiabatic edge crack of a bi-material plate.

the two materials. The stress intensity factor variation with respect to crack length is plotted in **Figure 5.24**, and compared with the XFEM results for verification.

## 5.7 Conclusions

This paper demonstrates the successful application of the smoothed floating node method with cohesive zone model to solve thermo-elastic fracture problems, encompassing both homogeneous and inhomogeneous materials considering isothermal and adiabatic thermal conditions. The method decouples thermo-elasticity problem into its thermal and elastic components, and temperature boundary conditions imposed through Lagrange multipliers which are then utilized to compute the displacements. The discontinuity of the displacement and heat flux are modelled in the framework of SFNM. The analysis includes determining temperature distributions and stress contours in static crack problems, with results compared to those in existing literature. The stress intensity factor is also verified for different lengths of the static crack. The SFNM method is further applied to edge crack problems, where the crack propagates up to fracture strength under steady-state thermal loading conditions. The proposed approach proves effective without the use of enrichment functions for discontinuity. Additionally, the inversion of the Jacobian used for isoparametric mapping is eliminated by using the line integration of the edges of the elements through smoothing procedure. The results demonstrate the effectiveness and capabilities of SFNM in solving thermo-elastic fracture problems with less complexity in implementation.

In this chapter, we model the steady-state heat conduction problem while considering mechanical constraints. However, it is also important to study problems that are exposed to both thermal and mechanical loads. After exploring into thermal loads, the subsequent chapter investigates the integration of thermo-mechanical loads.

# Thermo-mechanical Quasi-brittle Fracture

---

This chapter explores the fracture failure of quasi brittle materials subjected to thermo-mechanical loading conditions. The micro-cracks ahead of the crack tip possess the nonlinear nature of stress variations. The fracture process zone nonlinear behaviour is addressed by using the traction separation law. The intrinsic separation law is clubbed with the smoothed floating node method to assess the fracture behaviour of the crack. Domain based interaction integral is used to compute SIF by adding the thermal effect. To check the robustness of the method, a few problems of fracture mechanics are solved, and obtained results are compared with the literature.

## 6.1 Introduction

Quasi-brittle materials are substances that display a blend of both brittle and ductile qualities. Their defining characteristics involve a distinct shift from elastic to plastic behaviour, often accompanied by significant energy dissipation during the propagation of cracks. Notable examples of quasi-brittle materials encompass concrete, ceramics, rocks, and masonry etc. Thermo-mechanical crack analysis investigates the behaviour of cracks in quasi-brittle materials when subjected to both mechanical loading and temperature fluctuations. This analytical approach holds critical significance in examining the failure mechanisms of structures constructed from quasi-brittle materials operating in service environments prone to temperature-related stress. The mechanical attributes of quasi-brittle materials are susceptible to alteration by temperature variations. A prime illustration of this is the reduction in concrete's tensile strength and fracture toughness as the temperature rises. This phenomenon arises from the thermal expansion-induced formation of micro-cracks within the material, subsequently diminishing its structural integrity. Quasi-brittle materials contain an array of microstructural features, including pores, inclusions, and grain boundaries, each exerting a substantial influence on the process of crack propagation and coalescence. Hence, it is imperative to develop a more effective approach to examine the intricate attributes of engineering structures capable of withstanding the demands imposed by elevated temperatures and mechanical loading. To this end, the reference [\[180\]](#) explores

ceramics' thermal fracture mechanics with temperature-sensitive properties, confirming the persistence of the square-root singular field near the crack tip. It proceeds to calculate the steady thermal stress intensity factor for an edge-cracked strip. Numerical analysis has explored the steady-state, dynamically advancing crack in a heat-conducting elastic body with temperature-dependent cohesive zone properties [181]. Further, ref [182] describes thermo-mechanical analysis of laminates with delamination cracks under a temperature gradient using a cohesive zone model. A specific traction-separation law is presented, considering breakdown of load transfer mechanisms. Load transfer behaviour is linked to heat conduction across the delamination crack. A method for analysing thermo-mechanical coupling in composite structures with bridged cracks is described in ref [183]. It introduces a crack bridging law considering load and heat transfer breakdown as crack opening increases.

In the direction of solving thermo-mechanical fracture problems, linear elastic fracture mechanics (LEFM) has been the conventional method for predicting interface failure, but it has certain constraints related to the overall material response and the proportion of the fracture process zone relative to the crack's size. LEFM fails to provide an accurate representation of the stress distribution in the vicinity of the crack tip. To address these limitations, the cohesive zone concept is employed. This concept mitigates the singularity at the crack tip by incorporating a traction-opening law that accounts for the material's finite strength and the mechanisms of load transfer within the fracture process zone. Typically, the intricate details of the interface are not explicitly modeled, and the load transfer mechanisms are followed within cohesive zone constitutive relationships. This approach has proven effective in predicting interface failure across various boundary conditions. The FPZ, partially damaged zone, is where the coalescence of micro-cracks occurs. In this zone, the material that remains in contact without complete separation at the interface functions as a pathway for heat conduction from one side to the other. Similarly, stress is transferred through the partially bridged material at the interface. As the crack progresses, both stress and heat flux transfer through the FPZ diminish, aligning with the principles described in the traction-separation law. Several types of approaches are reported in the literature like damage based methods [184–186], phase field methods [42,47,187,188], meshfree methods [189], discontinuity approach [190] for modelling the failure behaviour of different materials under thermo-mechanical loading conditions.



This chapter is structured as outlined below: Section 6.2 elaborates on the numerical formulation in the context of both thermal and mechanical loading conditions. Section 6.3 investigates cohesive zone modelling. Section 6.4 details the description of the crack growth direction. Section 6.5 offers insights into numerical simulation problems. Finally, Section 6.6 presents the concluding remarks.

## 6.2 Numerical Formulation

Mechanical equilibrium equation can be written as

$$\nabla \cdot \boldsymbol{\sigma} + \mathbf{b} = \mathbf{0} \text{ in } \Omega \quad (6.1)$$

where  $\sigma$  is the Cauchy stress tensor and  $\mathbf{b}$  is the body force vector.

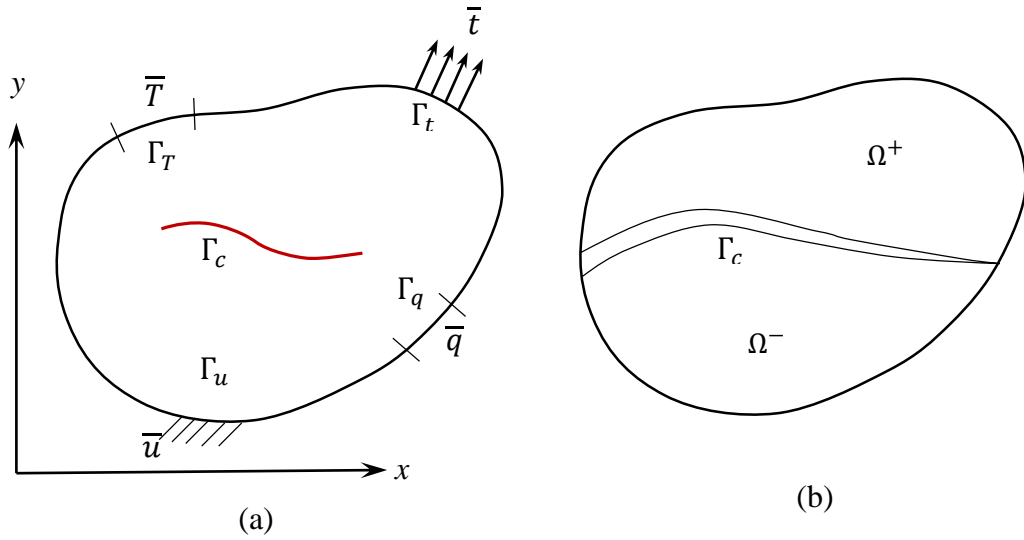


Figure 6.1: (a) Two dimensional cracked domain with loading and boundary conditions, (b) domain division as per discontinuity interface.

Similarly, in the absence of the internal heat source, the thermal equilibrium equation can be written as

$$\nabla \cdot \mathbf{q} + \rho c_v \dot{\theta} = 0 \quad (6.2)$$

$$\text{and } \mathbf{q} = -k \nabla T \quad (6.3)$$

Where  $\rho$  is the density,  $c_v$  is the heat capacity of the material and  $\mathbf{q}$  is the heat flux vector.

$$\boldsymbol{\sigma} = \mathbf{C} : (\boldsymbol{\varepsilon} - \boldsymbol{\varepsilon}_T) \quad (6.4)$$

$$\boldsymbol{\varepsilon}_T = \alpha (T - T_{ref}) \mathbf{I} \quad (6.5)$$

The thermal expansion coefficient is denoted by  $\alpha$ .  $\mathbf{I}$  represents the second-order identity tensor.

Along the cohesive crack the following continuity equations should be satisfied.  $t_c^+ = t_c^-$  and  $q_c^+ = q_c^-$ . The superscripts '+' and '-' represents the +ve and -ve side of the crack interface. The strong form of mechanical equilibrium equation in the absence of body force along with boundary conditions are given by **Eq. (6.6)**. Also **Eq. (6.6)** shows the thermal equilibrium equation with boundary conditions under steady state heat conduction flow [170].

Mechanical Domain	Thermal Domain	
$\nabla \cdot \boldsymbol{\sigma}^{+/-} = 0$ in $\Omega^{+/-}$	$\nabla \cdot \mathbf{q}^{+/-} = 0$ in $\Omega^{+/-}$	(6.6)
$\boldsymbol{\sigma}^{+/-} \cdot \mathbf{n}^{+/-} = \bar{\mathbf{t}}^{+/-}$ on $\Gamma_t^{+/-}$	$\mathbf{q}^{+/-} \cdot \mathbf{n}^{+/-} = \bar{q}^{+/-}$ on $\Gamma_q^{+/-}$	
$\mathbf{u}^{+/-} = \bar{\mathbf{u}}^{+/-}$ on $\Gamma_u^{+/-}$	$\boldsymbol{\theta}^{+/-} = \bar{\boldsymbol{\theta}}^{+/-}$ on $\Gamma_\theta^{+/-}$	
$t_c^{+/-} = \boldsymbol{\sigma}^{+/-} \cdot \mathbf{n}^{+/-}$ on $\Gamma_c^{+/-}$	$q_c^{+/-} = \mathbf{q}^{+/-} \cdot \mathbf{n}^{+/-}$ on $\Gamma_c^{+/-}$	

### 6.2.1 Weak formulation of equilibrium equations

For an adiabatic crack scenario, the weak form of the governing **Eq. (6.6)** using the constitutive equation can be expressed as follows [166],

$$\int_{\Omega} \rho c_v \dot{\theta} \delta \theta \, d\Omega + \int_{\Omega} \mathbf{q} \cdot \nabla \delta \theta \, d\Omega = \int_{\Gamma_q} \bar{q} \delta \theta \, d\Gamma + \int_{q_c} q_c (\delta \theta^+ - \delta \theta^-) \, d\Gamma \quad (6.7)$$

$$\int_{\Omega} \boldsymbol{\sigma} : \nabla \delta \mathbf{u} \, d\Omega = \int_{\Omega} \mathbf{b} \cdot \delta \mathbf{u} \, d\Omega + \int_{\Gamma_t} \bar{\mathbf{t}} \cdot \delta \mathbf{u} \, d\Gamma + \int_{\Gamma_c} t_c (\delta \mathbf{u}^+ - \delta \mathbf{u}^-) \, d\Gamma \quad (6.8)$$

The thermal boundary conditions are imposed using Lagrange multiplier approach coupled with FEM shape function. A set of discrete equation using temperature and nodal approximations, trial and test functions can be written as [167],

$$\begin{bmatrix} \mathbf{K}_{\text{thermal}} & \mathbf{G} \\ \mathbf{G}' & 0 \end{bmatrix} \begin{Bmatrix} \mathbf{T} \\ \boldsymbol{\lambda} \end{Bmatrix} = \begin{Bmatrix} \mathbf{f}_{\text{thermal}} \\ \mathbf{q}_{\text{thermal}} \end{Bmatrix} \quad (6.9)$$

$$[\mathbf{K}_{\text{elastic}}] \{\mathbf{u}\} = \{\mathbf{f}\} \quad (6.10)$$

where  $\mathbf{u}$  and  $\mathbf{T}$  are nodal displacement and temperature nodal unknowns, and  $\mathbf{K}$  and  $\mathbf{f}$  are the global stiffness matrix and external force vector respectively. Thermo-elastic fracture problems are dissociated into thermal and mechanical problems. First, the temperature distribution has been computed throughout the domain by solving the heat conduction discrete equations and therefore, the structural field variables are computed using the temperature as input loading parameter.

The discrete set of equations from the weak form is given by

$$\mathbf{G}_{IJ} = - \int_{\Gamma_u} \phi_I \mathbf{N}_J \, d\Gamma \quad (6.11)$$

$$(\mathbf{q}_J)_{\text{thermal}} = - \int_{\Gamma_T} \mathbf{N}_J \bar{T} \, d\Gamma \quad (6.12)$$

$$\lambda(s) = \mathbf{N}_J(s) \lambda_I \quad (6.13)$$

where  $\lambda$  is Lagrange multiplier,  $\mathbf{N}_J(s)$  is Lagrange interpolant and  $s$  is the arc length along the boundary. The stiffness matrices and force vectors given in Eq. 6.9 & Eq. 6.10 are defined as,

$$(\mathbf{K}_{ij}^e)_{\text{thermal}} = \int_{\Omega^e} (\mathbf{B}_i)_{\text{thermal}}^T \text{Cond} (\mathbf{B}_j)_{\text{thermal}} d\Omega \quad (6.14)$$

$$(\mathbf{K}_{ij}^e)_{\text{elastic}} = \int_{\Omega^e} (\mathbf{B}_i)_{\text{elastic}}^T \mathbf{C} (\mathbf{B}_j)_{\text{elastic}} d\Omega \quad (6.15)$$

$$(\mathbf{f}_i)_{\text{thermal}} = \int_{\Gamma_i} \mathbf{N}_i \mathbf{q} \, d\Gamma + \int_{\Omega^e} \mathbf{N}_i Q \, d\Omega \quad (6.16)$$

$$(\mathbf{f}_i)_{\text{elastic}} = \int_{\Gamma_i} \mathbf{N}_i \bar{\mathbf{t}} \, d\Gamma + \int_{\Omega^e} \mathbf{N}_i \mathbf{b} \, d\Omega \quad (6.17)$$

where  $\mathbf{N}_i$  is finite element shape function.

The thermal conductivity matrix ‘Cond’ for 2D isotropic materials is given by,

$$\text{Cond} = \begin{bmatrix} k & 0 \\ 0 & k \end{bmatrix} \quad (6.18)$$

In the case of an isothermal crack, the heat flux is discontinuous across the crack surface instead of the temperature field. The crack region is considered as part of  $\Gamma_T$ , where the minimum heat flux is introduced. On the other hand, for an adiabatic crack, the heat flux along the crack surface is set to zero, and the temperature field exhibits a discontinuity across the crack surface due to the insulation condition.

### 6.3 Cohesive Crack Modelling

In a uniaxial case, it's clear that traction should match the strength. However, in a mixed mode formulation, traction can be equivalent to the normal strength without shear traction, the shear strength without normal traction, or a combination of the two. The cohesive law utilized in this context is potential function based and valid for mode I, mode II, and a combination of both. It is integrated with the proposed method. The potential function ( $\Psi$ ) depends on the fracture energies and separation variables in normal and tangential directions, and is given as [156],

$$\begin{aligned} \Psi(\Delta_n, \Delta_t) = & \min(\phi_n, \phi_t) \\ & + \left[ \Gamma_n \left( 1 - \frac{\Delta_n}{\delta_n} \right)^\alpha \left( \frac{m}{\alpha} + \frac{\Delta_n}{\delta_n} \right)^m \right. \\ & \left. + \langle \phi_n - \phi_t \rangle \right] \left[ \Gamma_t \left( 1 - \frac{|\Delta_t|}{\delta_t} \right)^\beta \left( \frac{n}{\beta} + |\Delta_t| \delta_t \right)^n + \langle \phi_t - \phi_n \rangle \right] \end{aligned} \quad (6.19)$$

where  $\langle . \rangle$  is the Macauley bracket.  $\phi_n, \Gamma_n, \delta_n, \Delta_n$  represent the fracture energy, energy constant, crack opening width and separation at crack interface respectively, in the normal direction. The same variables with subscripts 't' means the variables in the tangential direction. Exponents  $m$  and  $n$  are associated with the initial slope, whereas  $\alpha, \beta$  act as shape parameters constants. The first derivative of the PPR potential provides cohesive tractions under the softening region.

$$\mathbf{t}_c(\Delta_n, \Delta_t) = \begin{Bmatrix} \partial \Psi / \partial \Delta_t \\ \partial \Psi / \partial \Delta_n \end{Bmatrix} = \begin{Bmatrix} T_t(\Delta_n, \Delta_t) \\ T_n(\Delta_n, \Delta_t) \end{Bmatrix} \quad (6.20)$$

The second derivative of the PPR potential results in the tangent stiffness matrix,

$$D_c(\Delta_n, \Delta_t) = \begin{bmatrix} D_{tt} & D_{tn} \\ D_{nt} & D_{nn} \end{bmatrix} = \begin{bmatrix} \partial^2 \Psi / \partial \Delta_t^2 & \partial^2 \Psi / \partial \Delta_t \partial \Delta_n \\ \partial^2 \Psi / \partial \Delta_n \partial \Delta_t & \partial^2 \Psi / \partial \Delta_n^2 \end{bmatrix} \quad (6.21)$$

These equations pertain to the cohesive crack within the fracture process zone and are integrated with the SFNM approach. For a thorough understanding and application of the cohesive zone model, one can refer to the details provided in the Chapter-4.

$$q_c = h_c \Delta \theta_c \quad (6.22)$$

The temperature jump ( $\Delta \theta_c$ ) across the cohesive zone is calculated as the difference of the upper and lower nodal temperature. Using the linear thermal cohesive law, the cohesive conductance coefficient  $h_c$  that corresponds to cohesive element separation is computed using the **Eq.(6.22)**. The detailed thermal part of the cohesive zone is presented in chapter-5.

## 6.4 Adiabatic edge crack propagation

The analysis of the specimen focuses on an adiabatic crack, with boundary conditions applied accordingly. The direction of crack propagation, under thermo-mechanical boundary conditions, is determined using the maximum principal stress theory. Crack increments are introduced at the fictitious crack tip once the fracture process zone achieves complete stress relaxation.

## 6.5 Numerical Simulations

The fracture problems are solved under the mechanical and the steady state heat conduction loading conditions. The problems are solved for the crack path and stress contour and temperature distribution. The principle of heat conduction, often referred to as Fourier's law, is applied in order to model the temperature distribution within the domain. The plane strain condition is utilized for simulating the problems. The detailed implementation of crack growth criterion and direction calculation is provided in Section 4.4 of Chapter-4.

### 6.5.1 Cruciform Specimen

A cruciform plate is investigated under the different loading conditions taken from ref. Firstly, it is analysed under the pure mechanical loading and then under pure thermal loading conditions. Finally, the specimen is checked under the combined effect of the thermal and mechanical loading conditions. The cruciform geometry along with boundary conditions is shown in **Figure 6.2**. An initial crack of size  $a = 0.2L$  oriented

at an angle of  $45^\circ$  counter clockwise to the horizontal direction. The material properties used for the specimen are given in **Table 6.1**. Here, the length designated as  $L$ , with a specified value of  $L=100$  mm is taken for the fracture analysis with a mesh size of 5 mm.

Table 6.1: Material properties and parameters for cruciform plate

Property Name/Parameters	Symbol	Value	Unit
Young's modulus	$E$	218400	Pa
Poisson's ratio	$\nu$	0.3	-
Fracture energy	$G_f$	$2e-4$	N/m
Tensile strength	$f_t$	120	N/m <sup>2</sup>
Thermal expansion coefficient	$\alpha$	$0.167e-5$	$^\circ\text{C}^{-1}$

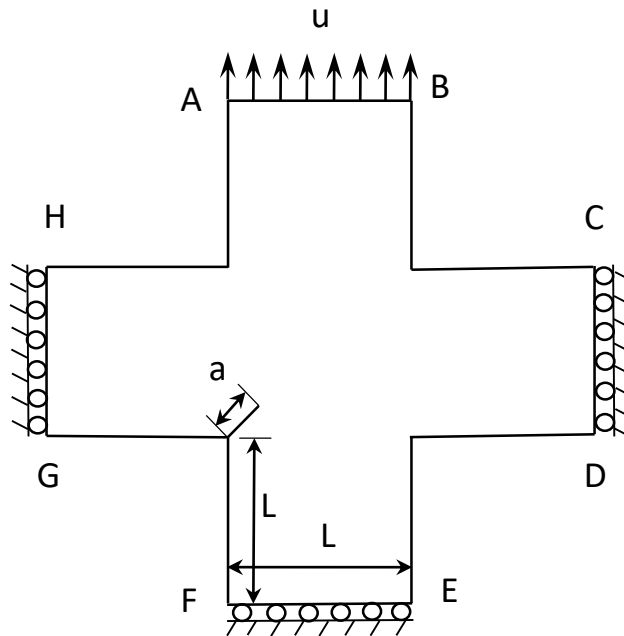


Figure 6.2: Cruciform Plate geometry with boundary conditions

Three types of cruciform cases are discussed with the SFNM formulation. The detail is provided in **Table 6.2**.

Table 6.2: Different cases of thermo-mechanical loading conditions.

Case	Temperature ( $^\circ\text{C}$ )				Displacement (mm)
	AB	CD	EF	GH	AB
1. Pure Mechanical	0	0	0	0	0.4
2. Pure Thermal	10	0	-10	0	0
3. Thermo-Mechanical	10	0	-10	0	0.4

### 6.5.1.1 Cruciform Specimen (Case-I: Pure Mechanical)

First case is the pure mechanical case in which left and right edges are constrained in the  $x$ -direction while the bottom edge is constrained in the  $y$ -direction as shown in **Figure 6.2**. The top edge is elongated using displacement controlled method. Initial crack with boundary conditions is subjected to minimum load and the conditions for the crack propagation is checked without using any cohesive zone model as the initial crack condition provides the stress free condition. Once the crack propagation criterion is fulfilled, the cohesive zone is inserted in the fracture process zone lumped as a straight crack length at the orientation computed from the crack growth criteria.

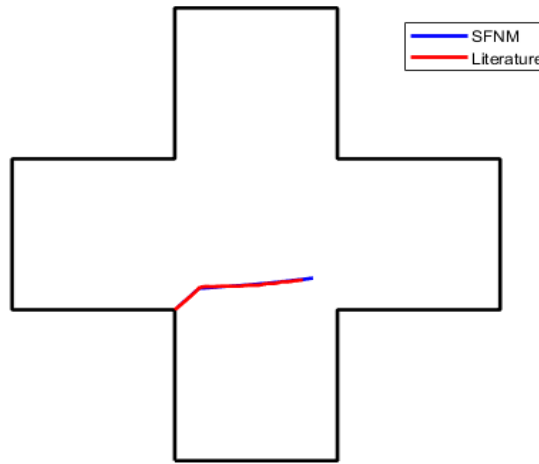


Figure 6.3: Cruciform plate crack path under pure mechanical loading conditions (Literature [170]).



Figure 6.4: Cruciform plate displacement contour (displacement in m) under pure mechanical loading conditions.

Using the first case of the problem, the crack path is traced by using the intrinsic potential based cohesive law applied to the fracture process zone and compared with the literature results. The crack path direction as shown in **Figure 6.3** can be seen as perpendicular to the applied load i.e. along horizontal direction. The nodal displacement contour plot is shown in **Figure 6.4**. Further the normal and shear stresses are computed and stress distribution in the y-direction is shown in the **Figure 6.5**. Constitutive relation of the nonlinear cohesive zone follows a dropping nature of stress with the increase in the crack opening. This softening behaviour can be seen in the structural response in the form of load displacement curve as shown in **Figure 6.6**. Finally, the deformed shape of the cruciform plate at an arbitrary state is shown in **Figure 6.7**.

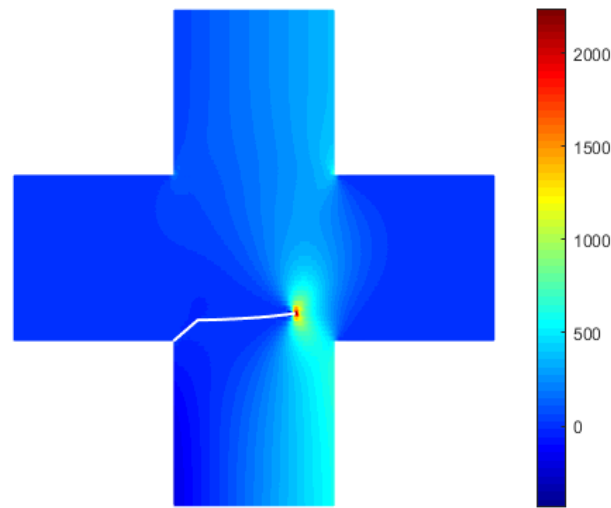


Figure 6.5: Cruciform plate stress ( $\text{N/m}^2$ ) contour in y-direction under pure mechanical case.

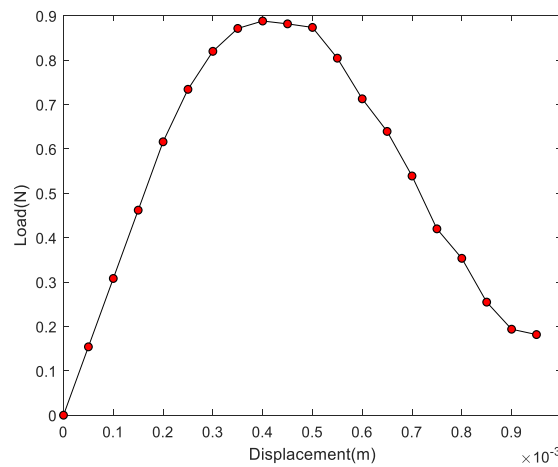


Figure 6.6: Structural Response of the cruciform plate



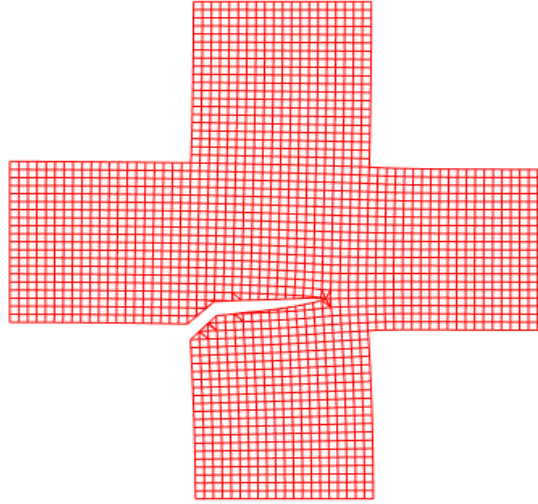


Figure 6.7: Deformed Shape under mechanical loading conditions.

#### 6.5.1.2 Cruciform Specimen (Case-II: Pure Thermal)

The second case of the cruciform plate follows the loading condition as given in **Table 6.2**. In this case no mechanical load is applied, only thermal load at top and bottom edges are applied and the specimen boundary conditions remain the same. First of all, the temperature distribution is calculated using the Lagrange multiplier and the induced thermal stresses are used to check the crack propagation path. The results of crack path calculated and of literature are compared as shown in the **Figure 6.8**. Corresponding to the crack growth path the temperature distribution is displayed in **Figure 6.9**.

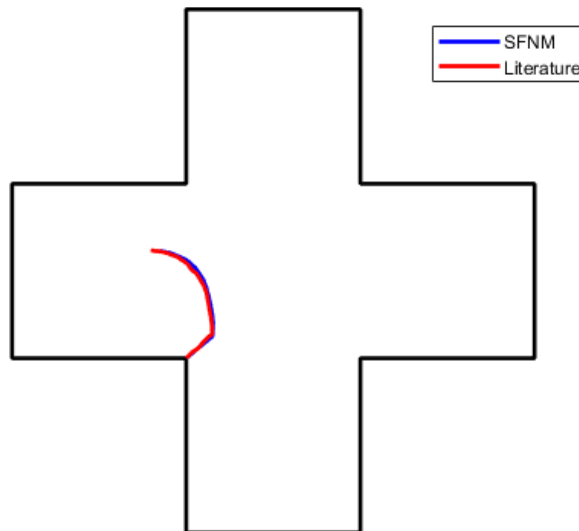


Figure 6.8: Crack path comparison under pure thermal loading conditions (Literature [170]).

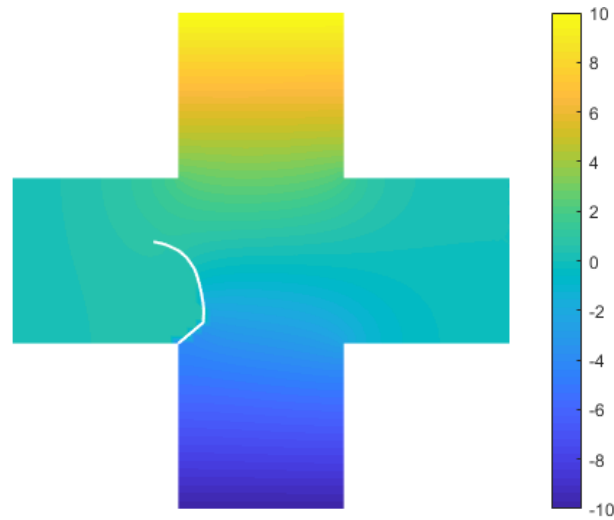


Figure 6.9: Temperature distribution profile under pure thermal loading conditions.

#### 6.5.1.3 Cruciform Specimen (Case-III: Thermo-Mechanical)

Third case deals with the combination of the mechanical and thermal loads keeping the constraints same. Here also the crack trajectory is obtained and compared with the literature as shown in **Figure 6.10**. The combination of two loads effects can be seen in the crack path compared to the individual one. The stresses are computed including the thermal stresses effects and the stress contour plot is shown in **Figure 6.11**.

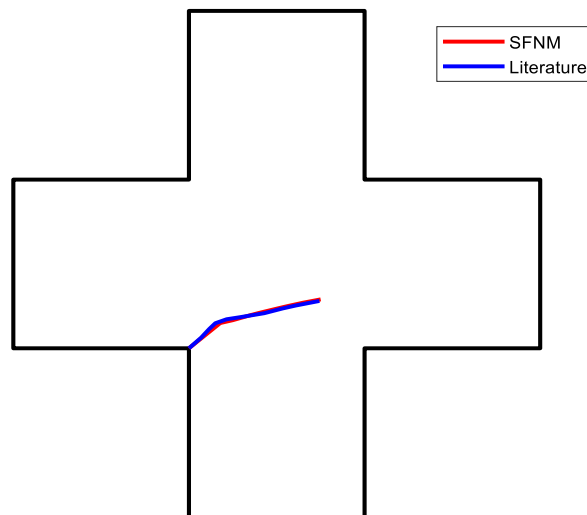


Figure 6.10: Crack path comparison under thermo-mechanical loading conditions (Literature [170]).

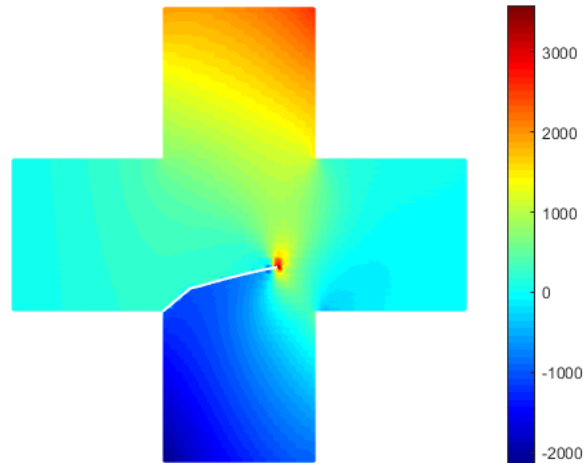


Figure 6.11: Stress Contour profile under thermo-mechanical loading conditions.

## 6.6 Conclusions

This chapter demonstrates the successful application of the smoothed floating node method with CZM to solve fracture problems subjected to thermo-mechanical loading conditions. The method utilises the SFNM feature to represent the discontinuity without the requirement of remeshing as in case of FEM and special enrichment functions in advanced methods i.e. XFEM etc. The numerical framework effectively implements the induced thermal stresses from the thermal boundary conditions. The results obtained through proposed framework are in good agreement with the results of literature. The application of a mechanical load in the y-direction causes the crack to extend in a direction perpendicular to the applied force. When thermal loads are applied at the top and bottom, the crack's propagation shifts towards the direction of the thermal load. Ultimately, the direction of crack growth becomes a result of the combined influence of both the applied mechanical load and the thermal load, dependent on the magnitude of each individual load as clearly demonstrated in the third case.

Left Blank Intentionally

### Conclusions and Future Scope

---

This chapter examines various findings extracted from the preceding chapters of the thesis. It highlights key conclusions derived from the analysis of mechanical and thermal loads under varying boundary conditions. The research primarily focuses on brittle and quasi-brittle materials. Moreover, considering the effectiveness of the suggested approach, potential opportunities for implementing the proposed method in fracture analysis across various applications have been suggested.

#### 7.1 Conclusions

The thesis investigates the advanced approaches in fracture mechanics to model the strong discontinuity in the structures. A novel approach, called smoothed floating node method, is developed that uses the floating nodes to model the crack in the domain and strain smoothing concept for the numerical integration. The proposed method effectively addresses the challenges of conformal meshing, remeshing, element distortion and singularity problems.

In elements where a crack emerges, previously dormant floating nodes become active. These activated floating nodes directly engage at the actual crack location and address the discontinuity. Further, the smoothing approach is also incorporated, wherein the element is partitioned into smooth cells, and integration is carried out along the edges of each cell. The results from these cells are combined to ascertain the behaviour of the element. Implementing line integration along the edges of the cell elevates both accuracy and convergence rate, as explained in Chapter-3. An isoparametric study and Jacobian calculations impose constraints on the choice of element and the nature of the study, whether it involves small or large deformation problems. Furthermore, it mandates that the element be convex in shape during the numerical simulations. These concerns have been tackled in the research work by incorporating the SFNM.

Based on this thesis work, the following key observations and conclusions have been made:

- A refined numerical framework for 2D linear elastic problems, known as the Smoothed Floating Node Method (SFNM), has been developed. This framework features explicit

shape function computation, eliminating the need for field variable gradient matrix derivatives and adhering to the properties of the Kronecker delta.

- SFNM's convergence rate has been assessed under both mode I and mode II loading conditions, revealing superior performance compared to the Floating Node Method. This framework is highly adaptable and can be applied to triangular, quadrilateral, or distorted elements.
- No remeshing or enrichment functions are required to model static crack and crack propagation behaviour.
- Issues related to artifacts at element edges near the crack tip in the FNM have been resolved by employing a single common float node instead of two separate nodes for adjacent elements.
- A cell-based smoothening approach has been adopted for integrating sub-elements and standard elements. An optimized approach includes four cells per quadrilateral element and a single cell for triangular elements for numerical integration.
- Stress and strain computations directly utilize cell area instead of weight and integration points, resembling reduced integration for quadrature integration.
- The method's insensitivity to element distortion, due to the absence of isoparametric mapping, eliminates the need for the inverse of Jacobian during integration, ensuring robustness in practical applications.
- SFNM has been combined with a cohesive zone approach to model crack growth behaviour in quasi-brittle materials. An intrinsic cohesive zone model based on potential is implemented to capture nonlinear fracture behaviour, including contact conditions, softening regions, and complete failure.
- Implementing nonlinear cohesive zone behaviour in SFNM is straightforward and adaptable for both homogeneous and nonhomogeneous materials using real positioned floating nodes.
- The effectiveness and robustness of SFNM are confirmed through the utilization of a single cohesive element in the patch test for both mode I and mode II analyses. This validation is then extended to address standard fracture problems.
- SFNM has successfully handled a variety of scenarios based on segment-based crack propagation. This includes straight and curved cracks positioned along edges, diagonally, and at different angles within elements.

- The research work illustrates the utilization of SFNM in addressing thermo-elastic fracture challenges in brittle materials, highlighting its versatility in managing diverse thermal loading and boundary conditions along with thermal cohesive modelling.
- In the domain of thermo-mechanical fracture simulations, the SFNM approach demonstrates its compatibility and effectiveness under various mechanical and thermal loading conditions.

## 7.2 Future Scope

The development and successful implementation of the SFNM under various boundary and loading conditions have been achieved. This approach has been effectively applied to address a variety of standard fracture problems. Moreover, there is potential for further exploration and expansion in various directions.

- In the context of material types, the SFNM has been rigorously tested for both brittle and quasi-brittle materials. For quasi-brittle materials, the model accounts for nonlinear behaviour within the FPZ. Expanding the scope of SFNM, it can be applied to computational analysis of ductile materials. This approach opens up the potential for modelling the nonlinear fracture process zone in ductile materials without relying on enrichment functions.
- The scope of this study can be broadened to encompass fatigue and dynamic loading scenarios. Throughout the dissertation, four floating nodes per element have been consistently utilized for fracture analysis, specifically to capture discrete single cracks. It's worth noting that the SFNM can be adapted to accommodate multiple cracks, including intersecting, non-intersecting cracks and branching crack patterns.
- The smoothening approach employed in this thesis primarily focuses on discrete fracture analysis. However, this same approach can be applied in conjunction with the concept of continuum damage mechanics for a broader range of applications.
- While the entire analysis in this thesis is based on 2D problems, the methodology can be extended and implemented to tackle 3D fracture mechanics challenges.
- Lastly, the proposed method scheme holds promise for application in diverse materials and structural scenarios, such as composites, laminates, functionally graded materials, and hyperelastic materials. Its adaptability allows for addressing a wide array of real-world engineering problems.

### **7.3 Method Limitation**

The analyses are carried out with respect to the specified initial crack length. Taking into account the geometry mesh, the crack tip may reside on any of the four edges of the element or within the element. In the proposed method, the crack tip is modeled at the edge of the element. If the crack tip is found inside the element, it is captured on the adjacent closer edge of the element. The drawback of the method arises from the need to adjust the crack tip to the element edge. Nevertheless, this limitation can be mitigated by utilizing a finer mesh, reducing the gap between the element edge and the crack tip.



## References

---

- [1] Belytschko T, Black T. Elastic crack growth in finite elements with minimal remeshing. *Int J Numer Methods Eng* 1999;45:601–20.
- [2] Moës N, Belytschko T. Extended finite element method for cohesive crack growth. *Eng Fract Mech* 2002;69:813–33.
- [3] Stolarska M, Chopp DL, Mos N, Belytschko T. Modelling crack growth by level sets in the extended finite element method. *Int J Numer Methods Eng* 2001;51:943–60.
- [4] Chen BY, Pinho ST, De Carvalho N V., Baiz PM, Tay TE. A floating node method for the modelling of discontinuities in composites. *Eng Fract Mech* 2014;127:104–34.
- [5] Kumar S, Wang Y, Poh LH, Chen B. Floating node method with domain-based interaction integral for generic 2D crack growths. *Theor Appl Fract Mech* 2018;96:483–96.
- [6] Liu GR, Nguyen TT, Dai KY, Lam KY. Theoretical aspects of the smoothed finite element method (SFEM). *Int J Numer Methods Eng* 2007;71:902–30.
- [7] Bažant ZP. Design of quasibrittle materials and structures to optimize strength and scaling at probability tail: An apercu. *Proc R Soc A Math Phys Eng Sci* 2019;475.
- [8] Dugdale DS. Yielding of steel sheets containing slits. *J Mech Phys Solids* 1960;8:100–4.
- [9] Barenblatt GI. The Mathematical Theory of Equilibrium Cracks in Brittle Fracture. *Adv. Appl. Mech.*, vol. 7, 1962, p. 55–129.
- [10] Hillerborg A, Modéer M, Petersson PE. Analysis of crack formation and crack growth in concrete by means of fracture mechanics and finite elements. *Cem Concr Res* 1976;6:773–81.
- [11] Carpinteri A. Post-peak and post-bifurcation analysis of cohesive crack propagation. *Eng Fract Mech* 1989;32:265–78.
- [12] Yang ZJ, Deeks AJ. Modelling cohesive crack growth using a two-step finite element-scaled boundary finite element coupled method. *Int J Fract* 2007;143:333–54.
- [13] Tvergaard V, Hutchinson JW. Effect of strain-dependent cohesive zone model on predictions of crack growth resistance. *Int J Solids Struct* 1996;33:3297–308.
- [14] Gullerud AS, Gao X, Dodds RH, Haj-Ali R. Simulation of ductile crack growth using computational cells: Numerical aspects. *Eng Fract Mech* 2000;66:65–92.
- [15] Tvergaard V, Hutchinson JW. Toughness of an interface along a thin ductile layer

- 
- joining elastic solids. *Philos Mag A Phys Condens Matter, Struct Defects Mech Prop* 1994;70:641–56.
- [16] Jirásek M. Comparative study on finite elements with embedded discontinuities. *Comput Methods Appl Mech Eng* 2000;188:307–30.
- [17] Wells GN, Sluys LJ. A new method for modelling cohesive cracks using finite elements. *Int J Numer Methods Eng* 2001;50:2667–82.
- [18] Mohammadnejad T, Khoei AR. Hydro-mechanical modeling of two-phase fluid flow in deforming, partially saturated porous media with propagating cohesive cracks using the extended finite element method. *Comput. Plast. XI - Fundam. Appl. COMPLAS XI*, 2011, p. 1516–27.
- [19] Lecampion B. An extended finite element method for hydraulic fracture problems. *Commun Numer Methods Eng* 2009;25:121–33.
- [20] Faivre M, Paul B, Golfier F, Giot R, Massin P, Colombo D. 2D coupled HM-XFEM modeling with cohesive zone model and applications to fluid-driven fracture network. *Eng Fract Mech* 2016;159:115–43.
- [21] Grogan DM, Brádaigh CMÓ, Leen SB. A combined XFEM and cohesive zone model for composite laminate microcracking and permeability. *Compos Struct* 2015;120:246–61.
- [22] Peerlings RHJ, de Borst R, Brekelmans WAM, Geers MGD. Gradient-enhanced damage modelling of concrete fracture. *Mech Cohesive-Frictional Mater* 1998;3:323–42.
- [23] Mühlhaus HB, Alfantis EC. A variational principle for gradient plasticity. *Int J Solids Struct* 1991;28:845–57.
- [24] Geers MGD, De Borst R, Brekelmans WAM, Peerlings RHJ. Strain-based transient-gradient damage model for failure analyses. *Comput Methods Appl Mech Eng* 1998;160:133–53.
- [25] Bažant ZP. Why Continuum Damage is Nonlocal: Micromechanics Arguments. *J Eng Mech* 1991;117:1070–87.
- [26] Bažant ZP, Pijaudier-Cabot G. Nonlocal continuum damage, localization instability and convergence. *J Appl Mech Trans ASME* 1988;55:287–93.
- [27] Triantafyllou A, Perdikaris PC, Giannakopoulos AE. Gradient Elastodamage Model for Quasi-Brittle Materials with an Evolving Internal Length. *J Eng Mech* 2015;141.
- [28] Thai TQ, Rabczuk T, Bazilevs Y, Meschke G. A higher-order stress-based gradient-enhanced damage model based on isogeometric analysis. *Comput Methods Appl Mech Eng* 2016;304:584–604.

- 
- [29] Silling SA. Reformulation of elasticity theory for discontinuities and long-range forces. *J Mech Phys Solids* 2000;48:175–209.
  - [30] Silling SA, Askari E. A meshfree method based on the peridynamic model of solid mechanics. *Comput. Struct.*, vol. 83, 2005, p. 1526–35.
  - [31] Silling SA, Epton M, Weckner O, Xu J, Askari E. Peridynamic states and constitutive modeling. *J Elast* 2007;88:151–84.
  - [32] Kilic B, Agwai A, Madenci E. Peridynamic theory for progressive damage prediction in center-cracked composite laminates. *Compos Struct* 2009;90:141–51.
  - [33] Askari E, Xu J, Silling S. Peridynamic analysis of damage and failure in composites. *Collect. Tech. Pap. - 44th AIAA Aerosp. Sci. Meet.*, vol. 2, 2006, p. 1123–34.
  - [34] Foster JT, Silling SA, Chen WW. Viscoplasticity using peridynamics. *Int J Numer Methods Eng* 2010;81:1242–58.
  - [35] Amani J, Oterkus E, Areias P, Zi G, Nguyen-Thoi T, Rabczuk T. A non-ordinary state-based peridynamics formulation for thermoplastic fracture. *Int J Impact Eng* 2016;87:83–94.
  - [36] Gerstle W, Sau N, Silling S. Peridynamic modeling of concrete structures. *Nucl Eng Des* 2007;237:1250–8.
  - [37] Karma A, Kessler DA, Levine H. Phase-field model of mode III dynamic fracture. *Phys Rev Lett* 2001;87:45501-1-45501–4.
  - [38] Hakim V, Karma A. Laws of crack motion and phase-field models of fracture. *J Mech Phys Solids* 2009;57:342–68.
  - [39] Francfort GA, Marigo JJ. Revisiting brittle fracture as an energy minimization problem. *J Mech Phys Solids* 1998;46:1319–42.
  - [40] Mumford D, Shah J. Optimal approximations by piecewise smooth functions and associated variational problems. *Commun Pure Appl Math* 1989;42:577–685.
  - [41] Buliga M. Energy minimizing brittle crack propagation. *J Elast* 1998;52:201–38.
  - [42] Bourdin B, Francfort GA, Marigo JJ. Numerical experiments in revisited brittle fracture. *J Mech Phys Solids* 2000;48:797–826.
  - [43] Bourdin B. Numerical implementation of the variational formulation for quasi-static brittle fracture. *Interfaces Free Boundaries* 2007;9:411–30.
  - [44] Francfort GA, Bourdin B, Marigo JJ. The variational approach to fracture. *J Elast* 2008;91:5–148.
  - [45] Amor H, Marigo JJ, Maurini C. Regularized formulation of the variational brittle fracture with unilateral contact: Numerical experiments. *J Mech Phys Solids*

- 
- 2009;57:1209–29.
- [46] Lancioni G, Royer-Carfagni G. The variational approach to fracture mechanics. a practical application to the french panthéon in Paris. *J Elast* 2009;95:1–30.
  - [47] Miehe C, Hofacker M, Welschinger F. A phase field model for rate-independent crack propagation: Robust algorithmic implementation based on operator splits. *Comput Methods Appl Mech Eng* 2010;199:2765–78.
  - [48] Miehe C, Welschinger F, Hofacker M. Thermodynamically consistent phase-field models of fracture: Variational principles and multi-field FE implementations. *Int J Numer Methods Eng* 2010;83:1273–311.
  - [49] Wu JY, Cervera M. A novel positive/negative projection in energy norm for the damage modeling of quasi-brittle solids. *Int J Solids Struct* 2018;139–140:250–69.
  - [50] Borden MJ, Verhoosel C V., Scott MA, Hughes TJR, Landis CM. A phase-field description of dynamic brittle fracture. *Comput Methods Appl Mech Eng* 2012;217–220:77–95.
  - [51] Hofacker M, Miehe C. A phase field model of dynamic fracture: Robust field updates for the analysis of complex crack patterns. *Int J Numer Methods Eng* 2013;93:276–301.
  - [52] Verhoosel C V., de Borst R. A phase-field model for cohesive fracture. *Int J Numer Methods Eng* 2013;96:43–62.
  - [53] Feng SZ, Xu Y, Han X, Li ZX, Incecik A. A phase field and deep-learning based approach for accurate prediction of structural residual useful life. *Comput Methods Appl Mech Eng* 2021;383.
  - [54] Feng Y, Wang Q, Wu D, Luo Z, Chen X, Zhang T, et al. Machine learning aided phase field method for fracture mechanics. *Int J Eng Sci* 2021;169.
  - [55] Heister T, Wheeler MF, Wick T. A primal-dual active set method and predictor-corrector mesh adaptivity for computing fracture propagation using a phase-field approach. *Comput Methods Appl Mech Eng* 2015;290:466–95.
  - [56] Badnava H, Msekh MA, Etemadi E, Rabczuk T. An h-adaptive thermo-mechanical phase field model for fracture. *Finite Elem Anal Des* 2018;138:31–47.
  - [57] Tian F, Tang X, Xu T, Yang J, Li L. A hybrid adaptive finite element phase-field method for quasi-static and dynamic brittle fracture. *Int J Numer Methods Eng* 2019;120:1108–25.
  - [58] Xu W, Li H, Li Y, Wang T, Lu S, Qiang S, et al. A phase field method with adaptive refinement strategy and virtual crack insertion technique. *Eng Fract Mech* 2022;271.
  - [59] Kazaryan A, Wang Y, Patton BR. Generalized phase field approach for computer

- 
- simulation of sintering: incorporation of rigid-body motion. *Scr Mater* 1999;41:487–92.
- [60] Kazaryan A, Wang Y, Dregia SA, Patton BR. Grain growth in anisotropic systems: Comparison of effects of energy and mobility. *Acta Mater* 2002;50:2491–502.
- [61] Miyoshi E, Takaki T, Sakane S, Ohno M, Shibuta Y, Aoki T. Large-scale phase-field study of anisotropic grain growth: Effects of misorientation-dependent grain boundary energy and mobility. *Comput Mater Sci* 2021;186.
- [62] Rice JR. A path independent integral and the approximate analysis of strain concentration by notches and cracks. *J Appl Mech Trans ASME* 1968;35:379–88.
- [63] Rice JR, Rosengren GF. Plane strain deformation near a crack tip in a power-law hardening material. *J Mech Phys Solids* 1968;16:1–12.
- [64] Rabczuk T, Zi G, Gerstenberger A, Wall WA. A new crack tip element for the phantom-node method with arbitrary cohesive cracks. *Int J Numer Methods Eng* 2008;75:577–99.
- [65] Tafazzolimoghaddam B. Computational Mechanics of Fracture and Fatigue in Composite Laminates by Means of XFEM and CZM. Sheffield Univ Sheffield PhD Thesis 2017.
- [66] Song JH, Areias PMA, Belytschko T. A method for dynamic crack and shear band propagation with phantom nodes. *Int J Numer Methods Eng* 2006;67:868–93.
- [67] Ling D, Yang Q, Cox B. An augmented finite element method for modeling arbitrary discontinuities in composite materials. *Int J Fract* 2009;156:53–73.
- [68] Fang XJ, Yang QD, Cox BN, Zhou ZQ. An augmented cohesive zone element for arbitrary crack coalescence and bifurcation in heterogeneous materials. *Int J Numer Methods Eng* 2011;88:841–61.
- [69] Reiner J, Veidt M, Dargusch M, Gross L. A progressive analysis of matrix cracking-induced delamination in composite laminates using an advanced phantom node method. *J Compos Mater* 2017;51:2933–47.
- [70] Xin H, Veljkovic M. Fatigue crack initiation prediction using phantom nodes-based extended finite element method for S355 and S690 steel grades. *Eng Fract Mech* 2019;214:164–76.
- [71] Broumand P, Khoei AR. General framework for dynamic large deformation contact problems based on phantom-node X-FEM. *Comput Mech* 2018;61:449–69.
- [72] Belytschko T, Black T. Elastic crack growth in finite elements with minimal remeshing. *Int J Numer Methods Eng* 1999;45:601–20.
- [73] Zhang X, Bui TQ. A fictitious crack XFEM with two new solution algorithms for

- 
- cohesive crack growth modeling in concrete structures. *Eng Comput* (Swansea, Wales) 2015;32:473–97.
- [74] Stolarska M, Chopp DL. Modeling thermal fatigue cracking in integrated circuits by level sets and the extended finite element method. *Int J Eng Sci* 2003;41:2381–410.
- [75] Hettich T, Ramm E. Interface material failure modeled by the extended finite-element method and level sets. *Comput Methods Appl Mech Eng* 2006;195:4753–67.
- [76] Osher, S, Fedkiw, R, Piechor, K. Level Set Methods and Dynamic Implicit Surfaces. *Appl Mech Rev* 2004;57:B15–B15.
- [77] Daux C, Moës N, Dolbow J, Sukumar N, Belytschko T. Arbitrary branched and intersecting cracks with the extended finite element method. *Int J Numer Methods Eng* 2000;48:1741–60.
- [78] Sukumar N, Chopp DL, Moës N, Belytschko T. Modeling holes and inclusions by level sets in the extended finite-element method. *Comput Methods Appl Mech Eng* 2001;190:6183–200.
- [79] Sukumar N, Dolbow JE, Moës N. Extended finite element method in computational fracture mechanics: a retrospective examination. *Int J Fract* 2015;196:189–206.
- [80] Belytschko T, Gracie R, Ventura G. A review of extended/generalized finite element methods for material modeling. *Model Simul Mater Sci Eng* 2009;17.
- [81] Tarancón JE, Vercher A, Giner E, Fuenmayor FJ. Enhanced blending elements for XFEM applied to linear elastic fracture mechanics. *Int J Numer Methods Eng* 2009;77:126–48.
- [82] Singh I V., Mishra BK, Bhattacharya S, Patil RU. The numerical simulation of fatigue crack growth using extended finite element method. *Int J Fatigue* 2012;36:109–19.
- [83] Tran AB, Yvonnet J, He QC, Toulemonde C, Sanahuja J. A multiple level set approach to prevent numerical artefacts in complex microstructures with nearby inclusions within XFEM. *Int J Numer Methods Eng* 2011;85:1436–59.
- [84] Curiel Sosa JL, Karapurath N. Delamination modelling of GLARE using the extended finite element method. *Compos Sci Technol* 2012;72:788–91.
- [85] Wells GN, De Borst R, Sluys LJ. A consistent geometrically non-linear approach for delamination. *Int J Numer Methods Eng* 2002;54:1333–55.
- [86] Wang Y, Waisman H. From diffuse damage to sharp cohesive cracks: A coupled XFEM framework for failure analysis of quasi-brittle materials. *Comput Methods Appl Mech Eng* 2016;299:57–89.
- [87] Nagashima T, Omoto Y, Tani S. Stress intensity factor analysis of interface cracks using

- 
- X-FEM. *Int J Numer Methods Eng* 2003;56:1151–73.
- [88] Liu XY, Xiao QZ, Karihaloo BL. XFEM for direct evaluation of mixed mode SIFs in homogeneous and bi-materials. *Int J Numer Methods Eng* 2004;59:1103–18.
- [89] Fries TP, Belytschko T. The extended/generalized finite element method: An overview of the method and its applications. *Int J Numer Methods Eng* 2010;84:253–304.
- [90] Fries T. Overview and comparison of different variants of the XFEM. *Pamm* 2014;14:27–30.
- [91] Kumar S, Singh I V., Mishra BK. A multigrid coupled (FE-EFG) approach to simulate fatigue crack growth in heterogeneous materials. *Theor Appl Fract Mech* 2014;72:121–35.
- [92] Lu YY, Belytschko T, Gu L. A new implementation of the element free Galerkin method. *Comput Methods Appl Mech Eng* 1994;113:397–414.
- [93] Nguyen VP, Rabczuk T, Bordas S, Duflo M. Meshless methods: A review and computer implementation aspects. *Math Comput Simul* 2008;79:763–813.
- [94] Belytschko T, Lu YY, Gu L. Crack propagation by element-free Galerkin methods. *Eng Fract Mech* 1995;51:295–315.
- [95] Brighenti R. Application of the element-free Galerkin meshless method to 3-D fracture mechanics problems. *Eng Fract Mech* 2005;72:2808–20.
- [96] Belytschko T, Krongauz Y, Organ D, Fleming M, Krysl P. Meshless methods: An overview and recent developments. *Comput Methods Appl Mech Eng* 1996;139:3–47.
- [97] Pathak H, Singh A, Singh IV. Fatigue crack growth simulations of homogeneous and bi-material interfacial cracks using element free Galerkin method. *Appl Math Model* 2014;38:3093–123.
- [98] Pathak H, Singh A, Singh IV. Numerical simulation of bi-material interfacial cracks using EFGM and XFEM. *Int J Mech Mater Des* 2012;8:9–36.
- [99] Huang R, Sukumar N, Prévost JH. Modeling quasi-static crack growth with the extended finite element method Part II: Numerical applications. *Int J Solids Struct* 2003;40:7539–52.
- [100] Rabczuk T, Bordas S, Zi G. A three-dimensional meshfree method for continuous multiple-crack initiation, propagation and junction in statics and dynamics. *Comput Mech* 2007;40:473–95.
- [101] Giner E, Sukumar N, Denia FD, Fuenmayor FJ. Extended finite element method for fretting fatigue crack propagation. *Int J Solids Struct* 2008;45:5675–87.
- [102] Singh I V., Jain PK. Parallel EFG algorithm for heat transfer problems. *Adv Eng Softw*

- 
- 2005;36:554–60.
- [103] Rabczuk T, Areias PMA, Belytschko T. A meshfree thin shell method for non-linear dynamic fracture. *Int J Numer Methods Eng* 2007;72:524–48.
- [104] Ai W, Bird RE, Coombs WM, Augarde CE. A configurational force driven cracking particle method for modelling crack propagation in 2D. *Eng Anal Bound Elem* 2019;104:197–208.
- [105] Ai W, Augarde CE. An adaptive cracking particle method for 2D crack propagation. *Int J Numer Methods Eng* 2016;108:1626–48.
- [106] Chen BY, Tay TE, Pinho ST, Tan VBC. Modelling the tensile failure of composites with the floating node method. *Comput Methods Appl Mech Eng* 2016;308:414–42.
- [107] Lu X, Chen BY, Tan VBC, Tay TE. Adaptive floating node method for modelling cohesive fracture of composite materials. *Eng Fract Mech* 2018;194:240–61.
- [108] Singh U, Kumar S, Chen B. Smoothed floating node method for modelling 2D arbitrary crack propagation problems. *Theor Appl Fract Mech* 2022;117.
- [109] Hu XF, Lu X, Tay TE. Modelling delamination migration using virtual embedded cohesive elements formed through floating nodes. *Compos Struct* 2018;204:500–12.
- [110] Zhi J, Chen BY, Tay TE. A geometrically nonlinear floating node method for damage modelling of composites. *ECCM 2018 - 18th Eur. Conf. Compos. Mater.*, 2020.
- [111] Trabal GG, Bak BLV, Chen B, Carreras L, Lindgaard E. An adaptive floating node based formulation for the analysis of multiple delaminations under high cycle fatigue loading. *Compos Part A Appl Sci Manuf* 2022;160.
- [112] Chen JS, Wu CT, Yoon S, You Y. Stabilized conforming nodal integration for Galerkin mesh-free methods. *Int J Numer Methods Eng* 2001;50:435–66.
- [113] Dai KY, Liu GR, Nguyen TT. An n-sided polygonal smoothed finite element method (nSFEM) for solid mechanics. *Finite Elem Anal Des* 2007;43:847–60.
- [114] Xie W, He X, Wu J, Liu Y. An edge-based smoothed finite element method for 2D mechanics problems. *Xibei Gongye Daxue Xuebao/Journal Northwest Polytech Univ* 2017;35:7–12.
- [115] He ZC, Liu GR, Zhong ZH, Cui XY, Zhang GY, Cheng AG. A coupled edge-/face-based smoothed finite element method for structural-acoustic problems. *Appl Acoust* 2010;71:955–64.
- [116] Nguyen-Xuan H, Bordas S, Nguyen-Dang H. Smooth finite element methods: Convergence, accuracy and properties. *Int J Numer Methods Eng* 2008;74:175–208.
- [117] Liu GR. A generalized gradient smoothing technique and the smoothed bilinear form



- 
- for Galerkin formulation of a wide class of computational methods. *Int J Comput Methods* 2008;5:199–236.
- [118] Nguyen-Thoi T, Phung-Van P, Luong-Van H, Nguyen-Van H, Nguyen-Xuan H. A cell-based smoothed three-node Mindlin plate element (CS-MIN3) for static and free vibration analyses of plates. *Comput Mech* 2013;51:65–81.
- [119] Phung-Van P, Nguyen-Thoi T, Bui-Xuan T, Lieu-Xuan Q. A cell-based smoothed three-node Mindlin plate element (CS-FEM-MIN3) based on the C0-type higher-order shear deformation for geometrically nonlinear analysis of laminated composite plates. *Comput Mater Sci* 2015;96:549–58.
- [120] Nguyen-Thoi T, Liu GR, Lam KY, Zhang GY. A face-based smoothed finite element method (FS-FEM) for 3D linear and geometrically non-linear solid mechanics problems using 4-node tetrahedral elements. *Int J Numer Methods Eng* 2009;78:324–53.
- [121] Liu GR, Nguyen-Thoi T, Lam KY. An edge-based smoothed finite element method (ES-FEM) for static, free and forced vibration analyses of solids. *J Sound Vib* 2009;320:1100–30.
- [122] Nguyen-Xuan H, Liu GR, Bordas S, Natarajan S, Rabczuk T. An adaptive singular ES-FEM for mechanics problems with singular field of arbitrary order. *Comput Methods Appl Mech Eng* 2013;253:252–73.
- [123] Bhowmick S, Liu GR. A phase-field modeling for brittle fracture and crack propagation based on the cell-based smoothed finite element method. *Eng Fract Mech* 2018;204:369–87.
- [124] Li E, Chang CC, He ZC, Zhang Z, Li Q. Smoothed finite element method for topology optimization involving incompressible materials. *Eng Optim* 2016;48:2064–89.
- [125] Mohapatra D, Kumar J. Smoothed finite element approach for kinematic limit analysis of cohesive frictional materials. *Eur J Mech A/Solids* 2019;76:328–45.
- [126] Doblare M, Espiga F, Gracia L, Alcantud M. Study of crack propagation in orthotropic materials by using the boundary element method. *Eng Fract Mech* 1990;37:953–67.
- [127] Sollero P, Aliabadi MH. Fracture mechanics analysis of anisotropic plates by the boundary element method. *Int J Fract* 1993;64:269–84.
- [128] Haojiang D, Aimin J. A boundary integral formulation and solution for 2D problems in magneto-electro-elastic media. *Comput Struct* 2004;82:1599–607.
- [129] García-Sánchez F, Rojas-Díaz R, Sáez A, Zhang C. Fracture of magnetoelectroelastic composite materials using boundary element method (BEM). *Theor Appl Fract Mech* 2007;47:192–204.

- 
- [130] Zhi J, Chen BY, Tay TE. Geometrically nonlinear analysis of matrix cracking and delamination in composites with floating node method. *Comput Mech* 2019;63:201–17.
- [131] De Carvalho N V., Chen BY, Pinho ST, Ratcliffe JG, Baiz PM, Tay TE. Modeling delamination migration in cross-ply tape laminates. *Compos Part A Appl Sci Manuf* 2015;71:192–203.
- [132] Liu GR, Quek SS. *Finite Element Method: A Practical Course*. 2003.
- [133] Liu GR, Dai KY, Nguyen TT. A smoothed finite element method for mechanics problems. *Comput Mech* 2007;39:859–77.
- [134] Bordas SPA, Rabczuk T, Hung NX, Nguyen VP, Natarajan S, Bog T, et al. Strain smoothing in FEM and XFEM. *Comput Struct* 2010;88:1419–43.
- [135] Surendran M, Natarajan S, Bordas SPA, Palani GS. Linear smoothed extended finite element method. *Int J Numer Methods Eng* 2017;112:1733–49.
- [136] Krongauz Y, Belytschko T. Consistent pseudo-derivatives in meshless methods. *Comput Methods Appl Mech Eng* 1997;146:371–86.
- [137] Gosz M, Dolbow J, Moran B. Domain integral formulation for stress intensity factor computation along curved three-dimensional interface cracks. *Int J Solids Struct* 1998;35:1763–83.
- [138] Sukumar N, Huang ZY, Prévost JH, Suo Z. Partition of unity enrichment for bimaterial interface cracks. *Int J Numer Methods Eng* 2004;59:1075–102.
- [139] Wang SS, Yau JF, Corten HT. A mixed-mode crack analysis of rectilinear anisotropic solids using conservation laws of elasticity. *Int J Fract* 1980;16:247–59.
- [140] Bhattacharya S, Singh I V., Mishra BK, Bui TQ. Fatigue crack growth simulations of interfacial cracks in bi-layered FGMs using XFEM. *Comput Mech* 2013;52:799–814.
- [141] Griffiths AA. The phenomena of rupture and flow in solids. *Masinovedenie* 1995;9–14.
- [142] Barenblatt GI. The Mathematical Theory of Equilibrium Cracks in Brittle Fracture. *Adv Appl Mech* 1962;7:55–129.
- [143] Unger JF, Eckardt S, Könke C. Modelling of cohesive crack growth in concrete structures with the extended finite element method. *Comput Methods Appl Mech Eng* 2007;196:4087–100.
- [144] Camacho GT, Ortiz M. Computational modelling of impact damage in brittle materials. *Int J Solids Struct* 1996;33:2899–938.
- [145] Needleman A. A continuum model for void nucleation by inclusion debonding. *J Appl Mech Trans ASME* 1987;54:525–31.
- [146] Xu XP, Needleman A. Void nucleation by inclusion debonding in a crystal matrix.

- 
- Model Simul Mater Sci Eng 1993;1:111–32.
- [147] Tvergaard V, Hutchinson JW. The relation between crack growth resistance and fracture process parameters in elastic-plastic solids. *J Mech Phys Solids* 1992;40:1377–97.
- [148] Tvergaard V. Effect of fibre debonding in a whisker-reinforced metal. *Mater Sci Eng A* 1990;125:203–13.
- [149] Fries TP. A corrected XFEM approximation without problems in blending elements. *Int J Numer Methods Eng* 2008;75:503–32.
- [150] Laborde P, Pommier J, Renard Y, Salaün M. High-order extended finite element method for cracked domains. *Int J Numer Methods Eng* 2005;64:354–81.
- [151] Ortiz M, Pandolfi A. Finite-deformation irreversible cohesive elements for three-dimensional crack-propagation analysis. *Int J Numer Methods Eng* 1999;44:1267–82.
- [152] Nguyen O, Repetto EA, Ortiz M, Radovitzky RA. A cohesive model of fatigue crack growth. *Int J Fract* 2001;110:351–69.
- [153] Ortiz M, Suresh S. Statistical properties of residual stresses and intergranular fracture in ceramic materials. *J Appl Mech Trans ASME* 1993;60:77–84.
- [154] Espinosa HD, Zavattieri PD. A grain level model for the study of failure initiation and evolution in polycrystalline brittle materials. Part I: Theory and numerical implementation. *Mech. Mater.*, vol. 35, 2003, p. 333–64.
- [155] Park K, Paulino GH, Roesler JR. A unified potential-based cohesive model of mixed-mode fracture. *J Mech Phys Solids* 2009;57:891–908.
- [156] Park K, Paulino GH. Computational implementation of the PPR potential-based cohesive model in ABAQUS: Educational perspective. *Eng Fract Mech* 2012;93:239–62.
- [157] Jirásek M, Marfia S. Non-local damage model based on displacement averaging. *Int J Numer Methods Eng* 2005;63:77–102.
- [158] Xie M, Gerstle WH. Energy-Based Cohesive Crack Propagation Modeling. *J Eng Mech* 1995;121:1349–58.
- [159] Ooi ET, Yang ZJ. Modelling crack propagation in reinforced concrete using a hybrid finite element-scaled boundary finite element method. *Eng Fract Mech* 2011;78:252–73.
- [160] Yu H, Wu L, Guo L, Wu H, Du S. An interaction integral method for 3D curved cracks in nonhomogeneous materials with complex interfaces. *Int J Solids Struct* 2010;47:2178–89.
- [161] Roth SN, Léger P, Soulaïmani A. A combined XFEM-damage mechanics approach for

- 
- concrete crack propagation. *Comput Methods Appl Mech Eng* 2015;283:923–55.
- [162] Negi A, Singh U, Kumar S. Structural size effect in concrete using a micromorphic stress-based localizing gradient damage model. *Eng Fract Mech* 2021;243.
- [163] García-Álvarez VO, Gettu R, Carol I. Analysis of mixed-mode fracture in concrete using interface elements and a cohesive crack model. *Sadhana - Acad Proc Eng Sci* 2012;37:187–205.
- [164] Gardner DR, Lark RJ, Barr B. Effect of conditioning temperature on the strength and permeability of normal- and high-strength concrete. *Cem Concr Res* 2005;35:1400–6.
- [165] Liu GR. An Overview on Meshfree Methods: For Computational Solid Mechanics. *Int J Comput Methods* 2016;13.
- [166] Duflot M. The extended finite element method in thermoelastic fracture mechanics. *Int J Numer Methods Eng* 2008;74:827–47.
- [167] Pant M, Singh I V., Mishra BK. Numerical simulation of thermo-elastic fracture problems using element free Galerkin method. *Int J Mech Sci* 2010;52:1745–55.
- [168] Singh U, Kumar S. Smoothed floating node method for modelling cohesive fracture in quasi-brittle materials. *Mech Adv Mater Struct* 2022;1–15.
- [169] Benabou L, Sun Z, Dahoo PR. A thermo-mechanical cohesive zone model for solder joint lifetime prediction. *Int J Fatigue* 2013;49:18–30.
- [170] Jung J, Do BC, Yang QD. Augmented finite-element method for arbitrary cracking and crack interaction in solids under thermo-mechanical loadings. *Philos Trans R Soc A Math Phys Eng Sci* 2016;374:20150282.
- [171] Özdemir I, Brekelmans WAM, Geers MGD. A thermo-mechanical cohesive zone model. *Comput Mech* 2010;46:735–45.
- [172] Banks-Sills L, Dolev O. The conservative M-integral for thermal-elastic problems. *Int J Fract* 2004;125:149–70.
- [173] Pathak H, Singh A, Singh IV. Fatigue crack growth simulations of bi-material interfacial cracks under thermo-elastic loading by extended finite element method. *Eur J Comput Mech* 2013;22:79–104.
- [174] Sih GC. On the singular character of thermal stresses near a crack tip. *J Appl Mech Trans ASME* 1960;29:587–8.
- [175] Hansbo A, Hansbo P. A finite element method for the simulation of strong and weak discontinuities in solid mechanics. *Comput Methods Appl Mech Eng* 2004;193:3523–40.
- [176] Moës N, Béchet E, Tourbier M. Imposing Dirichlet boundary conditions in the extended

- 
- finite element method. *Int J Numer Methods Eng* 2006;67:1641–69.
- [177] Bordas SPA, Natarajan S. On the approximation in the smoothed finite element method (SFEM). *Int J Numer Methods Eng* 2010;81:660–70.
- [178] Liu GR. The smoothed finite element method (S-FEM): A framework for the design of numerical models for desired solutions. *Front Struct Civ Eng* 2019;13:456–77.
- [179] Bouhala L, Makradi A, Belouettar S. Thermal and thermo-mechanical influence on crack propagation using an extended mesh free method. *Eng Fract Mech* 2012;88:35–48.
- [180] Jin ZH, Batra RC. Thermal fracture of ceramics with temperature-dependent properties. *J Therm Stress* 1998;21:157–76.
- [181] Costanzo F, Walton JR. Steady growth of a crack with a rate and temperature sensitive cohesive zone. *J Mech Phys Solids* 2002;50:1649–79.
- [182] Hattiangadi A, Siegmund T. A thermomechanical cohesive zone model for bridged delamination cracks. *J Mech Phys Solids* 2004;52:533–66.
- [183] Hattiangadi A, Siegmund T. Bridging effects in cracked laminates under thermal gradients. *Mech Res Commun* 2002;29:457–64.
- [184] Sarkar S, Singh I V., Mishra BK. A Thermo-mechanical gradient enhanced damage method for fracture. *Comput Mech* 2020;66:1399–426.
- [185] Poh LH, Sun G. Localizing gradient damage model with decreasing interactions. *Int J Numer Methods Eng* 2017;110:503–22.
- [186] Vernerey F, Liu WK, Moran B. Multi-scale micromorphic theory for hierarchical materials. *J Mech Phys Solids* 2007;55:2603–51.
- [187] Simoes M, Martínez-Pañeda E. Phase field modelling of fracture and fatigue in Shape Memory Alloys. *Comput Methods Appl Mech Eng* 2021;373.
- [188] Wu JY, Huang Y, Nguyen VP. On the BFGS monolithic algorithm for the unified phase field damage theory. *Comput Methods Appl Mech Eng* 2020;360.
- [189] Wang HS. A meshfree variational multiscale methods for thermo-mechanical material failure. *Theor Appl Fract Mech* 2015;75:1–7.
- [190] Zhang XL, Jiao YY, Zhao J. Simulation of failure process of jointed rock. *J Cent South Univ Technol (English Ed)* 2008;15:888–94.